Aston University

Some pages of this thesis may have been removed for copyright restrictions.

If you have discovered material in Aston Research Explorer which is unlawful e.g. breaches copyright, (either yours or that of a third party) or any other law, including but not limited to those relating to patent, trademark, confidentiality, data protection, obscenity, defamation, libel, then please read our Takedown policy and contact the service immediately (openaccess@aston.ac.uk)

Design and optimisation of micro-structured waveguides in nonlinear crystals

HUSEYIN KARAKUZU

Doctor of Philosophy

ASTON UNIVERSITY

December 2016

© Huseyin Karakuzu, 2016

[Huseyin Karakuzu] asserts his moral right to be identified as the author of this theses

This copy of the thesis has been supplied on condition that anyone who consults it is understood to recognise that its copyright rests with its author and that no quotation from the thesis and no information derived from it may be published without proper permission or acknowledgement.

Dedicated to my father and mother

Ali and Güner Karakuzu

Abstract

Direct femtosecond laser inscription has emerged as one of the most efficient methods for direct three dimensional micro-fabrication of integrated optical circuits in dielectric crystals. Lithium niobate is one of the most widely used dielectric crystal for a wide range of optical functions. Using the direct femtosecond inscription technology, it is possible to produce almost circular tracks of $1-2.5\,\mu$m diameters with negative refractive index changes up to -0.012 in lithium niobate crystals. Those tracks can be used as a cladding region to confine the propagating light inside a core region of a micro-structured waveguide. This dissertation is focused on the numerical investigation of the propagation properties of depressed-cladding, buried micro-structured waveguides in z-cut lithium niobate crystals which can be fabricated by direct fs laser inscription method.

First of all, we discuss how experimentally achievable parameters of cladding tracks such as their position, total number, refractive index contrasts between the low index cladding structure and the core region can be used to design buried micro-structured waveguides with good confinement properties and to achieve any control over the propagation properties of different polarisation modes specific to a wide range of applications of lithium niobate. Numerical analysis of micro-structured waveguides are implemented by using finite element method.

The high nonlinear coefficient and wide transparency region of lithium niobate enable its use for frequency conversion applications towards mid-infrared wavelength ranges. In this thesis, optimisation of the guiding properties, specifically the confinement losses, of micro-structured waveguides in lithium niobate is realised for both around telecom and mid-infrared wavelength regions. Optimisation is based on a practical approach which takes into account the variation of experimentally achieved track parameters over cladding region. It is shown that the spectral region where confinement losses are below 1 dB/cm can be extended up to a wavelength of $3.5\,\mu$m.

In recent years, a variety of design geometries for micro-structured waveguides has been a focus of research interest as a means of manipulating and controlling the properties of propagating light. The flexibility of writing tracks at various depths inside lithium niobate crystals allows direct fabrication of micro-structured waveguides with advanced design geometries. The ability to write tracks at varying sizes by femtosecond laser inscription method enables the fabrication of micro-structured waveguides with highly complex spiral geometries. Here, we explore design issues of equiangular, Fermat and Archimedes spiral geometries in accordance with experimentally available track parameters. Optimisation of each geometry is separately implemented for telecom and mid-infrared wavelength ranges. The primary advantage of designing waveguides with spiral geometries is a much finer control and better manipulation of propagating light stemming from a higher number of parameters available for design. Also, it is found that the spectral region where confinement losses are below 1 dB/cm can be further extended up to a wavelength of 3.66 μm.

Acknowledgments

I would like to express my sincere gratitude to my supervisor, Dr. Sonia Boscolo. I am deeply thankful for her trust, patience and support, as well as encouragement to move forward during my research study at Aston University. From the time I had my first contact, I was carefully guided, supported and encouraged to do things in the best way. I would like to thank my co-supervisor, Dr. Mykhaylo Dubov, for spending his invaluable time to enlighten me when I was stuck with problems, at any time I needed help. I have learnt a lot during my research studies through their continuous guidance and support. It was a pleasure to be learning from both of you.

I am very gifted to have such a family that never left supporting and loving me at good and bad. I could not have come to this point without the wish to complete and dedicate this thesis to them. Also, I would like to commemorate my grandparents and to express my gratitude for all their efforts and prays for me.

I am thankful to Aston Institute of Photonics Technologies (AIPT), where it was an enjoyment to be together with such highly qualified scientists and researchers. I learned a lot from the seminar series organised by AIPT and enjoyed to be in such an atmosphere where scientists from all over the world had come and talked about their latest research subject.

I am also indebted to the Leverhuelme Trust Foundation for the financial support.

Contents

Abstract **3**

Acknowledgements **4**

Contents **5**

List of Figures **8**

List of Tables **12**

Abbreviations and Units **13**

1 Introduction **14**

1.1 Research motivation 14

1.2 Thesis structure 19

2 Approaches to the modelling of micro-structured waveguides **21**

2.1 Propagation model 22

2.1.1 Maxwell's equations 22

2.1.2 Harmonic time dependence and wave equations 23

2.1.3 Anisotropic media 25

2.1.4 Eigenmodes of anisotropic micro-structured waveguides 28

2.2 Numerical solution techniques 29

2.2.1 Plane wave method 33

2.2.2 Finite Element Method 36

2.2.3 Validation of FEM results 46

2.3 Summary 49

3 Experimental background **50**

3.1 Direct femtosecond laser inscription method 50

3.1.1 Direct femtosecond laser inscription in Lithium Niobate 55

3.2 Experimental setup and procedures 64

3.3 Results 69

3.4 Summary 73

4 Design of depressed-cladding micro-structured waveguides in $LiNbO_3$ **74**

4.1 Introduction 74

4.2 Waveguide packing geometry and methodology 75

4.3 Mesh and PML setting 78

4.4 Results and discussion 79

4.5 Conclusion 85

5 Optimisation of micro-structured waveguides for broadband operation **87**

5.1 Set-up of MS WG geometry for optimisation 88

5.2 Numerical results by PWM and comparison with FEM 89

5.3 Optimisation of WG structural parameters 91

5.4 Summary 97

6 Advanced waveguide geometries **98**

6.1 Introduction 98

6.2 The design of MS WGs with spiral geometries 100

6.3 Optimisation of WG structural parameters 104

6.4 Comparison of MS WG geometries in $LiNbO_3$ 108

6.5 Summary 115

7 Conclusions **116**

7.1 Future Work 118

References **120**

A Numerical computation **133**

A.1 A Comsol - Matlab script to calculate the propagation modes of a MS WG . 133

A.2 A matlab code to construct RI profile from cumulative phase data 138

B Publications **141**

List of Figures

2.1 Left: Direction of the wave vector for a monochromatic wave relative to the orientation of the indicatrix in a crystal. Right: Orientation of the indicatrix inside negative and positive uniaxial crystals. 27

2.2 Mesh of a two-ring MS WG with an hexagonal geometry. 38

2.3 Configuration of a triangular element. 40

2.4 Cross section of MS WG surrounded by a circular PML. 44

2.5 Comparison of our calculations with: the FEM calculations of [94] using a squared PML, the FEM calculations of [95] using a circular PML, and the MM calculations of [67], for an MOF with two layers of air holes. 47

2.6 (a) Cross section of MOF with ten layers of air holes. (b) Comparison of our calculations of confinement loss with: the FEM calculations of [96] using a squared PML and the FEM calculations of [95] using a circular PML. (c), (d) Computed MOF dispersion and effective area. 48

3.1 Experimental setup. WP: wave plate, PBS: polarisation beam splitter, M: folding mirror, MO: micro-objective, CCD: charge-couple device. 64

3.2 (a) DIC microscope views of two pairs of tracks [45] (Inscription energy is 58 nJ, scanning speeds are 40 mm/s (left pair) and 60 mm/s (right pair), inscription depth is $\approx 200\,\mu$m) (b) Radial RI profile of a track [45] (Inscription energy is 58 nJ, scan velocity is 12 mm/s and inscription depth is $\approx 200\,\mu$m). 70

3.3 (a) Radius and (b) peak RI contrast of the tracks as a function of inscription energy [45] (Scanning velocity is 12 mm/s and approximate inscription depth is $250\,\mu$m). 71

3.4 Microscope (a) overhead view, and (b) cross section view of a fabricated MS WG with two rings of tracks [45] (Inscription energy is 48 nJ, scan velocity is 15 mm/s, and inscription depth is $\approx 250\,\mu$m). 72

4.1 Cross section of modeled depressed-cladding WG with two rings of tracks, and ellipsoid of indices for $LiNbO_3$ host. 76

4.2 Confinement loss for O wave as a function of PML thickness for different values of the PML maximum absorption for a depressed-cladding WG with two rings of tracks ($N_r = 2$) at various wavelengths: (a) $\lambda = 0.5\,\mu$m, (b) $\lambda = 1\,\mu$m, (c) $\lambda = 1.3\,\mu$m, and (d) $\lambda = 1.6\,\mu$m. WG parameters are: $d = 1.6\,\mu$m, $a = 2\,\mu$m, $\delta n = -0.05$. 79

4.3 Real parts of effective RIs for O and E waves as a function of wavelength for a depressed-cladding WG with two rings of tracks, $N_r = 2$. The O and E RIs of the unmodified material are also shown. WG parameters are: $d = 1.6\,\mu$m, $a = 2\,\mu$m, $\delta n = -0.05$. 80

4.4 (a) WG dispersion D_W for O wave, and (b) confinement losses for O and E waves as a function of wavelength for a depressed-cladding WG with two rings of tracks with various pitches. The material dispersion D_{mat} is also shown. Other WG parameters are: $d = 1.6\,\mu$m, $\delta n = -0.05$. 81

4.5 (a) WG dispersion D_W for O wave, and (b) confinement losses for O and E waves as a function of wavelength for a depressed-cladding WG with two rings of tracks of various RI contrasts. The material dispersion D_{mat} is also shown. Other WG parameters are: $d = 1.6\,\mu$m, $a = 2\,\mu$m. 82

4.6 (a) WG dispersion D_W for O wave, and (b) confinement losses for O and E waves as a function of wavelength for a depressed-cladding WG with varying number of track rings. The material dispersion D_{mat} is also shown. Other WG parameters are: $d = 1.6\,\mu$m, $a = 2\,\mu$m, $\delta n = -0.01$. 84

4.7 (a) confinement losses for O and E waves as a function of wavelength for depressed-cladding WG with seven rings of tracks, $N_r = 7$, with different diameters $d = 1.2 - 2\,\mu$m. Other WG parameters are: $a = 2.5\,\mu$m, $\delta n = -0.01$. The losses for seven rings of identical diameter are also shown (extracted from Fig. 4.6). (b) cross section of modeled WG structure. . . . 85

5.1 Cross-section of WG structure with seven rings of tracks with different diameters, and ellipsoid of RIs of z-cut $LiNbO_3$ crystal. 88

5.2 Left: track diameter versus cladding layer number for a seven-ring WG structure with different growth rate parameters p. Right: Cross-sections of seven-ring structures for (from top to bottom and left to right) $p = 0$ (uniform structure), 0.2, 1, 5. Other parameters are: pitch $a = 2.5$ μm, $D_{\max} = 2.4$ μm, $D_{\min} = 1$ μm. 90

5.3 Real parts of effective RIs as a function of wavelength for the PWM computed modes of a WG structure with seven rings of tracks. 91

5.4 Real parts of effective RIs for O and E waves as a function of wavelength for the fundamental mode of a seven-ring WG structure, as obtained from PWM and FEM simulations. 92

5.5 Confinement loss for E wave at $\lambda = 1.55$ μm versus track diameter for a seven-ring WG structure with $a = 2.5$ μm and different values of δn. 93

5.6 Confinement loss for E wave versus growth rate parameter p at $\lambda = 1.55$ μm (left) and $\lambda = 3$ μm (right), for a seven-ring WG structure with $\delta n = -0.01$. Here, $D_{\min} = 1$ μm. 94

5.7 Confinement losses for O and E waves as a function of wavelength for a seven-ring WG structure with different growth rate parameters p. Other parameters are: $\delta n = -0.01$, $D_{\max}$ =2.2 μm, $D_{\min}$=1 μm. 95

5.8 Confinement loss for E wave versus loss induced on tracks by fs inscription for a WG with $p = 0$ and $p = 0.5$ at $\lambda = 1.55$ μm, and with $p = 0.01$ at $\lambda = 3$ μm. Other WG parameters are: $\delta n = -0.01$, $a = 2.5$ μm, $D_{\max} = 2.4$ μm, $D_{\min} = 1$ μm. 96

5.9 Confinement losses for O and E waves as a function of wavelength for a seven-ring WG structure with $p = 0.01$. Other parameters are: maximum RI contrast $\delta n = -0.01$, $D_{\max} = 2.4$ μm, $D_{\min} = 1$ μm. 97

6.1 Cross sections of MS WGs with optimised parameters of Equiangular spiral geometry, Fermat spiral geometry, Archimedes spiral geometry and Hexagonal geometry. 99

6.2 Cross section of ES modeled depressed-cladding WG with six arms ($M_{\text{arm}} = 6$) and five ring ($N_{\text{ring}} = 5$) of tracks 101
6.3 Positions of tracks within FS geometry 102
6.4 (a) α and p pairs, and (b) confinement losses of MS WGs with ES geometry at 3 μm wavelength. 105
6.5 The change of confinement loss (blue) and effective area (red)(a) by N_0 ($N_{\text{total}} = 210$, $p = 0$), and (b) by p ($N_0 = 11$, $N_{\text{total}} = 210$) for a MS WG with FS geometry at 3 μm of wavelength. 106
6.6 (a) $N_0 - p$ pairs, and (b) confinement losses of MS WGs with $N_0 - p$ pairs of AS geometry at 3 μm wavelength ($N_{\text{total}} = 210$). 107
6.7 A comparison of MS WG geometries in terms of confinement loss for (a) E polarisation, (b) O polarisation, (c) effective area and (d) WG dispersion. . 109
6.8 The change of confinement loss by positioning errors of tracks in MS WGs with ES (blue), FS (pink), FS (green) spiral geometries and hexagonal (red) geometry for O polarisation vs. effective RI (n_O^{eff}) at 3 μm wavelength. . . . 111
6.9 (a) The change of birefringence by wavelength for optimised MS WGs with hexagonal, ES, FS and AS geometries, (b) the change of birefringence of an optimised MS WG with FS geometry by N_{total} at 1.55 μm wavelength. . . . 114

List of Tables

2.1 Sellmeier coefficients for pure silica. 46

3.1 A comparison of experimental settings used by various researchers during fs laser inscription in $LiNbO_3$. P: Polarisation (L: Linear, C: Circular), PW: Pulse width, PE: Pulse energy, RR: Repetition rate, TS: Translation speed, NP: Number of pulses per μm 61

4.1 Sellmeier coefficients for 5 mol.% MgO doped $LiNbO_3$ 77

5.1 Real parts of effective mode indices for O and E waves calculated using the PWM and the FEM. The RIs of the unmodified material $n_{o,e}$ are also displayed. 91

6.1 A comparison of optimised WG properties 113

Abbreviations and units

λ	Wavelength
μm	Micrometer
2D	Two-dimensional
3D	Three-dimensional
AS	Archimedes spiral
CCD	Charge coupled device
CPO	Chirped pulse oscillator
E	Extraordinary
ES	Equiangular spiral
FEM	Finite element method
FDFD	Finite difference frequency domain
FDTD	Finite difference time domain
FS	Fermat spiral
fs	Femtosecond
GVD	Group velocity dispersion
HRR	High repetition rate
IOC	Integrated optical circuit
$LiNbO_3$	Lithium niobate
Mid-IR	Mid-infrared
MM	Multipole method
MO	Micro objective
MOF	Micro-structured optical fibre
MS	Micro-structured
NA	Numerical aperture
O	Ordinary
PBG	Photonic band gap
PC	Photonic crystal
PDE	Partial differential equation
PML	Perfectly matching layer
PPLN	Periodically poled lithium niobate
PWM	Plane wave method
QPM	Quantitative phase microscopy
RI	Refractive index
SBR	Saturable Bragg reflector
WG	Waveguide
ZDW	Zero waveguide-dispersion wavelength

Chapter 1

Introduction

1.1 Research motivation

On-going advances in optics and photonics has been a leading factor of fast progress in various scientific areas such as communication, material science, computing, medicine, and many others. Optical waveguides (WGs) [1–3] play an essential role in optics and photonics because they enable efficient transmission of light between any two points, and they serve as a basic tool of integrated optical (and photonic) circuits (IOCs) [4] to implement linear and nonlinear functions for a variety of purposes. IOC technology refers to the fabrication of advanced optical devices by combining and interconnecting multiple optical and photonic components, for example, optical modulators, couplers, switchers, multiplexers, polarisers, interferometers, optical sources and detectors on a single chip. Lowering the costs, decreasing the sizes and thereby increasing the functionality of advanced complex devices in smaller footprints are the primary motivations for the integration of multiple optical and photonic functions in a single device.

Fabrication technologies of optical WGs are highly varied depending on the materials

used and the relevant WG geometry. Glass, nonlinear crystals, semiconductors and polymers are some of the materials which are frequently used to fabricate optical WGs and IOC devices. Lithium niobate ($LiNbO_3$) [5, 6] is one of the most widely used nonlinear optical crystals in IOC devices due to its wide transparency range from 0.3 μm to 5 μm, high second-order nonlinearity, electro-optical, acousto-optical and photorefractive properties. Additionally, it is a birefringent material and has a high nonlinear optical coefficient. It can be doped with active materials for the purpose of optical amplification. One of the most important features of $LiNbO_3$ in terms of IOC is that almost all basic IOC functions can be fabricated to build complex IOC devices on $LiNbO_3$ [7]. Functionality of basic blocks are based on either just transmission of light or control and manipulation of the properties of light during transmission through WGs.

There exist a number of techniques for the fabrication of optical WGs in $LiNbO_3$ such as metal ion (titanium, zinc, iron) indiffusion [8], proton exchange, ion beam techniques, pulsed laser deposition, direct femtosecond laser inscription, etc. Each fabrication technique has its advantages and disadvantages. Titanium indiffusion has been exploited to fabricate WG based devices since the middle of 70s [9]. Basically, titanium is diffused into the $LiNbO_3$ substrate at near 1000 °C for a duration of 4 to 12 hours, and the desired WG geometry is obtained by selectively removing titanium layers by lithographic techniques. The titanium indiffused regions in $LiNbO_3$ maintain the electro-optic properties and ensure a positive change for both ordinary and extraordinary refractive indexes (RIs), though the amount of RI change is less compared to other techniques [10].

Proton exchange is another classical method to fabricate WGs in $LiNbO_3$ [11]. It is based on immersion of a masked $LiNbO_3$ wafer into a high temperature ($200 - 250$ °C) acid bath for several days to exchange lithium ions with protons in unmasked regions at

a surface depth of 1 to 10 μm, thereby leading to a small decrease in the ordinary RI and an increase in the extraordinary RI of $LiNbO_3$ up to about 0.01 [12]. The proton exchange should be followed by an annealing process to maintain an effective nonlinear coefficient and to improve the deterioration of the electro-optic coefficient. WGs fabricated by the proton exchange method support the propagation of light polarised only along the extraordinary direction of polarisation due to the positive induced RI change [13].

Ion implantation [14, 15], a well-known method for the fabrication of WGs in $LiNbO_3$, is implemented by bombarding the crystals surface with ions which are accelerated at an impact energy and directed towards the material surface at a controlled angle to modify the materials optical properties. Ion implantation in $LiNbO_3$ produces locally reduced RI changes. Guiding of optical waves is therefore realised in an unmodified region confined by reduced RI regions [16, 17].

The conventional methods described above allow the fabrication of two dimensional (2D) planar structures only on or near the surface of $LiNbO_3$. Consequently, polishing the surface of the crystal wafer after WG fabrication requires very delicate procedures. Also, the depth of WGs from the crystal's surface is very limited due to penetration insufficiency of metal ions or protons. This entails no control on the shaping of the RIs and geometry of the WG. On the other hand, controlling the WG geometry would permit to reduce the otherwise present high coupling losses. Another issue with the WG inscription in $LiNbO_3$ arises due to changes in the material structure during WG fabrication, thereby leading to a decreased damage threshold and disruption of the poled $LiNbO_3$ domains. While communication applications of $LiNbO_3$ WGs use low signal powers, the efficiency of high power frequency conversion applications is diminished due to the lowered damage threshold of the WG regions.

Besides, large-scale applications of $LiNbO_3$ are in general limited because of expensive

clean room facilities, time consuming processes, high cost and low throughput, and limited possibility for fabricating integrated 3D complex optical devices. In recent years, the direct femtosecond (fs) laser inscription method [18,19] has evolved as a rapidly evolving alternative technology to fabricate IOCs in optical materials. It is based on focusing intense radiation of a fs laser beam in a focal point inside the bulk material and translating the focal point at a certain velocity along a 3D path. This method enables single-step, mask free fabrication of isolated air holes or voids, continuous and smooth tracks or channels with arbitrary and irregular 3D geometries which can be buried inside a broad range of materials like glass [20, 21], polymers [22], ceramics [23] and crystals [24, 25]. A variety of 3D buried structures with different optical functions can be fabricated and incorporated in $LiNbO_3$ for the realisation of compact and highly complex IOCs without the need for any clean room facilities [26–28].

Different types of RI modifications have been reported in or around irradiated areas of $LiNbO_3$ crystals during the fabrication of continuous tracks, depending on the structure and orientation of the crystal, and on the experimental parameters of the fs laser inscription process [29]. A first type of RI modification, associated with low or moderate level of laser energy densities, occurs in the irradiated focal volume with an increase of the extraordinary RI and no change in the ordinary RI [30–34]. It supports guidance of light along the track, so it has the inherent advantage of easy fabrication of single-line WGs and 3D structures. However, the absorption and scattering properties as well as nonlinear and electro-optic properties of the structurally modified regions also change and cause higher losses and diminished WG functionality. Moreover, this type of RI modification occurs only along one direction of the crystal, resulting in propagation of only one polarisation state of light with asymmetric output mode [35, 36]. Also, positive RI modifications [34–36] reduce or

completely vanish when exposed to thermal treatment, thereby showing thermally unstable behaviours.

A second type of RI modification is associated with high laser energy densities, causing a volume increase in the focal region with corresponding RI decrease in both polarisations and an induced stress in the surrounding material [29, 36]. Consequently, wave-guiding in single line tracks with reduced RI changes is not possible. However, WGs can still be produced by designing a depressed index cladding [37] such that light can be confined in a region of material by writing multiple tracks with a reduced RI around an unmodified region, which serves as the core of a WG. The depressed-cladding WG approach has some advantages compared to directly written single track WGs. Firstly, light is guided in a region that is not modified by fs laser irradiation, so the nonlinear and electro-optic properties of $LiNbO_3$ are conserved. Secondly, such WGs support balanced confinement of both polarisation states of light, which is highly important for applications based on the interactions between different polarisation states. Besides, a fairly large number of arbitrarily arranged tracks can be written to achieve light propagation with good confinement at different wavelengths. It is also possible to pre-set the size and shape of both core and cladding regions. Flexible sizes of WG cross sections are especially important for low loss coupling of fibres to WG integrated photonic chips and of inter-connects between multiple functional devices in $LiNbO_3$. Most importantly, due to the geometric flexibility of writing buried tracks at any position inside the material, the concept of periodically structured RI arrangements in dielectric materials, which was first introduced by Yablonovitch [38] as photonic crystals (PCs) [39], can be applied to fabricate 1D, 2D or 3D micro-structured (MS) WGs in $LiNbO_3$ by fs laser inscription. The PC technology has drawn considerable attention owing to its potential for realising ultra compact IOCs and its ability to control the flow of light. In the 2D case, MS fibres [40]

exhibit very interesting properties. For example, complete frequency band gaps can be observed, which is very important for strong confinement of light in small volumes to reach high light intensities. The WG dispersion and zero dispersion wavelength can be tailored by changing the periodicity, size and shape of the tracks and the WG geometry. It has been also shown that single mode propagation can be achieved over a wide wavelength range [41].

Arbitrarily shaped MS WGs consisting of an unmodified core region and a depressed-index cladding can also be achieved in $LiNbO_3$ crystals by using the fs laser inscription method. MS WGs with just two tracks [27,28,35,42] or a circular geometry [37,43,44] have already been achieved in various crystals. The primary motivation for this thesis work is to study MS WGs comprising multiple tracks with reduced RIs based on the experimentally obtained parameters for fs-induced modification tracks in $LiNbO_3$ [45]. The aim is to ensure good light confinement in the MS WG as depressed-index cladding WGs often exhibit leaky-mode features, and to optimise the propagation properties of the WG with respect to the geometrical design parameters.

1.2 Thesis structure

This thesis is organised according to the following structure:

Chapter 2 starts with a presentation of theoretical aspects relevant to wave propagation in anisotropic materials. Then commonly used methods to analyse the properties of MS WGs are discussed, and the choice of the finite-element method (FEM), which is thereafter used in the thesis, is explained. The application of the general concept of a perfectly matched layer (PML) to truncate the computational domain and, thus, ensure correct analysis of the lossy nature of MS WGs, is described. The accuracy of

the results obtained is validated through comparison with previously published results.

Chapter 3 starts with a review of the direct fs laser inscription method and then describes the experimental settings of fs laser systems and the WG characterisation method. The experimentally achievable operational parameters for fs laser inscription in $LiNbO_3$ are given.

Chapter 4 is devoted to the numerical study of depressed-index cladding MS WGs that can be formed in a $LiNbO_3$ crystal by fs laser writing. The feasibility of controlling the wave-guiding properties are investigated by exploiting WG geometric and structural characteristics such as the track size, spacing, number of rings and RI contrast.

Chapter 5 presents a practical approach to the numerical optimisation of the guiding properties of MS WGs in $LiNbO_3$, aiming at extending the spectral range of low-loss operation of the WG into the mid-infrared region. A comparison between the results obtained with the plane wave method (PWM) and the FEM is also provided.

Chapter 6 explores advanced WG geometries to enhance the propagation properties in $LiNbO_3$. Specifically, the design procedures for three different spiral geometries, namely the equiangular, Fermat and Archimedes geometries, are presented. The parameters of these geometries are then optimised, and the performances of the optimised geometries are compared to those of the conventional hexagonal geometry.

Chapter 7 summarises the outcomes of the research work presented in this thesis and discusses promising directions for future research.

Chapter 2

Approaches to the modelling of micro-structured waveguides

Whilst optical WGs with the desired propagation properties can be designed and fabricated on a try and test procedure, this approach may be highly time consuming and not be capable of fully exploiting the new degrees of freedom offered today by the possibility of engineering the material properties at the micro-metre scale. Therefore, to develop the potential of MS WGs, accurate and efficient modelling tools are necessary.

In this chapter, after reviewing the theoretical aspects concerned with wave propagation in anisotropic materials, we describe the numerical modelling methods and approaches that constitute the pillars of the work presented in this thesis.

2.1 Propagation model

2.1.1 Maxwell's equations

The most fundamental equations in electrodynamics are Maxwell's equations, which are given in the following in rationalised MKS units [46]

$$\nabla \times \vec{E} + \frac{\partial \vec{B}}{\partial t} = 0 \tag{2.1}$$

$$\nabla \times \vec{H} - \frac{\partial \vec{D}}{\partial t} = \vec{J} \tag{2.2}$$

$$\nabla \cdot \vec{D} = \rho \tag{2.3}$$

$$\nabla \cdot \vec{B} = 0 \tag{2.4}$$

In these equations, $\vec{E}$ and $\vec{H}$ are the electric field vector (in volts per meter) and the magnetic field vector (in amperes per meter), respectively. The two field vectors are often used to describe an electromagnetic field. The quantities $\vec{D}$ and $\vec{B}$ are called the electric displacement (in coulombs per square meter) and the magnetic induction (in webers per square meter), respectively, and they are introduced to include the effect of the field on matter. The quantities ρ and $\vec{J}$ are the electric charge (in coulombs per cubic meter) and current (in amperes per square meter) densities, respectively, and may be considered as the sources of the fields $\vec{E}$ and $\vec{H}$. These four Maxwell's equations completely determine the electromagnetic field.

In optics, one often deals with propagation of electromagnetic radiation in regions of space where both charge density and current density are zero. The solutions to Maxwell's equations with $\rho = 0$ and $\vec{J} = 0$ are called electromagnetic waves.

To obtain a unique determination of the field vectors, Maxwell's equations must be

supplemented by the so-called constitutive equations (or material equations),

$$\vec{D} = \varepsilon\vec{E} = \varepsilon_0\vec{E} + \vec{P} \tag{2.5}$$

$$\vec{B} = \mu\vec{H} = \mu_0\vec{H} + \vec{M} \tag{2.6}$$

where the constitutive parameters ε and μ are tensors of rank 2 and are known as the dielectric tensor (or permittivity tensor) and the permeability tensor, respectively; $\vec{P}$ and $\vec{M}$ are electric and magnetic polarisations, respectively. The constants ε_0 and μ_0 are called the permittivity and permeability of a vacuum, respectively, and have respective values of 8.854×10^{-12} F/m and $4\pi \times 10^{-7}$ H/m. If the material medium is isotropic, both ε and μ reduce to scalars. In many cases, the quantities ε and μ can be assumed to be independent of the field strengths. The treatment of nonlinear optical effects occurring when the fields are sufficiently strong are beyond the scope of this thesis.

2.1.2 Harmonic time dependence and wave equations

Maxwell's equations simplify considerably in the case of harmonic time dependence. Through the inverse Fourier transform, general solutions of Maxwell's equation can be built as linear combinations of single-frequency solutions: $\vec{E}(\vec{r},t) = \int \vec{E}(\vec{r},\omega)e^{i\omega t}\,\mathrm{d}\omega/(2\pi)$. Thus, we assume that all fields have a time dependence $e^{i\omega t}$:

$$\vec{E}(\vec{r},t) = \vec{E}(\vec{r})e^{i\omega t}, \quad \vec{H}(\vec{r},t) = \vec{H}(\vec{r})e^{i\omega t}$$

where the phasor amplitudes $\vec{E}(\vec{r})$, $\vec{H}(\vec{r})$ are complex-valued.

We now derive the wave equations in material media, which is achieved by mathematical elimination so that each of the field vectors satisfies a differential equation. We limit our attention to regions where both charge density and current density vanish. We also consider

a transparent, nonmagnetic medium for which $\mu = \mu_0$. If we use the constitutive relation (2.6) for $\vec{B}$ in Eq. (2.1), divide both sides by μ_0 and apply the curl operator, we obtain

$$\frac{1}{\mu_0}\nabla \times (\nabla \times \vec{E}) + \frac{\partial}{\partial t}\nabla \times \vec{H} = 0$$

If we now differentiate Eq. (2.2) with respect to time (using $\partial_t \to i\omega$), and combine it with Eq. (2.1), and use the material Eq. (2.5), we obtain

$$\nabla \times (\nabla \times \vec{E}) - k_0^2 \varepsilon_r \vec{E} = 0 \tag{2.7}$$

where $\varepsilon_r = \varepsilon/\varepsilon_0$ is the relative permittivity, $k_0 = \omega/c = 2\pi/\lambda$ is the free-space wave number, and $c = 1/\sqrt{\mu_0\varepsilon_0} = 2.997930 \times 10^8$ m/s is the phase velocity of the electromagnetic radiation in a vacuum. We now employ the vector identity

$$\nabla \times (\nabla \times \vec{E}) = \nabla(\nabla \cdot \vec{E}) - \nabla^2 \vec{E}$$

and Eq. (2.7) becomes

$$\nabla^2 \vec{E} + k_0^2 \varepsilon_r \vec{E} - \nabla(\nabla \cdot \vec{E}) = 0$$

By substituting for $\vec{D}$ from Eq. (2.5) into Eq. (2.3) and applying the vector identity

$$\nabla(\varepsilon \vec{E}) = \varepsilon \nabla \cdot \vec{E} + \vec{E} \cdot \nabla \varepsilon$$

we obtain from the above equation

$$\nabla^2 \vec{E} + k_0^2 \varepsilon_r \vec{E} + \nabla(\vec{E} \cdot \nabla \ln \varepsilon) = 0 \tag{2.8}$$

This, or equivalently Eq. (2.7), is the wave equation for the electric field vector. The wave equation for the magnetic field vector can be obtained in a similar way and is given by

$$\nabla \times (\eta \nabla \times \vec{H}) - k_0^2 \vec{H} = 0 \tag{2.9}$$

where $\eta = 1/\varepsilon_r$, or

$$\nabla^2\vec{H} + k_0^2\vec{H} + (\nabla \ln \varepsilon) \times (\nabla \times \vec{H}) = 0 \tag{2.10}$$

Inside a homogeneous and isotropic medium, the gradient of the logarithm of ε vanishes, and Eqs. (2.8) and (2.10) reduce to the standard electromagnetic wave equations. In this thesis, we will consider the solutions of wave Eqs. (2.8) and (2.10) in the context of waves propagating in MS WGs within uniaxial anisotropic crystals.

2.1.3 Anisotropic media

Wave propagation in anisotropic media such as calcite, quartz, and $LiNbO_3$ is determined by the dielectric tensor ε_{ij} that links the displacement vector and the electric field vector (Eq. (2.5)): $D_i = \varepsilon_{ij}E_j$, where the convention of summation over repeated indices is observed. In nonmagnetic and transparent materials, this tensor is real and symmetric: $\varepsilon_{ij} = \varepsilon_{ji}$. The magnitude of these nine tensor elements depends, of course, on the choice of the x, y, and z axes relative to the crystal structure. Because of its real and symmetric nature, it is always possible to find three mutually orthogonal axes in such a way that the off-diagonal elements vanish, leaving

$$\varepsilon = \varepsilon_0 \begin{pmatrix} n_x^2 & 0 & 0 \\ 0 & n_y^2 & 0 \\ 0 & 0 & n_z^2 \end{pmatrix} = \begin{pmatrix} \varepsilon_x & 0 & 0 \\ 0 & \varepsilon_y & 0 \\ 0 & 0 & \varepsilon_z \end{pmatrix} \tag{2.11}$$

where ε_x, ε_y, and ε_z are the principal dielectric constants and n_x, n_y, and n_z are the principal indices of refraction. These axes (x, y, and z) form the principal axes coordinate system.

Let us assume that a monochromatic plane wave of the form $\vec{D}\exp[i(\omega t - \vec{k}\cdot\vec{r})]$ can propagate through an anisotropic medium. The direction of $\vec{D}$ specifies the direction of polarisation of this wave. The wave vector $\vec{k}$ of this plane wave is normal to the wavefront

(the plane where the phase of the wave is everywhere equal) and has magnitude $|\vec{k}| = \omega/v$; v is the phase velocity of the wave, which is related to the velocity of light in vacuum by the RI n experienced by the wave according to $v = c/n$. It is possible to show that for propagation in a general direction, two distinct allowed linear polarisations specified by the direction of $\vec{D}$ can exist for such wave. These two allowed polarisations are orthogonal and the wave propagates with a phase velocity depending on which of these two polarisations it has. Clearly, a wave of arbitrary polarisation which enters such an anisotropic medium will not in general correspond to one of the allowed polarisations, and will therefore be resolved into two linearly polarised components along the allowed polarisation directions. The specification of the orientation of these allowed polarisation directions with respect to the principal axes of the medium is done with the aid of a geometric figure called the index ellipsoid or indicatrix [47]. This is an ellipsoid with the equation

$$\frac{x^2}{n_x^2} + \frac{y^2}{n_y^2} + \frac{z^2}{n_z^2} = 1 \tag{2.12}$$

This ellipsoid can be visualised as oriented inside a crystal consistent with the symmetry axes of the crystal. For example, in any crystal with perpendicular symmetry axes, such as those belonging to the cubic, tetragonal, hexagonal, trigonal or orthorhombic crystal systems, the axes of the ellipsoid, which are the principal axes of the crystal, are parallel to the three axes of symmetry of the crystal, which allows to determine the refractive indices and polarisations of the two monochromatic plane waves which can propagate through the crystal with a given wave vector. For the orientation of the indicatrix to be consistent with the symmetry of the crystal, planes of mirror symmetry within the crystal must coincide with planes of symmetry of the indicatrix: namely the xy, yz and zx planes. We can use the geometrical properties of the indicatrix to determine the RIs and polarisations of the

two monochromatic plane waves which can propagate through the crystal with a given wave vector. This is illustrated in Fig. 2.1, which shows the direction of the wave vector $\vec{k}$ for a monochromatic wave propagating through a crystal, drawn relative to the orientation of the indicatrix in the crystal. The plane surface that is orthogonal to the wave vector, and that passes through the centre of the indicatrix, intersects this ellipsoid in an ellipse called the intersection ellipse. The semi-axes of this ellipse define the directions of the two allowed $\vec{D}$ polarisations which can propagate through the crystal with the given wave vector $\vec{k}$, and the lengths of these semi-axes give the RIs experienced by these two polarisations. In the

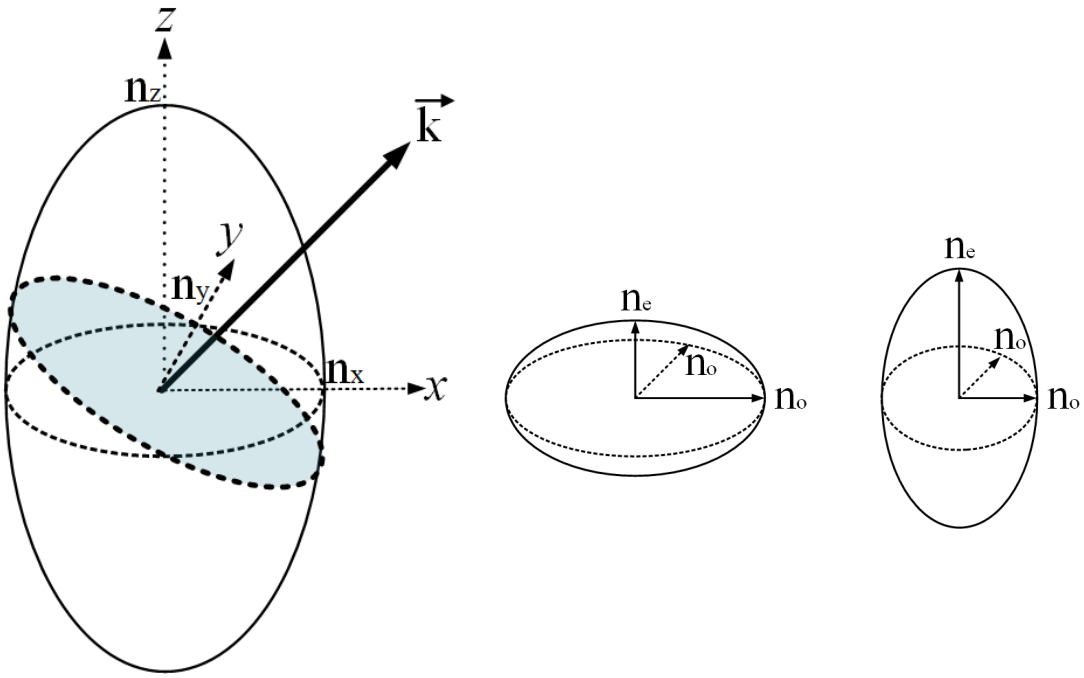

Figure 2.1: Left: Direction of the wave vector for a monochromatic wave relative to the orientation of the indicatrix in a crystal. Right: Orientation of the indicatrix inside negative and positive uniaxial crystals.

general case when the three principal indices n_x, n_y, n_z are all different, there are two $\vec{k}$ vector directions through the centre of the indicatrix for which the intersection ellipse is a circle. This is a fundamental geometric property of ellipsoids. These two directions are called the principal optic axes and are fixed for a given crystal and frequency of light. Waves can

propagate along these optic axes with any arbitrary polarisation, as in these directions the RI is not a function of polarisation. In this general case, the crystal is said to be biaxial. If the three principal indices are equal, the indicatrix is a sphere called the isotropic indicatrix, there are no specific optic axes as the indicatrix is an axial and the propagation of waves is independent of both the directions of $\vec{k}$ and $\vec{D}$. In crystals belonging to the tetragonal, hexagonal and trigonal crystal systems the crystal symmetry requires two of the principal indices be equal: $n_x = n_y$ and the indicatrix reduces to an ellipsoid of revolution. In this case there is only one optic axis, oriented along the axis of highest symmetry of the crystal, the z axis (or c axis of crystallographic terminology). These crystals classes are said to be uniaxial. The equation of the uniaxial indicatrix is

$$\frac{x^2+y^2}{n_o^2}+\frac{z^2}{n_e^2}=1 \tag{2.13}$$

where n_o is the index of refraction experienced by waves polarised perpendicular to the optic axis, called ordinary or O - waves; n_e is the index of refraction experienced by waves polarised parallel to the optic axis, called extraordinary or E - waves. If $n_e > n_o$ the indicatrix is a prolate ellipsoid of revolution as shown in Fig. 2.1 and such a crystal is said to be positive uniaxial. If $n_e < n_o$ the indicatrix is an oblate ellipsoid of revolution as shown in Fig. 2.1 and the crystal is said to be negative uniaxial.

2.1.4 Eigenmodes of anisotropic micro-structured waveguides

Hereinafter, we will consider the propagation of monochromatic optical waves in a transparent, uniaxial crystal with the z optic axis hosting a depressed-index cladding WG with the track RI contrast $\delta n < 0$. For such a crystal, we can use the approximation introduced in [48] and

express the RIs as

$$n_{o,e}(x,z) = n_{o,e} + \delta n\, f(x,z), \quad f(x,z) = \begin{cases} 1, & (x,z) \in \text{tracks} \\ 0, & (x,z) \in \text{otherwise} \end{cases} \tag{2.14}$$

Given the direction of propagation along the y axis, a mode of propagation of the dielectric structure, that is, a solution of (2.7) with (2.11) and (2.14), is characterised by the mode's field pattern and its effective RIs $n_{o,e}^{\text{eff}} = \beta_{o,e}/k_0$, where $\beta_{o,e}$ is the propagation constant for x- and z-polarised light, respectively. Because of the finite transverse extent of the confining structure, the effective RI is a complex value; its imaginary part $\Im(n_{\text{eff}})$ is related to losses $\mathcal{L}$ (in decibels per centimeter) through the relation $\mathcal{L} = 40\pi\Im(n_{\text{eff}}) \times 10^4/[\lambda \ln(10)]$, where λ is given in micrometers. Dispersion parameter D is computed through the usual formula from the real part of effective RI $\Re(n_{\text{eff}})$ [49]: $D = -(\lambda/c)\partial^2\Re(n_{\text{eff}})/\partial\lambda^2$. Chromatic dispersion in micro-structured WGs arises from that of the unmodified material (D_{mat}) and also from the WG dispersion (D_W) associated with the structure of the confining region. Solution of Eqs. (2.7), (2.11) and (2.14) provides directly the total dispersion (D), so we deduced D_W from the relation $D_W \simeq D - D_{\text{mat}}$. Finally, a quantitative measure of the area which a WG mode effectively covers in the transverse dimensions is provided by the effective mode area: $A_{\text{eff}} = (\iint |E(x,z)|^2\, \mathrm{d}x\mathrm{d}z)^2 / \iint |E(x,z)|^4\, \mathrm{d}x\mathrm{d}z$.

2.2 Numerical solution techniques

The optimisation of the performance of optical WG devices requires a knowledge of their propagation characteristics and field distributions, and their dependence on the fabrication parameters. As the range of guiding structures becomes more intricate, so the need for computer analysis becomes greater and thus more demanding. Therefore, there is a particular

interest in theoretical methods of WG analysis which has attracted the attention of many researchers. Several computation models fundamentally relying on numerical techniques for solving partial differential equations [50–53] have been developed and applied to a large number of scientific and engineering problems. Numerical techniques devoted to the modal analysis of WGs generally deal with the time-harmonic (frequency domain) Maxwell's equations. Furthermore, the modal analysis of inhomogeneous WGs with anisotropic materials requires a numerical method which can handle full vectorial wave equations (Eq. (2.7) and (2.9)) under boundary conditions, which is to be incorporated to provide the continuity of equations between different media. According to boundary conditions, tangential components of electric and magnetic fields and normal components of electric displacement and magnetic induction must be continuous across interfaces between different materials [54]. Well established vectorial modal solvers that have been widely used to predict WG properties include the finite-difference time-domain (FDTD) method, the plane wave method (PWM), the multipole method (MM), and the finite element method (FEM).

The principle of FD methods [53, 55–57] is close to the numerical schemes used to solve ordinary differential equations. It consists in approximating the differential operator by replacing the derivatives in the equation using differential quotients. FDTD is a popular computational electromagnetics technique that belongs in the general class of grid-based differential time-domain numerical modelling methods. These methods discretise the space in terms of grids (both orthogonal and non-orthogonal) and solve Maxwell's equations at each point in the grid. In FDTD, Maxwell's equations (in partial differential form) are modified to central-difference equations, discretised, and implemented in software. The equations are solved in a cyclic manner: the electric field is solved at a given instant in time, then the magnetic field is solved at the next instant in time, and the process is repeated

over and over again. Modal solutions can be obtained from the observation of the field distributions during propagation. As FDTD provides a direct approach to the computation of the first- and second-order derivatives in the wave equations, a corresponding eigenvalue matrix equation can be assembled and modal solutions can directly be obtained. The computational domain in FDTD needs to be finalised by boundary conditions. However, the discretisation of the computational domain by regular sized rectangular grids consumes computer memory, and solving the equations takes significant time, so large-scale problems involving complex geometries generally face memory and CPU limitations.

The PWM computational technique [39, 51, 58–60] solves the Maxwell's equations by formulating and eigenvalue problem out of the equation. This method is popular among the photonic crystal community as a method of solving for the band structure (dispersion relation) of specific photonic crystal geometries. The PWM is traceable to the analytical formulations, and is highly efficient for calculating modes in periodic dielectric structures. The numerical computation is based on expanding the periodic functions of the fields and material properties in Fourier series, inserting them into the wave equations and solving the corresponding eigenvalue matrix problem. The finalisation of the computational domain is not restricted by any boundary condition owing to the assumption of periodicity. The PWM and its generalisations have already been used for the analysis of anisotropic WGs [61] and MS optical fibres [62–64]. The PWM can be computationally fast, and it is also well suited for the study of mode interactions as well dispersion characteristics changes under external influences. However, PW treatments effectively replace the necessarily finite WG structure with an infinite one and thus cannot address the issue of the loss associated with propagation in a transversely finite confining structure (confinement loss). As a result, they cannot provide an accurate description of leaky WGs, for which the imaginary parts of the effective

mode indices are large. PWMs also do not accommodate general characteristics of the geometry of the inclusions/tracks. Whereas they are highly general, they are consequently not highly efficient.

The MM is based on the multipole expansion technique, and was first applied in computational electromagnetics by Engheta et al. (1992) [65]. In the MM [66–68], electromagnetic fields which are modal solutions to wave equations are represented as a superposition of scattered fields from all dielectric boundaries. Therefore, each inclusion/track and the outer boundaries enclosing the core and cladding regions are considered as sources of field. Cylindrical harmonic functions are used as a natural basis for the cylindrical scatterers to represent the scattered fields. When all incoming and outgoing fields of inclusions/tracks are related to each other by boundary conditions, the resulting algebraic equations in terms of each boundary equation can be transformed into an eigenvalue matrix equation whose solution gives the corresponding propagation constant. This method has been successfully used to calculate the confinement loss for the leaky modes of MS optical fibres with fast convergence and high accuracy [66, 67]. However, the method is at present limited to designs composed of non-intersecting circular inclusions/tracks [69], and a decrease in the spacing between tracks may cause convergence problems.

The FEM [50, 70, 71] implements a variational form of the wave equation and applies it over each small region formed by discretisation of the WG structure. The size and shape of these subregions can be locally varying, thereby allowing for a better representation of the fields in key regions. Instead of basis functions, the FEM uses interpolation functions to define the fields over such subspaces. The variational form of the wave equation is computed in each subregion in terms of edge and node coefficients of the interpolation functions, and the corresponding equations are assembled into a global eigenvalue matrix

equation. Among the different numerical approaches, the FEM has established itself as a powerful method throughout engineering for its flexibility and versatility, being used to solve partial differential equations over complex domains or when the desired precision varies over the entire domain. One of the most important features of FEMs is that they are based on unstructured grids, whereas FD methods use structured grids. This means that FEM is more flexible with respect to the geometry. For example, in two dimensions, we do not need the computational domain to be rectangular or something that can be mapped onto a rectangle.The FEM is particularly advantageous for electromagnetic field problems, because of its applicability to WGs with arbitrary geometry, arbitrary RI profile, and anisotropic or nonlinear materials or materials with absorption (indicated by the imaginary part of the RI). The FEM has been widely used during the last four decades in the analysis of various optical WG structures. Thus it is probably the WG analysis method that is the most generally applicable and most versatile. Based on these reasons, we have chosen the FEM as the primary method for the modal analysis of MS WGs in anisotropic crystals. Additionally, we have used the PWM as an efficient and convenient tool for preliminary calculations when modelling complex WG structures. We will describe these two techniques in the following sections.

2.2.1 Plane wave method

As we have seen in Section 2.1, monochromatic optical waves of angular frequency ω propagating along the y axis of the cartesian coordinate system in a transparent, uniaxial crystal with the z optical axis and relative permittivity ε_r, hosting a depressed-cladding WG with the RI contrast δn can be described by the wave equation (2.9) and $\nabla \cdot \vec{H} = 0$ following

from the Maxwell's equations, along with Eqs. (2.11) and (2.14). The distance- and time-dependence of the electromagnetic field: $\exp(i\omega t - i\beta y)$ is assumed, where $\beta = k_0 n^{\text{eff}}$ is the propagation constant of the mode propagating in the structure. To apply PW decomposition, the WG structure should be put in a box and tiled periodically along the x- and z-axes. The box should not be too large in order not to include a large area of unmodified material around the structure and, at the same time, should not be too small in order to avoid overlapping of modes in adjacent computational cells. Thus, the size of the box has to be a parameter for the calculations.

The equation $\nabla \cdot \vec{H} = 0$ can be used to exclude $H_y(x,z)$ from Eq. (2.9) and, thus, obtain

$$\begin{aligned}
\beta^2 H_x(x,z) &= \frac{\partial^2 H_x}{\partial x^2} + \frac{\partial^2 H_x}{\partial z^2} + k_0^2 \frac{1}{\eta_o} H_x + \frac{1}{\eta_o}\frac{\partial \eta_o}{\partial z}\left(\frac{\partial H_x}{\partial z} - \frac{\partial H_z}{\partial x}\right), \\
\beta^2 H_z(x,z) &= \frac{\eta_o}{\eta_e}\frac{\partial^2 H_z}{\partial x^2} + \frac{\partial^2 H_z}{\partial z^2} + k_0^2 \frac{1}{\eta_e} H_z + \left(1 - \frac{\eta_e}{\eta_o}\right)\frac{\partial^2 H_x}{\partial x \partial z} - \frac{1}{\eta_e}\frac{\partial \eta_o}{\partial x}\left(\frac{\partial H_x}{\partial z} - \frac{\partial H_z}{\partial x}\right).
\end{aligned} \tag{2.15}$$

Equations (2.15) can be solved using the PWM [62, 63] to find out the (real) eigenvalues β^2 and eigenvectors $\{H_x, H_z\}$. For this purpose, we use the following expansions in terms of PWs:

$$\begin{aligned}
H_x(x,z) &= \sum_{m=-\infty}^{\infty}\sum_{n=-\infty}^{\infty} H^x_{m,n} \exp\left[iG^x_{m,n}x + iG^z_{m,n}z\right], \\
H_z(x,z) &= \sum_{m=-\infty}^{\infty}\sum_{n=-\infty}^{\infty} H^z_{m,n} \exp\left[iG^x_{m,n}x + iG^z_{m,n}z\right], \\
\frac{1}{\eta_o(x,z)} &= \sum_{m=-\infty}^{\infty}\sum_{n=-\infty}^{\infty} U^o_{m,n} \exp\left[iG^x_{m,n}x + iG^z_{m,n}z\right], \\
\frac{1}{\eta_e(x,z)} &= \sum_{m=-\infty}^{\infty}\sum_{n=-\infty}^{\infty} U^e_{m,n} \exp\left[iG^x_{m,n}y + iG^z_{m,n}z\right], \\
\eta_o(x,z) &= \sum_{m=-\infty}^{\infty}\sum_{n=-\infty}^{\infty} P^o_{m,n} \exp\left[iG^x_{m,n}x + iG^z_{m,n}z\right], \\
\eta_e(x,z) &= \sum_{m=-\infty}^{\infty}\sum_{n=-\infty}^{\infty} P^e_{m,n} \exp\left[iG^x_{m,n}x + iG^z_{m,n}z\right],
\end{aligned} \tag{2.16}$$

with unknown complex amplitudes $H^{x,z}_{m,n}$, and $G^x_{m,n} = 2\pi m/a$, $G^z_{m,n} = 2\pi n/a$. Substituting these expansions into Eq. (2.15) and equalising the coefficients of the same exponential factors one can obtain the following linear equations for the modal amplitudes $H^x_{m,n}$, $H^z_{m,n}$:

$$\sum_{m'=-\infty}^{\infty}\sum_{n'=-\infty}^{\infty}\left(L^{xx}_{m',n'}H^x_{m',n'} + L^{xz}_{m',n'}H^z_{m',n'}\right) = \beta^2 H^x_{m,n},$$
$$\sum_{m'=-\infty}^{\infty}\sum_{n'=-\infty}^{\infty}\left(L^{zx}_{m',n'}H^x_{m',n'} + L^{zz}_{m',n'}H^z_{m',n'}\right) = \beta^2 H^z_{m,n}, \tag{2.17}$$

where

$$L^{xx}_{m',n'} = -\left[(G^x_{m,n})^2 + (G^z_{m,n})^2\right]\delta_{mm'}\delta_{nn'} + k_0^2 U^o_{m-m',n-n'} + iG^z_{m',n'}V^o_{m-m',n-n'},$$
$$L^{xz}_{m',n'} = iG^x_{m',n'}V^o_{m-m',n-n'}, \quad L^{zz}_{m',n'} = -(G^z_{m,n})^2\delta_{mm'}\delta_{nn'} - (G^x_{m',n'})^2 W_{m-m',n-n'},$$
$$-G^x_{m',n'}G^x_{m',n'}T_{m-m',n-n'} + k_0^2 U^e_{m-m',n-n'} + iG^x_{m',n'}V^e_{m-m',n-n'}, \quad L^{zx}_{m',n'} = iG^z_{m',n'}V^e_{m-m',n-n'},$$
$$V^{o,e}_{m,n} = \sum_{m'=-\infty}^{\infty}\sum_{n'=-\infty}^{\infty} iG^{z,x}_{m',n'}P^o_{m',n'}U^{o,e}_{m-m',n-n'}, \quad W_{m,n} = \sum_{m'=-\infty}^{\infty}\sum_{n'=-\infty}^{\infty} P^o_{m',n'}U^e_{m-m',n-n'},$$
$$T_{m,n} = \sum_{m'=-\infty}^{\infty}\sum_{n'=-\infty}^{\infty} P^o_{m',n'}\left(P^o_{m-m',n-n'} - P^e_{m-m',n-n'}\right).$$

From Eq. (2.17), one can determine β^2 and $H^{x,z}_{m,n}$. The transverse components of the electric field $E_{x,z}$ and the longitudinal component of the Poynting vector S_y will be then given by

$$E_x = \frac{\eta_e(x,z)}{\beta k_0}\left(\beta^2 H_z - \frac{\partial^2 H_z}{\partial z^2} - \frac{\partial H_x}{\partial x \partial z}\right), \quad E_z = -\frac{\eta_o(x,z)}{\beta k_0}\left(\beta^2 H_x - \frac{\partial^2 H_z}{\partial x \partial z} - \frac{\partial^2 H_x}{\partial x^2}\right),$$
$$S_y = \Re\left[E_z^* H_x - E_x^* H_z\right]. \tag{2.18}$$

The solution of Eq. (2.17) involves the calculation of Fourier harmonics of the mode profiles. For arbitrary shapes of the tracks of the WG structure, numerical methods have to be employed to calculate the Fourier coefficients, including, when necessary, digital image processing of real structure cross-sections [72]. In the special case of cylindrical tracks (circular cross-sections), however, analytical expressions for the Fourier coefficients can be

found. Let Y denote any of $\eta_{o,e}$, $1/\eta_{o,e}$, with $Y(x,z) = Y_1$ if $(x,z) \in$ tracks and $Y(x,z) = Y_2$ if $(x,z) \in$ otherwise. For cylindrical tracks of radii r_i, one can obtain

$$Y_{m,n} = \begin{cases} \sum_i \frac{\pi r_i^2}{S} Y_1 + \left(1 - \sum_i \frac{\pi r_i^2}{S}\right) Y_2, & m = n = 0 \\ 2\pi \sum_i \exp\left[iG^x_{m,n} x_i + iG^z_{m,n} z_i\right] \frac{r_i^2}{S} \frac{J_1(r_i\sqrt{(G^x_{m,n})^2 + (G^z_{m,n})^2})}{r_i\sqrt{(G^x_{m,n})^2 + (G^z_{m,n})^2}} (Y_1 - Y_2), & m,n \neq 0 \end{cases} \tag{2.19}$$

Here S is the area of the surrounding box, J_1 is the Bessel function of the first kind, and x_i, z_i are the coordinates of the centre of the ith track.

2.2.2 Finite Element Method

A typical work out of the FE solution procedure [73–75] involves the following steps.

1. *Discretise the continuum.* The first step is to divide the solution domain (the cross section of the optical WG) into a number of subdomains or elements, usually triangles or quadrilaterals, creating a covering mesh (see Fig. 2.2). Elements can have various shapes, such as triangles or rectangles or even be with curved sides [76], and they can also be of various sizes. Triangles are commonly used because they are easy to adapt to complex shapes. The size of the elements defines the density of the mesh; smaller triangles increase the mesh density and therefore the model's accuracy. The trade-off for high accuracy is the exponential increment of both the calculation time and the computation capacity. A possible way of achieving optimum coverage of the domain concerned without a significant increase of the number of elements consists in using a non-uniform mesh. This way, it is possible to increase the density of the mesh only around the complicated areas or areas of special interest. The FE mesh is typically generated by a preprocessor program.

2. *Select shape functions.* Shape functions are used to interpolate the field variables over the element. Often, polynomials are selected as interpolation functions, with the degree of the polynomial depending on the number of nodes assigned to the element. However, the nodal-based FEM when applied to the vector wave equation results in nonphysical or spurious solutions [77]. The most elegant and simple approach to eliminate the disadvantages of the nodal-based elements is to use edge elements, which are FE bases for vector fields assigning degrees of freedom to the edges rather than the nodes of the element [78, 79].

3. *Find the element properties.* The matrix equation for the FE should be established, which relates the nodal and/or edge values of the unknown function to other parameters. Several approaches can be used to transform the physical formulation of the problem to its FE discrete analogue. If the physical formulation of the problem is known as a differential equation then the most popular method of its finite element formulation is the Galerkin method [80]. If the physical problem can be formulated as minimisation of a functional then variational formulation of the FE equations is usually used.

4. *Assemble the element equations.* To find the global equation system for the whole solution region we must assemble all the element equations. In other words we must combine local element equations for all elements used for discretisation. Element connectivities are used for the assembly process. Before solution, boundary conditions should be imposed.

5. *Solve the global equation system.* The FE global equation system has known solution techniques, and can be calculated from the initial values of the original problem to obtain a numerical answer.

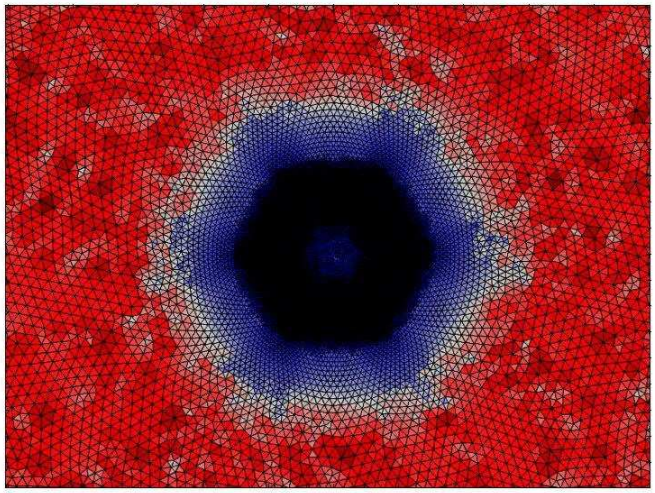

Figure 2.2: Mesh of a two-ring MS WG with an hexagonal geometry.

We now describe the formulation of the three-dimensional vector FEM for the analysis of WGs [50, 81]. This approach can be followed by using either the $\vec{E}$ or $\vec{H}$ field. We illustrate the case for the $\vec{E}$ field. The vector wave equation for the $\vec{E}$ field is given by (2.7), where $\vec{E} = (E_x\hat{x} + E_y\hat{y} + E_z\hat{z})\exp(-i\beta y)$. By doing the curl-curl operation and separating the transverse from the longitudinal components, Eq. (2.7) can be divided into two equations and rewritten as

$$\nabla_t \times (\nabla_t \times \vec{E}_t) - i\beta\nabla_t E_y + \beta^2\vec{E}_t = k_0^2\varepsilon_r\vec{E}_t,$$

$$-\nabla_t \cdot (\nabla_t E_y + i\beta\vec{E}_t) = k_0^2\varepsilon_r E_y, \tag{2.20}$$

and $\vec{E}_t = E_x\hat{x} + E_z\hat{z}$. Separate β from k_0^2 and to have real-valued matrices introduce the scaling $\vec{E}_t = \vec{E}_t/\beta$, $E_y = -E_y/i$. Then Eqs. (2.20) can be written as

$$\nabla_t \times \nabla_t \times \vec{E}_t + \beta^2(\nabla_t E_y + \vec{E}_t) = k_0^2\varepsilon_r\vec{E}_t,$$

$$-\nabla_t \cdot (\nabla_t E_y + \vec{E}_t) = k_0^2\varepsilon_r E_y. \tag{2.21}$$

To apply Galerkin's method to Eqs. (2.2.2), multiply the first and second equation with the respective testing functions $\vec{T}_t$ and T_y and integrate both the equations over the cross section

of the WG Ω; that is,

$$\iint_\Omega [\vec{T}_t \cdot \nabla_t \times \nabla_t \times \vec{E}_t + \beta^2(\vec{T}_t \cdot \nabla_t E_y + \vec{T}_t \cdot \vec{E}_t)]\,\mathrm{d}s = k_0^2 \varepsilon_r \iint_\Omega \vec{T}_t \cdot \vec{E}_t\,\mathrm{d}s,$$
$$-\iint_\Omega T_y[\nabla_t \cdot (\nabla_t E_y + \vec{E}_t)]\,\mathrm{d}s = k_0^2 \varepsilon_r \iint_\Omega T_y E_y\,\mathrm{d}s. \tag{2.22}$$

With the vector identities

$$\vec{A} \cdot (\nabla_t \times \vec{B}) = (\nabla_t \times \vec{A}) \cdot \vec{B} - \nabla_t \cdot (\vec{A} \times \vec{B}),$$
$$\iint_\Omega \nabla_t \cdot (\vec{A} \times \vec{B})\,\mathrm{d}s = \int_{\mathrm{d}\Omega} (\vec{A} \times \vec{B}) \cdot \hat{n}\,\mathrm{d}l = -\int_{\mathrm{d}\Omega} \vec{A} \cdot (\hat{n} \times \vec{B})\,\mathrm{d}l,$$
$$\nabla_t \cdot f\vec{A} = \vec{A} \cdot \nabla_t f + f \nabla_t \cdot \vec{A},$$
$$\iint_\Omega \nabla_t \cdot \vec{A}\,\mathrm{d}s = \int_{\mathrm{d}\Omega} \vec{A} \cdot \hat{n}\,\mathrm{d}l$$

Eqs. (2.2.2) can be written in their weak form as

$$\iint_\Omega [(\nabla_t \times \vec{T}_t) \cdot (\nabla_t \times \vec{E}_t) + \beta^2(\vec{T}_t \cdot \nabla E_y + \vec{T}_t \cdot \vec{E}_t)]\,\mathrm{d}s$$
$$= k_0^2 \varepsilon_r \iint_\Omega \vec{T}_t \cdot \vec{E}_t\,\mathrm{d}s - \int_{\mathrm{d}\Omega} \vec{T}_t \cdot (\hat{n} \times \nabla \times \vec{E}_t)\,\mathrm{d}s,$$
$$\iint_\Omega (\nabla_t T_y \cdot \nabla_t E_y + \nabla_t T_y \cdot \vec{E}_t)\,\mathrm{d}s = k_0^2 \varepsilon_r \iint_\Omega T_y E_y\,\mathrm{d}s + \int_{\mathrm{d}\Omega} \left(T_y \frac{\partial E_y}{\partial n} + T_y \hat{n} \cdot \vec{E}_t \right) \mathrm{d}s. \tag{2.23}$$

If the WG boundary $\mathrm{d}\Omega$ is assumed to be perfectly conducting, then $\vec{T}_t = 0$ and $T_y = 0$ on $\mathrm{d}\Omega$. Hence, the line integrals on the right-hand side of Eqs. (2.2.2) can be neglected, and Eqs. (2.2.2) can be written as

$$\iint_\Omega (\nabla_t \times \vec{T}_t) \cdot (\nabla_t \times \vec{E}_t)\,\mathrm{d}s - k_0^2 \varepsilon_r \iint_\Omega \vec{T}_t \cdot \vec{E}_t\,\mathrm{d}s = -\beta^2 \left(\iint_\Omega \vec{T}_t \cdot \nabla_t E_y\,\mathrm{d}s + \iint_\Omega \vec{T}_t \cdot \vec{E}_t\,\mathrm{d}s \right),$$
$$\beta^2 \iint_\Omega \nabla_t T_y \cdot \nabla_t E_y\,\mathrm{d}s + \beta^2 \iint_\Omega \nabla_t T_y \cdot \vec{E}_t\,\mathrm{d}s = k_0^2 \beta^2 \varepsilon_r \iint_\Omega T_y E_y\,\mathrm{d}s. \tag{2.24}$$

As the vector Helmholtz equation is divided into two parts, vector-based tangential elements can be used to approximate the transverse fields, and nodal-based Lagrangian interpolation functions can be used to approximate the y-component. As an example, we consider

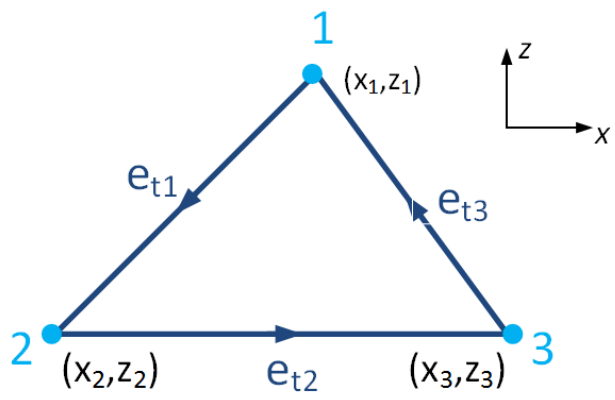

Figure 2.3: Configuration of a triangular element.

here first-order interpolation functions. For a single triangular element shown in Fig. 2.3, the edge elements permit a constant tangential component of the basis function along one triangular edge while simultaneously allowing a zero tangential component along the other two edges. Three such basis functions overlapping each triangular cell, provide the complete expansion:

$$\vec{E}_t = \sum_{m=1}^{3} e_{tm}\vec{W}_{tm} \tag{2.25}$$

where m indicates the mth edge of the triangle and $\vec{W}_{tm}$ is the edge element for edge m. The testing function $\vec{T}_t$ is chosen to be the same as the basis function in Eq. (2.25); that is, $\vec{T}_t = \vec{W}_{tm}$. The y-component is written as

$$E_y = \sum_{i=1}^{3} e_{yi}\alpha_i \tag{2.26}$$

where i indicates the ith node and α_i is the simplex coordinate of node i. Also the testing function $\vec{T}_y$ is chosen to be the same as the basis function in Eq. (2.26); that is, $\vec{T}_y = \alpha_i$.

Substituting Eqs. (2.25) and (2.26) into Eqs. (2.2.2), integrating over a single triangular element, and interchanging the integration and summation give

$$\begin{aligned}
&\sum_{m=1}^{3}\iint_{\Delta}(\nabla_t\times\vec{W}_{tm})\cdot(\nabla_t\vec{W}_{tn})e_{tm}\,\mathrm{d}s-k_0^2\sum_{m=1}^{3}\varepsilon_r\iint_{\Delta}(\vec{W}_{tm}\cdot\vec{W}_{tn})e_{tm}\,\mathrm{d}s\\
&=-\beta^2\left[\sum_{m=1}^{3}\iint_{\Delta}(\vec{W}_{tm}\cdot\nabla\alpha_j)e_{yj}\,\mathrm{d}s+\sum_{m=1}^{3}\iint_{\Delta}(\vec{W}_{tm}\cdot\vec{W}_{tn})e_{tm}\,\mathrm{d}s\right],\\
&\beta^2\sum_{i=1}^{3}\iint_{\Delta}(\nabla\alpha_i\cdot\nabla\alpha_j)e_{yi}\,\mathrm{d}s+\beta^2\sum_{i=1}^{3}\iint_{\Delta}(\nabla\alpha_i\cdot\vec{W}_{tn})e_{tn}\,\mathrm{d}s=\beta^2\sum_{i=1}^{3}k_0^2\varepsilon_r\iint_{\Delta}\alpha_i\alpha_j e_{yi}\,\mathrm{d}s\\
&\qquad(n=1,2,3;\ j=1,2,3).
\end{aligned}\tag{2.27}$$

Subscripts for α indicate node numbers and subscripts for $\vec{W}_t$ indicate edge numbers. Equations (2.27) can be written in matrix form as

$$\begin{bmatrix} S_{\mathrm{el}(tt)} & 0\\ 0 & 0\end{bmatrix}\begin{bmatrix} e_t\\ e_y\end{bmatrix}=-\beta^2\begin{bmatrix} T_{\mathrm{el}(tt)} & T_{\mathrm{el}(ty)}\\ T_{\mathrm{el}(yt)} & T_{\mathrm{el}(yy)}\end{bmatrix}\begin{bmatrix} e_t\\ e_y\end{bmatrix},\tag{2.28}$$

with the element matrices given by

$$\begin{aligned}
S_{\mathrm{el}(tt)}&=\iint_{\Delta}(\nabla_t\times\vec{W}_{tm})\cdot(\nabla_t\vec{W}_{tn})\,\mathrm{d}s-k_0^2\varepsilon_r\iint_{\Delta}(\vec{W}_{tm}\cdot\vec{W}_{tn})\,\mathrm{d}s,\\
T_{\mathrm{el}(tt)}&=\varepsilon_r\iint_{\Delta}(\vec{W}_{tm}\cdot\vec{W}_{tn})\,\mathrm{d}s,\quad T_{\mathrm{el}(ty)}=\iint_{\Delta}(\vec{W}_{tm}\cdot\nabla\alpha_j)\,\mathrm{d}s,\\
T_{\mathrm{el}(yt)}&=\iint_{\Delta}(\nabla\alpha_i\cdot\vec{W}_{tn})\,\mathrm{d}s,\quad T_{\mathrm{el}(yy)}=\iint_{\Delta}(\nabla\alpha_i\cdot\nabla\alpha_j)\,\mathrm{d}s-k_0^2\varepsilon_r\iint_{\Delta}\alpha_i\alpha_j\,\mathrm{d}s.
\end{aligned}\tag{2.29}$$

These element matrices can be assembled over all the triangles in the cross section of the WG to obtain a global eigenvalue equation,

$$\begin{bmatrix} S_{tt} & 0\\ 0 & 0\end{bmatrix}\begin{bmatrix} e_t\\ e_y\end{bmatrix}=(-\beta^2)\begin{bmatrix} T_{tt} & T_{ty}\\ T_{yt} & T_{yy}\end{bmatrix}\begin{bmatrix} e_t\\ e_y\end{bmatrix},\tag{2.30}$$

which can be solved to obtain β when the operating frequency is specified.

Within this thesis, the execution of the FEM to compute the modal properties of MS WGs has been realised via the commercial modelling software “COMSOL Multiphysics”.

This software enables the definition of any MS WG geometry, material properties and type of Maxwell's equations in either their general or weak form via a graphical interface or the Matlab software. It can generate a mesh geometry based on user-defined geometrical properties, such as mesh element geometry, maximum and minimum element size, growth rate from minimum to maximum, and others. Based on the user-defined parameters, the software creates an eigenvalue matrix equation and start to solve it around a user-defined approximate propagation constant (β) at a specified wavelength. The solution space includes the electric and magnetic fields over the WG cross section, and the complex propagation constants corresponding to different modal distributions. The spatial modes of the electric field in the WG structure have been characterised by the mode field pattern. The most compact, Gaussian-like mode has been selected as the fundamental mode of the structure according to the criterium of 'minimum effective mode area'.

Perfectly matched layer

One of the most important aspects of FD and FE implementations is the truncation of the computational domain. An ideal truncation scheme must ensure that outgoing waves are not reflected backwards at the mesh termination surface, i.e. the mesh truncation scheme must simulate a surface which actually does not exist. The first attempts at non-reflecting or absorbing boundaries for wave equations involved absorbing boundary conditions (ABCs) [82, 83]. Given a solution on a discrete grid, a boundary condition is a rule to set the value at the edge of the grid. For example, a simple Dirichlet boundary condition sets the solution to zero at the edge of the grid (which will reflect waves that hit the edge). An ABC tries to somehow extrapolate from the interior grid points to the edge grid point(s), to fool the solution into 'thinking' that it extends forever with no boundary. However, existing

ABCs restrict themselves to absorbing waves exactly only at a few angles, especially at normal incidence: as the size of the computational grid grows, eventually normal-incident waves must become the dominant portion of the radiation striking the boundaries. Another difficulty is that many standard ABCs are formulated only for homogeneous materials at the boundaries, and may even become numerically unstable if the grid boundaries are inhomogeneous.

In 1994, the problem of absorbing boundaries for wave equations was transformed in a seminal paper by Bérenger [84]. Instead of finding an absorbing boundary condition, Bérenger found an absorbing boundary layer, that is, a layer of artificial absorbing material that is placed adjacent to the edges of the grid, completely independent of the boundary condition. When a wave enters the absorbing layer, it is attenuated by the absorption and decays exponentially; even if it reflects off the boundary, the returning wave after one round trip through the absorbing layer is exponentially tiny. The problem with this approach is that, whenever we have a transition from one material to another [85], waves generally reflect, and the transition from non-absorbing to absorbing material is no exception – so, instead of having reflections from the grid boundary, we now have reflections from the absorber boundary. However, Bérenger showed that a special absorbing medium could be constructed so that waves do not reflect at the interface for all incidence angles: a perfectly matched layer (PML). There are several nearly equivalent formulations of PMLs. Bérenger's original formulation is called the split-field PML, because he artificially split the wave solutions into the sum of two new artificial field components. Nowadays, a more common formulation is the uniaxial PML, which uses a special uniaxial anisotropic absorbing medium introduced into the ordinary (un-split) wave equation [85]. Further, both the split-field and uniaxial PML formulations can be viewed as the result of a complex coordinate stretching [86–88].

This complex-coordinate approach is essentially based on analytic continuation of Maxwell's equations into complex spatial coordinates where the fields are exponentially decaying. PML absorbers offer ease of implementation coupled with excellent absorption characteristics [84]. Unlike ABCs, PML truncation schemes do not require *a priori* knowledge of propagation constants within the computational domain, and the use of boundary derivatives is avoided altogether. Also, PML termination schemes facilitate de-embedding and parameter extraction [89]. Because of these advantages, PML absorbers have been extensively employed for truncating FEM domains. However, the inclusion of PML absorbers within the computational domain in general deteriorates the condition of the resulting FEM systems, thus PML-truncated meshes typically are quite slow to converge. It is therefore important to choose the PML parameters in an optimal manner, so that speedup in the solution convergence can be achieved without affecting PML absorption.

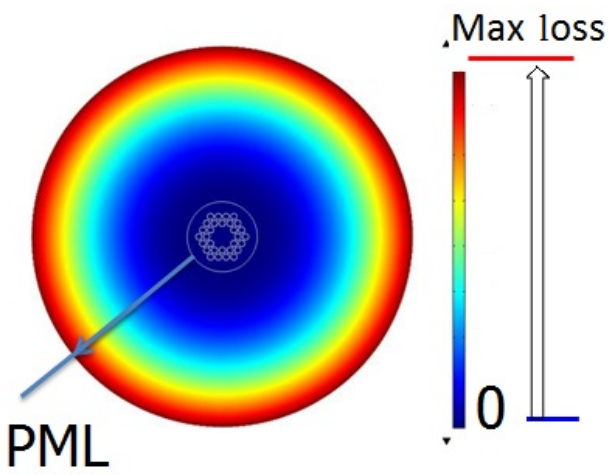

Figure 2.4: Cross section of MS WG surrounded by a circular PML.

In our numerical simulations, we chose a circular PML surrounding the cross-section of the WG structure and isotropic in its absorption, as shown in Fig. 2.4. This artificial absorbing layer is designed in such a way that the real part of the RI over its region is the

same as that of the unmodified material, whereas the imaginary part, κ, increases from zero at the inner edge to a maximum value at the outer edge, thereby introducing a gradually increasing loss mechanism. The RI profile of the PML is therefore defined by [90]

$$n_{\mathrm{PML}}(r) = n_{o,e} - i\kappa_{\max}\left(\frac{r - r_{\mathrm{in}}}{L}\right)^2, \quad r_{\mathrm{in}} < r \leq r_{\mathrm{in}} + L \tag{2.31}$$

where r is the polar radial coordinate, r_{in} and L are the respective inner radius and thickness of the PML, and $\kappa_{\max}$ is the maximum absorption value, which is assumed to be wavelength independent.

Outside the absorbing regions, where $\kappa = 0$, the wave equation and thus the solution are unchanged, and it is only inside the absorbing region that the oscillating solution becomes exponentially decaying. In the exact wave equation, this transition occurs with no reflections, no matter how fast κ changes, even if κ changes discontinuously. As soon as we discretise the problem, we are only solving an approximate wave equation and the analytical perfection of PML is no longer valid. PML is still an absorbing material: waves that propagate within it are still attenuated, even discrete waves. The boundary between the PML and the regular medium is no longer reflectionless, but the reflections are small because the discretisation is (presumably) a good approximation for the exact wave equation. It turns out that, even without a PML, reflections can be made arbitrarily small as long as the medium is slowly varying. That is, in the limit as we turn on absorption from zero more and more slowly, reflections go to zero due to an adiabatic theorem [91]. With a non-PML absorber, we might need to go very slowly (i.e. a very thick absorbing layer) to get acceptable reflections. With PML, however, experience shows that a quadratic or cubic turn-on of the PML absorption over some length L usually produce negligible reflections [92]. In [93], the computational error was estimated to scale down with the PML's thickness approximately as $1/L^8$ for

the case of a quadratic turn-on of the PML absorption as given in (2.31). Increasing the resolution also increases the effectiveness of the PML, because it approaches the exact wave equation. Therefore, the trade-off in the optimisation of the PML's parameters $\kappa_{\max}$ and L is between minimisation of the computational error and minimisation of the random memory access requirements.

2.2.3 Validation of FEM results

In order to confirm the accuracy of our numerical model for the analysis of MS WGs in anisotropic crystals we simulated known micro-structured optical fibre (MOF) structures. From the discussion above, other than from the use of different computational methods, differences in simulation results are likely to stem from the choice of the PML parameters and the computational mesh. The PML settings used throughout this thesis are described in Chapter 4. The mesh size must be a few times smaller than the wavelength in use to ensure good accuracy of the results. This was adjusted so to be as small as possible with the only limitation of computer capacity. Examples of comparison of calculations of the confinement loss in two different MOF structures are shown in Figs. 2.5 and 2.6. The standard Sellmeier equation

$$n^2(\lambda) = 1 + \frac{A_1\lambda^2}{\lambda^2 - B_1^2} + \frac{A_2\lambda^2}{\lambda^2 - B_2^2} + \frac{A_3\lambda^2}{\lambda^2 - B_3^2}$$

was used to model the dispersion relation for pure silica with the following Sellmeier coefficients [49]:

A_1	A_2	A_3
0.6961663	0.4079426	0.8974794
B_1	B_2	B_3
0.0684043	0.1162414	9.896161

Table 2.1: Sellmeier coefficients for pure silica.

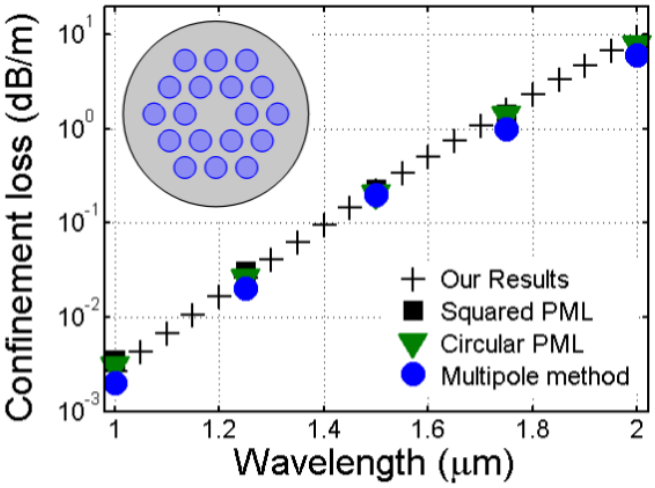

Figure 2.5: Comparison of our calculations with: the FEM calculations of [94] using a squared PML, the FEM calculations of [95] using a circular PML, and the MM calculations of [67], for an MOF with two layers of air holes.

The core of the first MOF (Fig. 2.5) is made of silica, and the cladding region consists of two layers of air holes with a diameter of 1.61 μm and separated by a pitch of 2.3 μm. Our calculations are compared with the calculations of [94] using the FEM and a square PML, those of [95] using the FEM and a circular PML, and those of [67] based on the MM. We can see that in the wavelength range 1 to 2 μm our values of confinement loss are of the same order of magnitude as those obtained in the other works. Our results for confinement losses at the wavelengths of 1, 1.5 and 2 μm are 2.675×10^{-3}, 2.22×10^{-1} and 9.1 dB/m, respectively. The results reported in [67] by using the MM are 3.06×10^{-3}, 2.06×10^{-1} and 7.73. The results reported in [94] by using the FEM and a square PML are 2.00×10^{-3}, 2.00×10^{-1} and 6 dB/m. The results reported in [95] by using the FEM and a circular PML are 3.47×10^{-3}, 2.26×10^{-1} and 7.74 dB/m. Those results show that the maximum rate of difference between our results and the confinement loss results of other computations goes to % 50 at 2 μm wavelength.

The structure of the second MOF is given in Fig. 2.6(a). The cladding of this fibre is

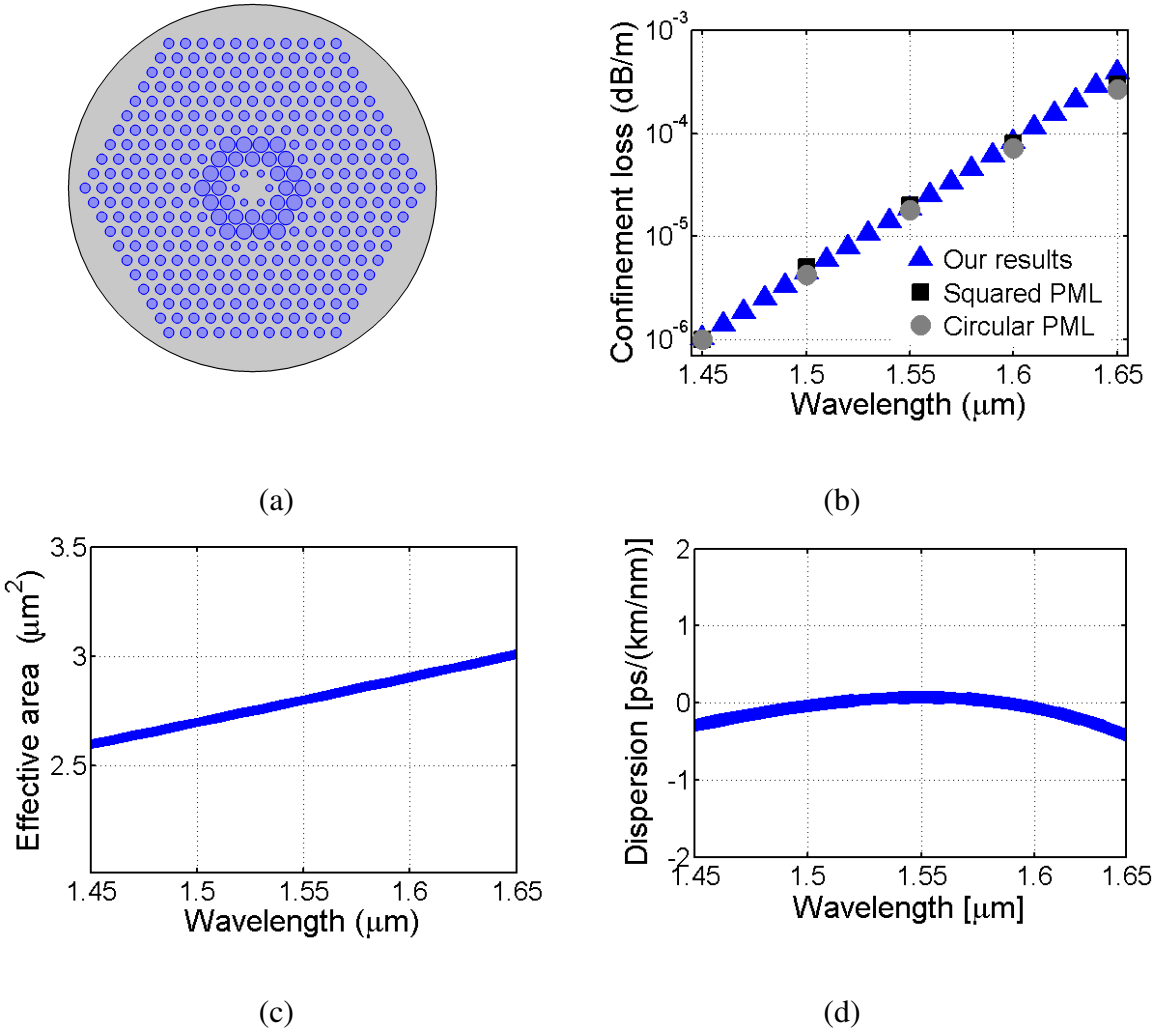

Figure 2.6: (a) Cross section of MOF with ten layers of air holes. (b) Comparison of our calculations of confinement loss with: the FEM calculations of [96] using a squared PML and the FEM calculations of [95] using a circular PML. (c), (d) Computed MOF dispersion and effective area.

composed of ten layers of air holes separated by a pitch of 0.89 μm. The diameter of the air holes is the same for a given layer, but varies from layer to layer. The diameter values from innermost to outermost layer are: 0.41 μm, 0.85 μm, 0.92 μm, 0.53 μm, and 0.60 μm for the following six layers. Our calculations are compared with the FEM calculations of [96] using a squared PML and the FEM calculations of [95] using a circular PML. Again, all results are very close to each other, and variations of confinement loss are very small.

Our results for confinement losses at the wavelengths of 145, 1.55 and 1.65 μm are

1.046×10^{-6}, 1.895×10^{-5} and 3.92×10^{-4} dB/m, respectively. The results reported in [94] by using the FEM and a square PML are 1.00×10^{-6}, 2.00×10^{-5} and 3×10^{-4} dB/m. The results reported in [95] by using the FEM and a circular PML are 1.00×10^{-6}, 1.8×10^{-5} and 2.65×10^{-4} dB/m. While our results at 1.45 and 1.55 μm wavelengths are between the values of other two computations, it is around %50 higher at 1.65 μm wavelength than the lower value of other computation results. Furthermore, we have also plotted the WG dispersion and effective area of the fundamental mode for this fibre as obtained in our numerical model (Figs. 2.6(c) and 2.6(d)).

2.3 Summary

This chapter gave a detailed account of the theoretical approaches to the modelling of MS WGs in anisotropic crystals that are employed in the remainder of this thesis. The FEM and PWM for the modal analysis of these WGs have been described. The accuracy of the FEM calculations performed by using the COMSOL Multiphysics software has been validated by comparing our results to previously reported results for MOFs.

Chapter 3

Experimental background

The design and optimisation of MS WGs in $LiNbO_3$ crystals necessitate the use of available parameters related to track structures for any fabrication purpose. Therefore, it is worth first evaluating the fs laser inscription method and its use in $LiNbO_3$, and then introducing experimentally obtained operational parameters [45]: track sizes and RI contrasts, which have been used in this theses.

3.1 Direct femtosecond laser inscription method

Dielectric transparent materials allow the transmission of low intensities of light without any significant absorption due to wide gaps between the valence and conduction bands. However, interactions between light and transparent materials may become triggered due to nonlinear effects such as multiphoton absorption, avalanche ionization and plasma formation at very high intensities of light, which is only available by use of spatially and temporally confined high energies of ultra-short laser pulses. As such, tight focusing of fs laser pulses inside a small volume of transparent materials leads to localised and permanent changes of material

properties such as RI, absorption coefficient, susceptibility, crystal structure, and so forth. Choosing proper light sources for permanent modification of RIs at specific intensities and wavelengths with a micron size precise spatial control over a focal area inside bulk materials, and continuous translation over multiple axes of 3D space allow for micro-fabrication of complex IOC devices. Being developed over two decades into a research field to understand the underlying phenomena, to optimise photo-induced structural modifications on various transparent materials, and to exploit its capabilities on the micro-fabrication of a multitude of optical devices, the direct fs laser inscription method [97, 98] has been considered as a valuable alternative to more mature fabrication technologies due to the flexibility and robustness of 3D volume micro-structuring of transparent dielectric materials.

The first demonstration of reproducible permanent RI modification by direct fs laser writing was reported for bulk glasses in [99]. Since then, it has been implemented on a variety of transparent materials such as polymers [22], amorphous and chalcogenide glasses [100], crystalline materials [101], dielectric crystals [37, 102, 103] to fabricate buried WGs [102, 104], lasers [37], amplifiers [105, 106], couplers [107], splitters [108], gratings [109], computer holograms [110], and many more. All those devices utilise the modification of RIs of transparent dielectric materials, which results from a combination of a highly complex physical processes.

Fs laser induced RI changes depend on the properties of both material and fs laser source, as well as focusing conditions. The availability of fs laser sources is the primary factor leading to any ability to change material structure because it provides with high intensity levels of light pulses required to start any physical process. Fs light sources can be focused in a focal area inside the material by using a micro objective (MO). Numerical aperture (NA) of the MO, a measure of the range of angles that light is emitted, needs be correctly

chosen not just to adjust the width and depth of the focal area also not to cause any high intensity dependent nonlinear processes such as self-focusing and white-light generation because of Kerr effects, diffraction and dispersion during the propagation of light pulses [111, 112]. The nonlinear nature of absorption in a material is the mechanism triggering a process leading to controllable and small volumes of structural changes, so that any other part including the surface of material do not become affected by laser light except focal area in which pulses reach enough intensity. Depending on band-gap energy of material, an electron moves from valence band to conduction band if sufficient multiple number of photons incident at the same time on any electron is absorbed, which is called multi-photon absorption [97]. Only if the NA of MO, pulse width, wavelength and energy of laser is chosen properly, a nonlinear absorption mechanism takes place and creates a seed of electrons at high energy levels [113]. Those free electrons at conduction band can subsequently acquire extra energy and accelerate by linearly absorbing the incoming photons. As soon as their accumulated kinetic energies is over band-gap energy, other electrons at valence band acquire this extra energy and move also to conduction band [114]. The number of free electrons increase exponentially as in an avalanche effect, leading to absorption of the remaining pulse energy and plasma formation. Part of the accumulated energy in a focal volume transfers to the lattice through carrier-carrier and carrier-phonon scattering, leading to thermalisation and a hot focal volume [113]. Subsequently, accumulated energy leaves out the focal volume through shock wave generation and heat diffusion to outside of the focal area; meanwhile causing the RI modification of the material structure through several mechanisms such as stress-induced changes, densification, color centre formation [113]. RI modifications reported for different transparent materials under various experimental conditions have been varying from 10^{-4} to 10^{-2} [97]. An exact model which can quantify the

highly complex interdependence of different physical processes do not exist to identify the properties of material changes, even though there exist several numerical works to evaluate the effects of separate system parameters [25, 112, 115]. Thereby, fabrication of optical devices by fs laser inscription becomes an experimental optimisation problem within a parameter space: wavelength of fs light source, pulse energy, polarisation, spatial and temporal pulse shape, repetition rate of the laser system, NA of the MO used, depth of focusing and the aberrations of the laser wavefront and sample translation speed.

Irradiation of fs laser pulses in dielectric crystals may produce both negative [103, 116] and positive RI changes [37], depending on the experimental parameter settings during the fs laser inscription. While single line tracks can be used as WGs because it can confine light in core regions with positive RI changes, light propagation along single written tracks can not be accomplished with negative RI changes. However, confinement of light by use of multiple number of single line tracks with negative RI changes is also possible by designing MS buried WGs in such a way that a depressed-index cladding which consists of a certain number of tracks with negative RI changes can be inscribed around an unmodified area of material which serves as the core of WG [37, 103]. It is possible, in principle, that advanced designs of light guiding channels consisting of tracks with negative RI changes can be achieved to reduce propagation losses [97, 117]. But, the question of how good confinement can be achieved by the implementation of this approach arises due to the fact that depressed-index cladding WGs inherently have leaky-mode properties [118], specifically on the conditions that cladding region of depressed-index MS WGs may consists of a limited number of tracks, and that RI contrasts which can be achievable by current fs laser inscription technology between tracks and unmodified core region are relatively small. Simplest depressed-index claddings which have often been fabricated to date consists of either just two parallel tracks

or a single layer of tracks surrounding the unmodified core region. Those simple geometries can not effectively confine light and generally suffer from high propagation losses [117]. Additionally, these geometries do not allow for any control over wave-guiding properties, such as confinement loss, WG dispersion, WG birefringence, insertion/coupling loss, effective area and so on. Therefore, a large number of tracks with advanced design geometries need to be configured to effectively lower confinement losses, and, ideally, to control the WG parameters.

As the number of tracks necessary to provide a better confinement increases, laser writing duration becomes a limiting factor in terms of fabrication of complex depressed-index cladding MS WGs. Repetition rate of fs laser sources is one of the most important parameters to improve the fabrication time of tracks. Even tough the structural deformations by one-by-one energy deposition of separate fs laser pulses are a rather complex process, the use of fs laser sources with low repetition rates, in practice, leads to longer inscription times and becomes a limiting factor. As it is currently employed the most widely for WG inscription in crystals, kHz fs laser systems use typical sample translation speeds from ten to a few hundred μm/s. In comparison, fs laser sources with high repetition rates (HRR) enable much faster fabrication times because higher number of pulses per unit time can be deposited into a focal region, leading to a fast accumulation of heat and therefore faster translation speeds [20, 119]. HRR fs laser sources have already been preferred for the fabrication of low-loss WGs in glasses [20, 120–123] because it enables up to five times higher RI contrasts between exposed and unexposed regions than those of what are the maximum RI contrasts achieved by LRR fs systems [20]. However, the use of HRR fs laser sources for the inscription of crystals has got less attention in the literature [104]. It was shown that the energy absorption efficiency of laser inscription with HRR lasers can be twice more than that with low repetition

rate lasers due to heat accumulation effect [120, 121], which permits even faster translation speeds. Since the time difference between successive pulses of HRR lasers are less than the time for heat dissipation, heat accumulation is sustained throughout laser cycles in the focal volume leading to a melting of the material [34]. Molten material starts cooling from outside, resulting in smooth track formations with permanent RI change. Definitely, the repetition rate is one of the key parameters to optimise permanent material modification. If optimised results can be obtained by using HRR laser systems, faster energy deposition into the focal volume reduces the fabrication time of tracks; thereby making the fabrication of a large number of tracks feasible for complex depressed cladding MS WGs.

3.1.1 Direct femtosecond laser inscription in Lithium Niobate

Fs laser inscription method in z-cut $LiNbO_3$ was demonstrated for the first time to fabricate 3D optical WGs and a Y splitter by Gui in 2004 [30, 31]. A positive RI change of around 6×10^{-4} for elliptically shaped tracks was reported by using a fs laser system producing 150 fs pulse-width of laser pulses with a repetition rate of 1 kHz at 775 nm wavelength. Circularly polarised fs laser beam with average pulse energy of 10 μJ was focused ≈ 500 μm under the surface by using a 20$\times$ MO with 0.4 NA and translation stage is moved with a velocity of 50 μm/s. Propagation losses were estimated to be around 1 dB/cm at 632.8 nm of wavelength [31].

Thomson [124] *et al*. reported the WG fabrication of z-cut $LiNbO_3$ to demonstrate well-confined propagation at 1550 nm. A 5 kHz laser system emitting 130 fs pulses at 800 nm wavelength was used. Fs laser beam linearly polarised parallel to the x axis was focused at ≈ 250 μm below the surface by using 20$\times$ MO with 0.4 NA. It was reported that WGs

fabricated by using pulse energies from 0.1 to 40 μJ and translation speeds less than 5 μm/s supported propagation at 1550 nm of wavelength. In his following report [32], Thomson presented further characterisation results with the aim of producing high confinement at 1550 nm. The same laser system and focusing optics set-up but pulses with a duration of 520 fs were used. Guiding was reported to be observed at 1550 nm when pulse energies was between 300 to 400 nJ and to be improving with lower translations speeds. However, it was later seen that guiding deteriorates over time with no guiding after 1 month. Thomson also reported the formation of two different types of waveguides; first type supporting the propagation of both polarisation state of light around central laser damage region and the second type supporting highly polarisation sensitive guiding with confinement of only one polarisation state which was perpendicular to material surface in the laser focus modification region.

Burghoff *et al*. [35] reported the observation and discussion of different types of modifications in $LiNbO_3$, as well as frequency doubling of 1064 nm using birefringent phase matching. A laser system producing 1 kHz repetition rate of 40 fs pulses at 800 nm was used. Laser beam was focused 200 μm below the surface by using 40$\times$ MO with a NA of 0.65. Linearly polarised laser beam with 500 nJ pulse energy was translated at 100 μm/s. Inscription of both x nd z-cut samples by applying an energy below 500 nJ produced tracks which guides only one polarisation state of light and which vanished after heating to 150 °C for 1.5 hours. When pulse energies above 500 nJ was applied on x-cut sample, guiding was not seen on damaged material with reduced RI at the focal point, but guiding of both polarisation states was supported through the sides of focus with no vanishing after heating to 150 °C for several hours. Frequency doubling experiment was realised by fabricating a WG which

located between two parallel tracks with reduced RIs.

In his paper [34], Nejadmalayeri *et al*. included the effects of pulse-widths and polarisation of pulses into the optimisation of track properties in z-cut $LiNbO_3$. A laser system capable of producing 2.5 W average power and 1 kHz repetition rate of 35 fs pulses at 800 nm was used. Laser beam was focused around 70 μm below the surface by using an aspheric lens with 0.5 NA. Circular and linear polarisation parallel and perpendicular to scan direction, pulse widths from 50 fs to 1 ps, pulse energies from 250 to 800 nJ and scan speed from 0.1 to 2 mm/s constituted the optimisation parameters. By using circularly polarised light with 1 ps pulse duration, fabrication of 0.7 dB/cm low loss tracks with positive RIs was reported at telecommunication band with strong modal polarisation dependence. It was reported that no depreciation of the WGs quality was observed after keeping in room temperature conditions for 5 weeks. However, those WGs disappeared after applying a temperature test of 8 hours slow heating to 450 °K over, keeping at this temperature for 24 hours and slow cooling to room temperatures over 8 hours.

Lee *et al*. [33] demonstrated optical WGs fabricated in periodically poled $LiNbO_3$ (PPLN) for second harmonic generation. A fs laser system supplied 1 kHz repetition rate of pulses with 130 fs pulse duration and 400 nJ pulse energy at 781 nm of wavelength. Laser beam was focused approximately 20 μm below the surface by an objective lens with 0.4 NA and translated with a velocity of 10 μm/s. Beam translation was translated 6 times with a line spacing of 0.7 μm to broaden WG to about 4.7 μm. Guiding was observed for just one polarisation state of light and propagation loss were measured to be 2.25 dB/cm at 1550 nm.

Burghoff *et al*. investigated the influence of processing and focusing parameters on the structural modifications induced in $LiNbO_3$ by fs laser writing [125]. A laser system operating at 1 kHz repetition rate of 40 fs duration of pulses at 800 nm of wavelength was

used. Laser pulses with 380 fs duration, 0.2 μJ energy and with 420 fs duration, 1 μJ energy were focused at a depth of 100 μm and 130 μm on x-cut and z-cut $LiNbO_3$ samples by using a 40× MO with 0.65 NA, respectively. Polarisation was linear and perpendicular to scanning direction. x-cut $LiNbO_3$ was written in the y direction. Translation velocity was kept constant at 100 μm/s. Two different types of structural modification were reported. First, a positive RI increase along E polarisation direction was observed at low laser fluences, which was thermally unstable and the electro-optic coefficient was substantially reduced. Second, a RI decrease along both polarisation directions accompanied by material damage and stresses in the surrounding regions was observed at high laser fluences. The discussion concluded that decreased RI regions can be used to fabricate symmetrically confined WGs by writing two parallel lines. In his following work [36] with similar experimental settings, using a pulse duration of 420 fs and a pulse energy of 1 μJ, a different behavior was observed in both polarisations. A decreased RI at the center and positive RI changes at the sides were observed along the E polarisation direction while it was just a decreased RI along O polarisation direction. After a thermal treatment at 200 °C for 30 minutes, positive RI changes disappeared and negative RI changes slightly increased along both polarisation directions. It was shown that two different modification types were obtained by changing just pulse duration. The RI increase along E polarisation was associated with moderate laser fluences and short pulse durations which generated small structural changes. The second type modification with decreased RI changes along both polarisation directions was associated with high laser fluences and long pulse durations around 1 ps. Burghoff *et al*. [126] also demonstrated the use of an optical WG consisting of two parallel tracks with reduced RIs and with 17 μm separation from each other for second harmonic generation of 1064 nm laser irradiation. The shape and polarisation dependence of propagation modes over those

WGs were modeled by FEM simulations and seen to be in agreement with experimental results [29].

Thomas *et al*. [42] reported the fabrication of symmetric and thermally stable optical WGs formed between two tracks in z-cut PPLN for a second harmonic generation of 1064 nm wavelength of light by using a quasi-phase matching approach. A laser system operating at 800 nm wavelength and 1 kHz repetition rate was used. Circularly polarised pulses with 2.5 ps pulse duration and 0.4 μJ pulse energy were focused 50 μm under the surface by using a 40$\times$ MO with 0.65 NA. Focus point was translated at a velocity of 800 μm/s.

HRR fs laser pulses was applied for the inscription of $LiNbO_3$ by Nejadmalayeri *et al*. [119]. A fiber based chirped laser system which provided minimum pulse duration of 400 fs at 1045 nm wavelength with variable repetition rate from 0.1 to 5 MHz was used. Both linearly and circularly polarised beams were examined. Pulses with 600 fs pulse duration were focused 110 μm below the surface with an aspheric lens having 0.55 NA. After examinations by changing pulse energy, scanning speeds from 1 to 80 mm/s, polarisation and repetition rate, best results were obtained for positive RI modifications of tracks along E polarisation direction at 1300 nm wavelength of light when scan speed, pulse energy, polarisation and repetition rate were, 46 mm/s, 500 nJ/pulse, circular and 700 kHz, respectively. Thermal stability of WGs were not tested. It was also reported that heat accumulation effects due to higher repetition rates were the cause of smooth WG formation.

Huang *et al*. [127] investigated the tuning characteristics of fs second harmonic generation in WGs formed between double tracks with reduced RIs in PPLN. Linearly polarised pulses with 50 fs pulse duration, 10 μJ pulse energy and 1 kHz repetition rate at 800 nm of wavelength were focused 200 μm below the surface by a 25$\times$ MO with 0.4 NA and were translated at a velocity of 400 μm/s.

Thomas [28] demonstrated a combination of a frequency doubling unit and a Match-Zehnder modulator on a single chip to convert 1.06 μm wavelength of light to 0.53 μm and to modulate. WGs for both units were formed between two tracks with reduced RI indices around 30 to 50 μm below the surface. First unit was designed for converting laser irradiation from 1064 μm to 532 μm by second harmonic generation in z-cut PPLN. The WG was designed for sustaining the guidance of fundamental mode at both of the wavelengths. A total conversion efficiency of 58% was achieved thanks to the unchanged electro-optic coefficient of the core region and to a good overlap of fundamental modes. A Match-Zehnder modulator was formed in x-cut $LiNbO_3$ by two y-junctions combined by double-track WGs. A tapered section was added to the modulator for higher-order modes filtering, and propagating lights in both arms was modulated by gold-coated surface electrodes. A modulation depth upto 11 dB was achieved at 80 Hz with a half voltage of 23 V at 532 nm of wavelength.

Horn *et al*. reported the fabrication of first-order WG Bragg gratings by fs laser writing in x-cut $LiNbO_3$ and demontrated the electro-optic tuning of narrowband reflections around a 1550 nm wavelength of light by an external electric field. Bragg gratings were structured between two tracks with negative RI changes which function as an optical WG. A laser system producing 1 kHz repetition rate of 120 fs duration of pulses at 800 nm was used. Linearly polarised pulses with an energy of $400-600$ nJ was focused at a depth of 250 μm by using a $100\times$ MO with 0.9 NA and translated at a speed of 30 μm/s to write two paralel tracks separated 7 to 15 μm from each other.

He *et al*. [44] demonstrated the fabrication of depressed cladding WGs in x-cut $LiNbO_3$ crystal with a circular geometry of one layer of tracks, which was written by linearly polarised pulses of 120 fs duration at a 1 kHz repetition rate and at the wavelength of 800 nm. 4 different WGs was fabricated, two of which were written along z axis with 50 μm and 110 μm

of circular diameters of core regions by using a pulse energy of 2.1 μJ, and other two of which were written along x axis with the same diameters of core regions by using a 5.04 μJ pulse energy. The laser beam was focused at a maximum depth of 150 μm by using a 20$\times$ MO with 0.4 NA, and scanned at a velocity of 0.5 mm/s. Separation distances between tracks was set to 3 μm. Depressed-cladding WGs with 50 μm of circular diameter showed a single-mode propagation at 4 μm wavelength of light, while it was multi-mode at 0.633 and 1.064 μm wavelengths. Minimum insertion losses including coupling and propagation losses in 10 mm long WG written along z direction with a diameter of 110 μm were estimated to be 1.0 dB, 0.5 dB and 3.0 dB at 0.633 μm, 1.064 μm and 4 μm wavelengths. It was seen that those WGs support confinement along both polarisation directions.

	Year	λ (μm)	P	PW (fs)	PE (μJ)	RR (kHz)	TS (mm/s)	NP	Cut	Type	Depth (μm)	δn	Loss (dB/cm)
Gui *et al*. [30]	2004	775	C	150	10	1	0.05	20	z	I	500	$6 \cdot 10^{-4}$	1 / 632.8 μm
Thomson *et al*. [32,124]	2005	800	L	520	0.4	5	0.02	250	z	I	250	*	9 / 650 μm
Burghoff *et al*. [35,126]	2006	800	L	40	18	1	0.1	10	x	II	200	$-12 \cdot 10^{-4}$	2.4 / 1064 μm
Nejadmalayari *et al*. [34]	2006	800	C	1000	0.7	1	0.9	1.1	z	I	70	*	0.7 / 1300 μm
Nejadmalayari *et al*. [34]	2006	800	C	1000	0.7	1	0.62	1.6	z	I	70	*	1 / 1550 μm
Lee *et al*. [33]	2006	781	*	130	0.4	1	0.01	100	*	I	20	*	2.25 / 1550 μm
Thomas *et al*. [42]	2007	800	C	2500	0.4	1	0.8	1.25	z	II	50	$-2 \cdot 10^{-4}$	1.2 / 1064 μm
Nejadmalayari *et al*. [119]	2007	1045	C	600	0.5	700	46	15.2	z	I	110	*	0.6 / 1300 μm
Osellame *et al*. [128]	2008	1030	L	350	0.37	600	4	150	z	I	250	$1 \cdot 10^{-3}$	0.6 / 1550 μm
Huang *et al*. [127]	2010	800	L	50	10	1	0.4	2.5	z	II	200	$3 \cdot 10^{-3}$	0.8 / 1550 μm
Horn *et al*. [27]	2012	800	L	120	0.6	1	0.03	33.3	x	II	250	*	*
He *et al*. [44]	2013	800	L	120	2.1	1	0.5	2	x	III	150	$-4.1 \cdot 10^{-3}$	4.3 / 4000 μm

Table 3.1: A comparison of experimental settings used by various researchers during fs laser inscription in $LiNbO_3$. P: Polarisation (L: Linear, C: Circular), PW: Pulse width, PE: Pulse energy, RR: Repetition rate, TS: Translation speed, NP: Number of pulses per μm . (* indicates missing information)

To summarise, WG fabrication in $LiNbO_3$ by using fs laser inscription method has been experimentally studied by various research groups with different experimental settings and fabrication parameters, which are given in Table 3.1 for comparison purposes. Taking into account different forms of RI changes, WGs have been classified as: Type-I WG which is a single line track supporting the confinement of light with increased RI changes, Type-II WG which supports the propagation of light between double-line parallel tracks with decreased

RIs in the focal regions of tracks and stress induced small and positive RI changes in between, and Type-III WG on which light propagates in an unchanged core region surrounded by multiple number of tracks with negative RI changes. Exact reasons and specific experimental settings leading to the formation of different kinds of RI changes and WGs have not clearly been identified yet. Optimisation efforts to improve WG properties, as can be seen in Table 3.1, have mostly been conducted experimentally by varying pulse energies, pulse widths, focus depths or translation speeds.

Type-1 WGs have the practical advantage of single line writing for the fabrication of complex IOC circuits. However, those WGs intrinsically have the disadvantages of confinement along just one polarisation direction, degradation of nonlinear properties during fs laser inscription and stability of RI changes at room or higher temperatures especially over 150 °C [34,35,128]. Most of the research efforts have been implemented by using low-repetition-rate fs laser systems. On the other hand, the first use of a HRR laser system was reported by [119] for a Type-I WG fabrication in $LiNbO_3$, achieving a lowest loss value of 0.6 dB/cm at telecommunication wavelengths, and a general trend towards lower losses by increasing repetition rates can be seen in Table 3.1. Interestingly, Type-II and Type-III WGs have only been reported by using low repetition rate laser systems. Especially, type-III WGs are advantageous due to symmetric mode propagation, conservation of nonlinear properties due to propagation in an unmodified region, RI changes along both polarisation directions and corresponding confinement of both polarisation states of light, and possibility to design MS WGs which can allow to control propagation properties. The decrease of the RI in $LiNbO_3$ can be explained as an amorphisation of the material in the focal area by heat accumulation and subsequent densification of the surrounding region. Also, time for heat diffusion out of the near-focal region has been assumed to be around 1 μs. The primary difference

between high and low repetition rate systems appears at this stage. The time interval between subsequent pulses is 1 ms in a 1 kHz laser system, while it is 0.1 μs in a, for example, 10 MHz laser system. So, by using a kHz laser system, there will exist a temperature rise and drop after all subsequent pulses. On the other hand, by using a HRR laser system with appropriate pulse energy, pulse shape, scan speed and so on, heat will be accumulated over a focal region by subsequent pulse trains and temperature can be kept almost constant with very low range of fluctuation while focal area moves smoothly to next regions. Although HRR laser systems enable an easier accumulation of heat over a focal region with low temperature fluctuations, to our knowledge, fabrication of Type-II or Type-III WGs by using HRR laser systems have not been studied or reported yet. Of equal importance, using a HRR laser system increases the possible range of translation speeds to find better inscription regimes during experimental optimisation process. In Table 3.1, NP gives the number of pulses when focal spot is translated 1 μm, calculated by RR/TS. Interestingly, it ranges from 2 to 250 for a wide variety of inscription settings. For example, for an inscription setting [44] by using 2 pulse during 1 μm translation of focal spot, the translation speed is 0.5 mm/s. If translation speed is increased to 1 mm/s, only one pulse can be focused per a length of 1 μm region, which means that the optimisation range for possible translation speeds is drastically reduced. What is more important is that faster translation speeds can be employed during fabrication by using HRR laser systems. Translation speeds for various inscription regimes by using low and high repetition laser systems can compared in Table 3.1. For example, the best loss results had been reported by using a 46 mm/s translation speed [119], which is approximately 50 times faster compared to 0.9 mm/s translation speed in [34] reported by the same author, or which is 460 times faster than an average 0.1 mm/s translation speed of low repetition rate inscription regimes. Surely, those translation times of HRR incription

regimes may even increase or decrease, depending on the repetition rate of the laser systems and other optimisation parameters, thereby providing a bigger optimisation interval. This is very important because next generation IOCs especially in optical communication or optical computing systems will demand the fabrication of highly complex optical systems consisting of thousands of optical devices. As direct fs laser inscription method enables the fabrication of highly complex 3D IOCs in a small foot-print, the use of HRR laser systems seems to be a key factor for mass production of future all-optical communication and computing devices by decreasing fabrication durations and corresponding production costs.

3.2 Experimental setup and procedures

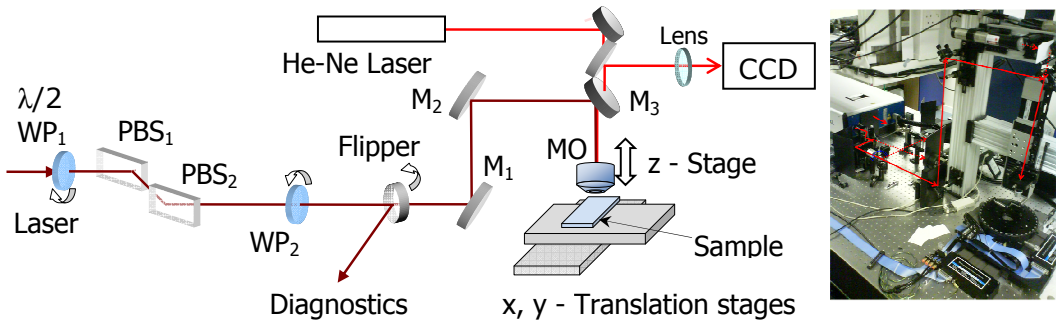

Figure 3.1: Experimental setup. WP: wave plate, PBS: polarisation beam splitter, M: folding mirror, MO: micro-objective, CCD: charge-couple device.

The experimental setup used for HRR fs laser inscription of $LiNbO_3$ is shown in Fig. 3.1. The fs laser is a commercial chirped-pulse oscillator (CPO) system [129] (Femtosource Scientific XL, Femtolasers), which consists of a diode-pumped solid state Verdi V-10 (10 W, green, 532 nm laser), a 3 mm length of highly doped Ti:Sapphire crystal, a broad-band (BB) and chirped intracavity mirrors, and a saturable Bragg reflector (SBR) end mirror. It operates at the central wavelength of 792 nm with a repetition rate around 11 MHz. A

frequency-resolved optical gating device (Grenouille) is used to measure temporal pulse widths. Dispersion compensation is implemented by use of chirped BB and SBR mirrors. Pulses have a radially symmetric beam profile and the shortest full-widths at half maximum of temporal pulses are around 50 and 26 fs when SBR is used or not, respectively [25, 112]. Spectral bandwidth is approximately 30 nm in the case of SBR inclusion. Laser system produces on-target pulse energies of maximum 75 nJ. The same system produces two times shorter pulse duration with approximately more than twice the energy output without SBR. Starting of fs laser system is achieved by first operating in total negative dispersion regime and shifting to total positive dispersion by adjusting the mirror at the end of the cavity.

CPO system generates linearly polarised laser pulses. The first half-wave plate and two Brewster angle polariser are employed to control the intensity of the laser beam. Second wave plate in Fig. 3.1 is used to adjust the polarisation state. The following steering mirrors carry laser beam to the MO, as well as to auxiliary diagnostic equipments: a FROG, a spectrometer, a power meter and a beam shifter. Broadband, highly reflective and polarisation-insensitive dielectric mirrors with a low group-velocity dispersion (GVD) around 20 fs^2 and a high reflectivity of 99% are chosen. He-Ne laser beam and a CCD camera are employed to observe and to adjust the alignment of light beam as perpendicular to the surface of transparent material. Spatial beam profiles after CPO and before MO are checked by a beam profiler to be circular or slightly elliptical by small laser cavity adjustments.

During the inscription of $LiNbO_3$ crystal, a Zeiss MO with 1.25 NA is used after trying a number of MO lenses to observe the possibility of writing smooth, non-damaged tracks. It has a fixed spherical aberration correction at the depth of 0.17 mm in standart glass and it is immersed in oil, the RI of which is $n = 1.523$. Any dispersion which can be induced by the MO glass or any other optical element is compensated by a slight tuning of the prism

compensator at the CPO output by observing the minimum threshold level for a continuum of light [25]. Polarisation state of laser beam is adjusted as linear and perpendicular to the sample scanning direction based on the reports regarding the fs laser inscription in various glasses [20, 98] and crystals [25, 98], which state that the optimum HRR fs laser inscription regimes are independent of the polarisation state of laser beam. Polarisation state of laser beam irradiated on $LiNbO_3$ can be adjusted by the second wave plate which is next to Brewster angle polarisers.

A z-cut $LiNbO_3$ wafer of 75 mm diameter and 1 mm thickness (supplied by University Wafer) is used to obtain the results presented in the following section. A 3D Aerotech translation stage, which consists of the air-bearing 2D stages (ABL10050) for the x and y directions and an independent mechanical roll-bearing type stage (ABS-100) for the z direction, are used to translate the positions of samples at speeds up to 100 mm/s with sub-micrometer accuracy and are controlled by computer through the NPAQ controller (Aerotech). Sample is mounted on a rotary and homemade platform (Ekspla, Lithuania) with heavy load carrying capacity. Accurate positioning of the top surface of the sample is checked to be transverse to the x-y plane and perpendicular to laser beam direction by adjusting precision screws and by observing the reflection from the sample top surface. The first wave plate in Fig. 3.1 is controlled by computer to adjust the intensity of light reaching over the sample. A transverse inscription direction is used such that laser beam is transmitted along the z direction. Inscription of a WG with multiple number of tracks start from the deepest track along the z direction. Inscription of any track is started by turning on a computer-controlled-electronic-shutter, and sample is moved transversely in the x-y plane. After the inscription of a track has been completed on any x-y point; the shutter is turned off, sample is moved back to the starting point of the next deepest track to be written on the x-y plane, the depth of

focal point of the next track is adjusted by changing the position of the MO on z direction, and shutter is turned on for the inscription of the next track.

Experimental settings which are used to focus fs laser beams inside the sample take extra importance with respect to the distribution of spatial and temporal intensity around the focal volume and to the accurate positioning of focal point beneath the sample top surface. If fs laser beams can not be focused well enough, energy of laser beam is distributed over a bigger area and, consequently, intensity or energy threshold of material can not be reached. The better the focusing of the fs laser beam, the lower the pulse energy to produce a continuum of light within $LiNbO_3$ [112, 115]. For example, energy threshold is measured to be approximately 12 nJ at an inscription depth of 0.5 mm in borosilicate (BK7) glass using an oil-immersed MO with an effective NA of 1.2 [130]. On the other hand, the energy threshold of $LiNbO_3$ is measured to be three times higher at inscription depths of approximately 0.25 mm by using a commercial MO with a NA of 1.25 [45]. The threshold for residual material modification is respectively higher than the threshold for the appearance of a continuum in $LiNbO_3$ as well as in other crystals [25]. It is also worth emphasizing that the difficulty of focusing of high intensity laser beams in $LiNbO_3$ crystals [131] puts extra importance over the choice of MOs due to the RI difference between E and O axis. Aberration-free focusing at arbitrary depths in such crystals may become possible by using special focusing equipments rather than standart MOs. The results presented in the next section can be improved by using computer-controlled spatial phase modulators [131] and an on-line feedback loop mechanism. However, unavailability of methods to determine optimum focusing conditions puts limitations on its implementation for birefringent crystals.

Fs laser inscribed tracks are visually inspected by using an optical microscope, Axioscope-2 MOT (Zeiss), which is equipped for both transmitted light and differential interference

contrast (DIC) measurements. A charge-couple device (CCD), 10 megapixel and 16 bits camera, on the microscope is interfaced to a computer by a fibre-optic link to reduce the level of electronic noise and to achieve high data throughput. Cumulative phase profile and RI distribution of tracks are estimated by using Quantitative Phase Microscopy (QPM) method by using a commercial software (IATIA). The QPM technique is based on taking bright field images at different focus distances (an in-focus image and a number of slightly positive and negative defocused images) and calculating the differential of these data for phase recovery [132, 133]. This technique requires an accurate positioning along the z axis for the extraction of correct phase information. Since the motorised version of microscope has a built-in, electronically controlled z translation stage with an approximate positioning accuracy of 100 nm, choosing a z step size which is equal to an integer multiple of the motor stepper size let avoid any interpolation due to the motion controller and achieve a positioning accuracy up to an (estimated) value of 20 nm. Further improvements are possible by using a position feedback encoder or by reducing any noise arising during the image acquisition and transmission. Also, any additional noise due to short exposure times can be minimised by choosing large exposure times over a fraction of a second. Extra care is required during the application of QPM technique for objects with absorption or gain because of the fact that this method is based on the transport-of-intensity equation [133, 134], which is valid only when the beam energy is preserved. A comparison between QPM measurements of BK7 glasses and those by scattering interferometry clearly disclose this problem [130].

The radial RI profiles of the tracks can be extracted from the cumulative phase data obtained from QPM by using Abel inverse transform method [135], which is based on the assumption that the structure is axisymmetric. Phase retardation maps and corresponding RI values can be obtained by using QPM and Abel transform over $300\,\mu\text{m} \times 400\,\mu\text{m}$ view area of

microscope for an image magnification factor of 20. It is worth emphasizing that the phase retardation maps obtained by QPM software for z-cut $LiNbO_3$ samples are not sensitive to the polarisation of the illumination light, so necessitating extra care to interpret the phase maps on wafers with different orientations due to the host birefringence.

3.3 Results

The results [45] presented below is a result of an investigation in search of the optimal conditions over the parameters space: fs laser pulse energy, the speed of translation stage, focus depth inside the $LiNbO_3$ sample, polarisation state of the laser beam relative to the scanning direction, and the duration of laser pulses. The results are obtained by using laser pulses with a minimum pulse duration, polarised in the x direction perpendicular to the scanning direction. Additionally, beam profile, calculated by $1 - b/a$ where a and b are the respective major and minor semi-axes, exhibits a small ellipticity of 0.05 with the larger semi-axis in the scan (y) direction [25, 45]. The physical characteristics of tracks inscribed by using different inscription parameters except those showing any apparent instabilities are evaluated by employing a white-light microscope and the QPM technique based on the Abel transform. An example of tracks obtained with a high inscription energy is shown in Fig. 3.2. Those tracks shown are written by using an inscription energy of 58 nJ. Two pairs of tracks on the left and right side are written at a scanning speed of 40 mm/s and 60 mm/s, respectively, and tracks of each pair are scanned at opposite direction with respect to other track. A typical example of the reconstructed RI profile of a track written at the inscription energy of 58 nJ and at the scan velocity of 12 mm/s is shown in Fig. 3.2(b). As it can be seen, highly uniform tracks are obtained even at high inscription speeds in z-cut $LiNbO_3$ crystal,

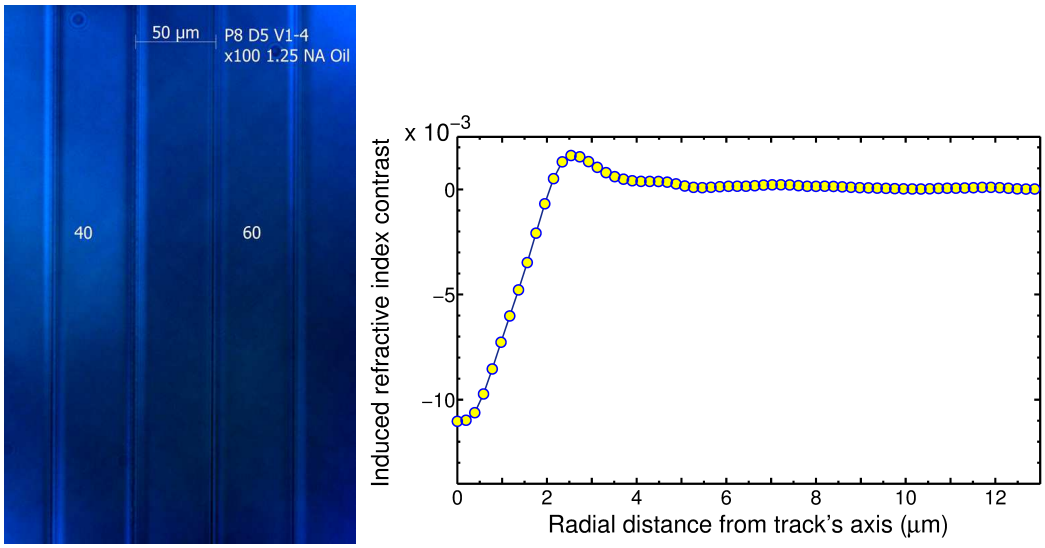

(a) (b)

Figure 3.2: (a) DIC microscope views of two pairs of tracks [45] (Inscription energy is 58 nJ, scanning speeds are 40 mm/s (left pair) and 60 mm/s (right pair), inscription depth is $\approx 200\,\mu$m) (b) Radial RI profile of a track [45] (Inscription energy is 58 nJ, scan velocity is 12 mm/s and inscription depth is $\approx 200\,\mu$m).

and any significant morphological change on tracks due to different scanning directions do not exist. RIs of those tracks have a negative contrast and it do not permit guiding of light.

Keeping other inscription parameters constant and changing just the inscription energy from 35 to 60 nJ, the variation of radial size (r) and peak RI contrast of tracks are shown in Fig. 3.3 (scanning velocity is 12 mm/s, approximate depth from the surface of the crystal is 250 μm). It is obvious that both sizes of tracks and the magnitude of the peak RI contrast increase with pulse energy. A maximum index change of -0.0127, which is the highest RI contrast achieved in $LiNbO_3$ by fs laser inscription, is seen at the inscription energy of 58 nJ. However, it is worth reminding that those values are obtained by varying just pulse energy and by keeping other experimental parameters constant during fs laser inscription in $LiNbO_3$, which means that track radius and RI contrast, without any interdependence, still have the possibility of being tuned to any desired value in a certain range by some

exploration in the parameter space of fs laser inscription. For example, uniform tracks can be achieved within a wide range of scanning velocities from a few mm/s to 60 mm/s, though the uniformity of the immersion layer underneath the MO may pose problems when the inscription of tracks are performed by using high pulse energies and fast scanning. Fabrication of MS WGs with any desired geometry necessitates the inscription of tracks

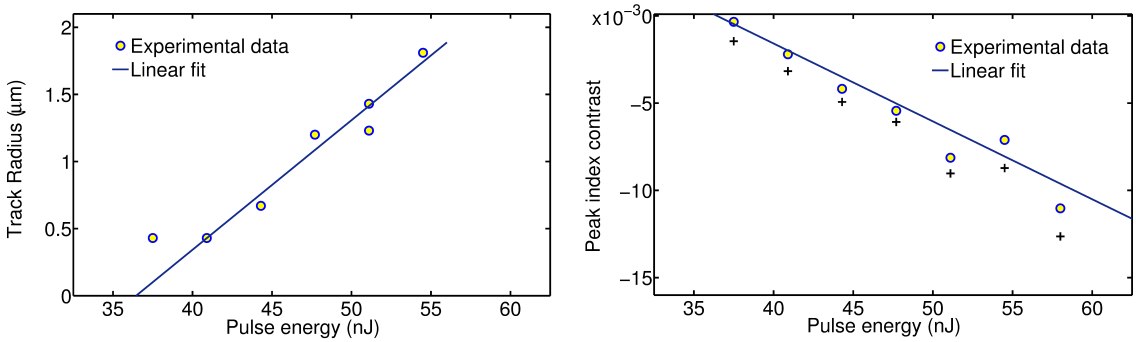

(a) (b)

Figure 3.3: (a) Radius and (b) peak RI contrast of the tracks as a function of inscription energy [45] (Scanning velocity is 12 mm/s and approximate inscription depth is 250 μm).

at different depths under the sample top surface, and relative positions of tracks need to be controlled with high precision. Most important parameters which can effectively determine the depth of tracks are both the distance of the MO from sample surface and its NA. Any straightforward approach to relate the actual focusing depth of the inscription beam with MO shift of the z-axis stage do not exist due to a multitude of nonlinear effects during the wave front propagation. However, once any inscription regime is determined, the use of advanced optical devices such as spatial light modulators, which can reconstruct the formation of similar wavefronts at any inscription depth, makes it possible to obtain similar track sizes and RI contrasts. Microscope images of a MS WG written in a z-cut $LiNbO_3$ sample are shown in Fig. 3.4. All tracks are written by using fs laser pulses with an energy of 48 nJ, transverse scanning velocity of 15 mm/s, and at an approximate depth of 250 μm. The

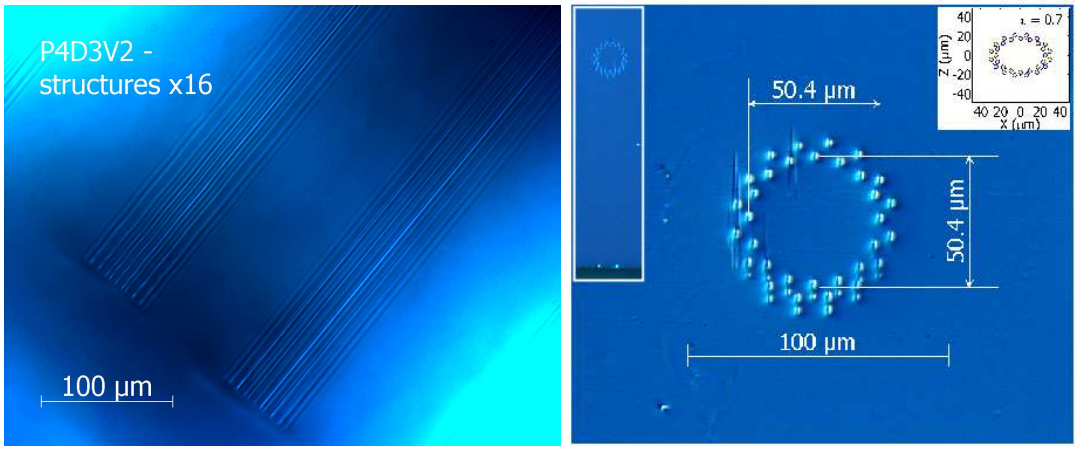

a) b)

Figure 3.4: Microscope (a) overhead view, and (b) cross section view of a fabricated MS WG with two rings of tracks [45] (Inscription energy is 48 nJ, scan velocity is 15 mm/s, and inscription depth is $\approx 250\,\mu$m).

depressed cladding consists of two circular rings, each of which have equally distributed sixteen tracks. The radii of inner and outer circles are 24 μm and 30 μm, and average sizes of tracks are 3.7 and 1.4 μm for its major and minor axis, respectively. Guiding properties of this MS WG are investigated by using a broadband light source with a total bandwidth from 0.4 to 2 μm. It is filtered by using an external acousto-optic tunable filter which have six separate channels with an approximate bandwidth of 20 nm. The filtered light is coupled into the MS WG through a multi-mode optical fiber with a core diameter of 40 μm. Total propagation losses are estimated through integration of mode field profiles on the CCD camera. Calculated propagation loss is approximately 3 dB/cm around 0.6 μm of wavelength , and it is approximately ten times bigger around 1 μm of wavelength. Those loss results obtained from this MS WG with just two rings of tracks are a clear indication of a necessity that structural properties of MS WGs should be designed to lower confinement losses and evaluated for any possibility to control the propagation properties. Taking into account the relatively moderate levels of track RI contrasts, which are possible to achieve by

current fs inscription technology, lower confinement losses may become possible by using higher number of tracks and by employing some design strategies. Micro-fabrication of such large number of tracks make HRR fs laser inscription the preferred technique over that of kHz fs laser inscription or other fabrication methods. The reason for this fact can be more clear by calculating the fabrication time of a MS WG at the length of 10 cm and with total number of 200 tracks over the cladding region. It may exceed 60 hours if a kHz fs system (with a typical translation speed of 10 to 500 μm/s [25]) is used, whereas it is less than an hour if a HRR system is used. More importantly, it is worth reminding that HRR fs laser inscription technology can be extended for the micro-fabrication of periodically poled crystals to enable a wide spectrum of applications in classical and quantum optics.

3.4 Summary

In conclusion, this chapter first introduces direct fs laser inscription method and gives a review of experimental settings previously used by other researchers and obtained results regarding to WG properties fabricated in $LiNbO_3$. Then, experimental setup used during WG fabrication in $LiNbO_3$ is introduced, and results with regard to experimentally achieved track parameters [45] are provided. It is shown that the RI contrasts of individual tracks fabricated in $LiNbO_3$ can be at a record-high value of -0.0127, and that RI contrasts and sizes of individual tracks can be varied by the applied pulse energy.

Chapter 4

Design of depressed-cladding micro-structured waveguides in $LiNbO_3$

4.1 Introduction

As mentioned in Chapter 1, the combination of excellent electro-optical, acousto-optical and nonlinear optical (χ^2) properties, as well as its wide transparency window, make $LiNbO_3$ an attractive material to integrate various linear and nonlinear optical applications in IOC devices [6, 7, 136]. After the advent of quasi-phase matching by poling of ferroelectric crystals [137], $LiNbO_3$ has become one of the most commonly used materials in devices such as acousto-optical filters, frequency converters and optical parametric generators.

MS WGs with low losses, high damage threshold and controllable dispersion in a broad spectral range are highly demanded for both traditional applications and applications in recently emerged fields, such as integrated quantum optics and mid-IR range frequency comb generation. In this chapter, we numerically study the design of depressed-index cladding

MS WGs with an hexagonal geometry, which can be formed in a z-cut $LiNbO_3$ crystal by fs laser writing [138]. Depressed-cladding MS WGs have been demonstrated to achieve light propagation with good mode confinement and low propagation losses at various wavelengths of light in comparison to directly written, single-track WGs [37, 43, 117, 139, 140]. The simplest type of depressed-index cladding consists of only two parallel tracks positioned close to each other [97, 125]. But such a WG structure does not allow for control over the wave-guiding properties. On the other hand, owing to geometric flexibility in track positioning, the depressed cladding may consist of a fairly large number of arbitrarily arranged tracks confining the flexibly large and shaped core guiding area [43]. Our goal is here to establish how experimentally accessible parameters, such as the size, RI contrast, number and positions of tracks in the depressed cladding region, can be used to achieve control over the propagation constants of modes with different polarisations in the WG geometry [138]. A similar approach has already been used for controlling the wave-guiding properties of MS optical fibres (MOFs) [141–143], where tracks/rods with a reduced RI are naturally formed by introducing air holes during the fibre drawing process.

4.2 Waveguide packing geometry and methodology

For this study, we modeled depressed-cladding WG structures with an hexagonal geometry. This is a fairly commonly used WG shape, which has already been well studied in the case of isotropic materials such as MOFs [143]. The depressed cladding was formed by a finite number of rings of regularly spaced, cylindrical tracks whose centers were arranged hexagonally, as shown in Fig. 4.1. These tracks can be written in a $LiNbO_3$ crystal by direct fs laser irradiation using a transverse inscription geometry (cf. chapter 3) [97]. In our

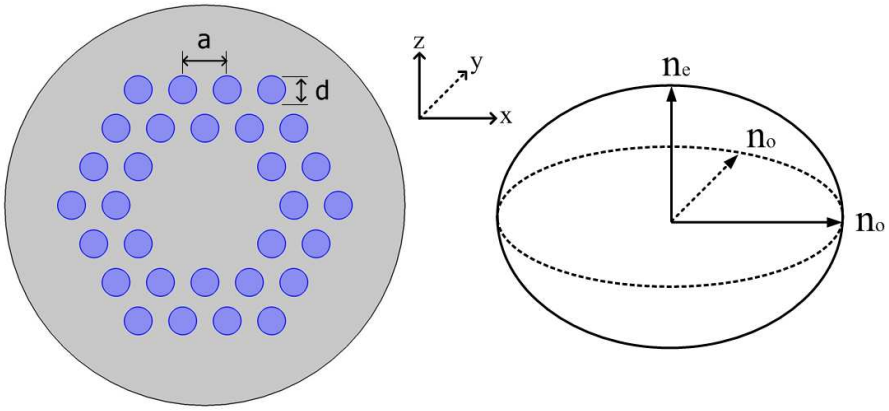

Figure 4.1: Cross section of modeled depressed-cladding WG with two rings of tracks, and ellipsoid of indices for $LiNbO_3$ host.

modeling, the reduced RI of the tracks was assumed to be a real value, uniform across the cross section of a track, and polarisation- and wavelength-independent. Note that this might not be the case in practical scenarios, especially under arbitrary fs laser irradiation protocols. Indeed, direct measurements of the ultrafast dynamics of the dielectric permittivity of glass materials [130] revealed that irradiation by HRR fs laser can generate changes in both real and imaginary parts of the permittivity, especially for long irradiation times or high laser pulse energies. Importantly, fs-written tracks in crystals possess a complex geometry and include volumes of material with increased and decreased RIs [37]. However, the change of RI, averaged across the cross section of each track, has always negative sign.

Key parameters that were varied in the numerical model were extracted from experiments (cf. Chapter 3). They include the track size d, the track spacing or pitch a, the RI contrast between the cladding and core regions δn, and the number of track rings or depressed-cladding layers N_r. On the other hand, in this work we did not explore other symmetries, more complex topologies or tiling, and disorder. Some of such examples can be found in [144].

In this study we considered a z-cut $LiNbO_3$ wafer with the larger surfaces perpendicular to the z axis of the coordinate system (Fig. 4.1). The z axis is the optical axis of the crystal, and light is assumed to propagate along the y axis. Following [145], a three-oscillator Sellmeier equation of the form:

$$n^2 = 1 + \frac{A\lambda^2}{(\lambda^2 - B)} + \frac{C\lambda^2}{(\lambda^2 - D)} + \frac{E\lambda^2}{(\lambda^2 - F)} \tag{4.1}$$

was used for the RIs of congruently grown $LiNbO_3$ doped with 5 mol.% magnesium oxide (MgO), with the following Sellmeier coefficients:

Coefficient	n_e	n_o
A	2.4272	2.2454
B	0.01478	0.01242
C	1.4617	1.3005
D	0.05612	0.05313
E	9.6536	6.8972
F	371.216	331.33

Table 4.1: Sellmeier coefficients for 5 mol.% MgO doped $LiNbO_3$

As mentioned in Chapter 2, the wave equation for electric field vector (Eq. (2.4) with (2.11) and (2.14) were solved using the COMSOL software based on the FEM to find out the complex effective RIs $n_{o,e}^{\text{eff}}$ of the modes of the structure for the two orthogonal polarisation states x and z, hence the WG dispersion and confinement losses. In our numerical simulations, the wavelength was varied in the transparency window of 5% MgO-doped $LiNbO_3$, from 0.3 μm to 3 μm. As mentioned in Chapter 2, the FEM results presented in this thesis refer to the fundamental mode of the structure, which was selected using the criterium of minimum effective mode area during the wavelength scanning.

4.3 Mesh and PML setting

Special care was given to the choice of the computational mesh and the parameters of the PML. As mentioned in Chapter 2, the mesh size must be a few times smaller than the wavelength being used to ensure good accuracy of the results. In our simulations, the computational domain was mapped with an automatically configured, triangle mesh with the minimum size 0.003 μm in the core of the domain and the relative growth rate 1.1. The maximum mesh size at the periphery of the domain is of the same order of magnitude as the shortest wavelength in use. The same mesh is used for all wavelengths in the range being studied.

The PML was configured according to Eq. (2.31). As mentioned in Chapter 2, the PML must have sufficiently large κ_{max} to provide an adequate level of absorption and be wide enough to guarantee a small absorption gradient across its extent. We performed a number of testing runs for a hexagonal MS WG with two rings of tracks, with the diameter $d = 1.6$ μm and the pitch $a = 2$ μm. The induced RI contrast was $\delta n = -0.05$. Parameters L and κ_{max} were varied between 10 μm and 50 μm, and between 0.03 and 0.2, respectively. The evaluation range of κ_{max} was determined by a prior testing such that κ was considered as a constant value all over the PML region, and the value of κ at which transition reflection became significant was found. In Fig. 4.2 we show the confinement loss $\mathcal{L}$ for the O wave as a function of the PML thickness L for different values of κ_{max} at different wavelengths. A common feature of the results obtained is that transition and round-trip reflections are dominant when L is small, whereas they become increasingly less important with increasingly larger PML thickness. The confinement losses at all wavelengths being studied converge to a constant value when the PML is wide enough and κ_{max} is 0.05. Considering that mesh sizes

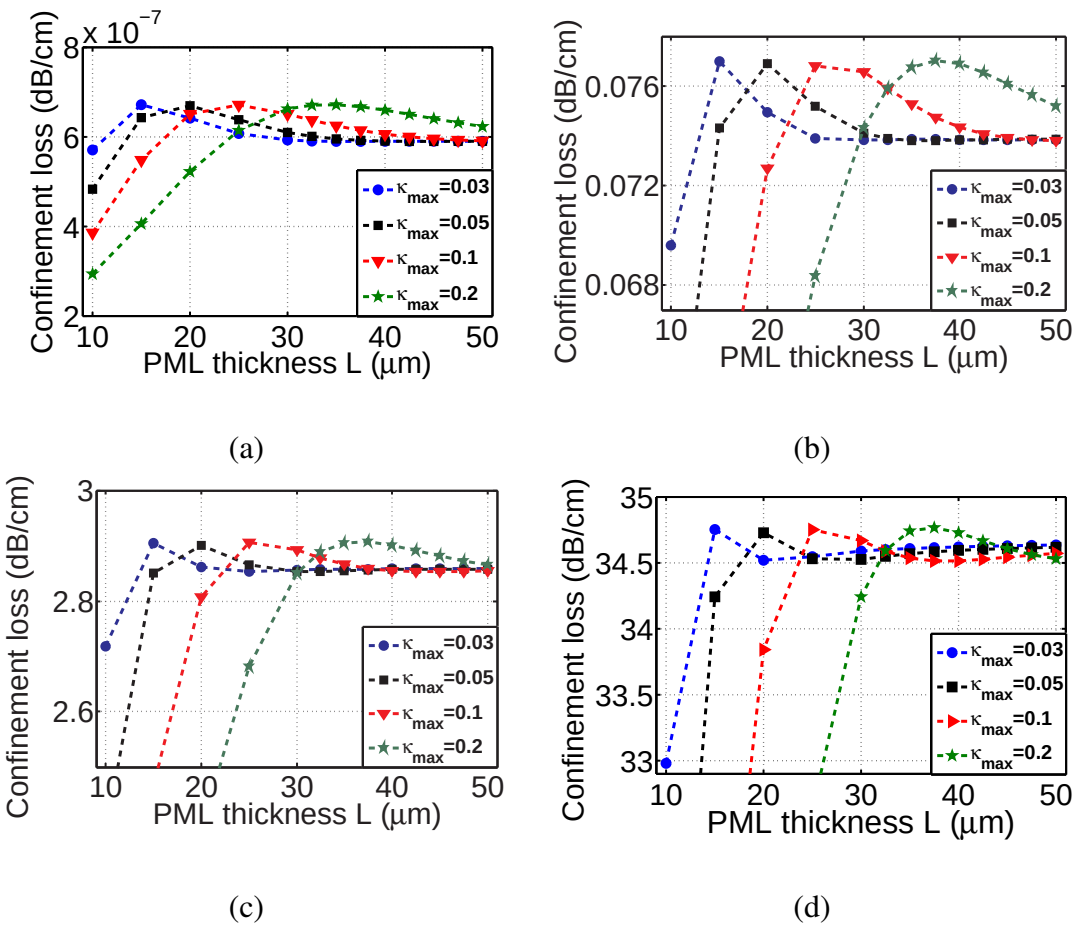

Figure 4.2: Confinement loss for O wave as a function of PML thickness for different values of the PML maximum absorption for a depressed-cladding WG with two rings of tracks ($N_r = 2$) at various wavelengths: (a) $\lambda = 0.5$ μm, (b) $\lambda = 1$ μm, (c) $\lambda = 1.3$ μm, and (d) $\lambda = 1.6$ μm. WG parameters are: $d = 1.6$ μm, $a = 2$ μm, $\delta n = -0.05$.

are small enough to correctly represent all the wavelengths being used, we can conclude from Fig. 4.2 that, if the PML is chosen to be sufficiently wide, κ_{max} can be assumed to be wavelength-independent. So, in the simulations described hereafter we set $L = 40$ μm and $\kappa_{max} = 0.05$.

4.4 Results and discussion

One of the important features of MS WGs is the control that their geometry and structural parameters can exert on the dispersion and loss characteristics of modes. The confinement

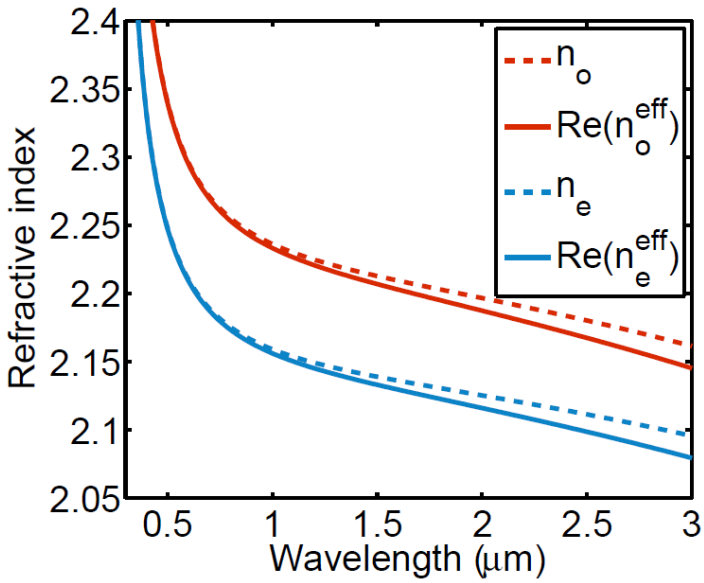

Figure 4.3: Real parts of effective RIs for O and E waves as a function of wavelength for a depressed-cladding WG with two rings of tracks, $N_r = 2$. The O and E RIs of the unmodified material are also shown. WG parameters are: $d = 1.6\ \mu$m, $a = 2\ \mu$m, $\delta n = -0.05$.

losses that are intrinsically related to the WG geometry, in particular, are the most important parameter to consider in any practical design of WGs. In Fig.4.3 we show a typical evolution of the real parts of the effective RIs for the O and E waves with wavelength, for a depressed-cladding WG with two rings of tracks. In this example, we modeled tracks with the diameter $d = 1.6\ \mu$m and the pitch $a = 2\ \mu$m. Direct fs laser inscription experiments in 5% MgO-doped $LiNbO_3$, as described in Chapter 3, have revealed that the track diameters may vary in the range from 1 to approximately 3.5 μm. In the example of Fig. 4.3, the pitch was set to the minimum value ensuring no overlap of the tracks for the chosen track size. The induced RI contrast was $\delta n = -0.05$. This value is above the RI contrasts of the tracks of depressed-cladding WGs that can be achieved in 5% MgO-doped $LiNbO_3$ with current fs micro-fabrication technology - typical values are around -0.01. However, since there is some experimental evidence that larger RI contrasts can in fact be obtained, in a number of simulations we exceeded the value -0.01 to demonstrate the effect of higher RI contrasts on

the waveguiding properties. It is seen from Fig. 4.3 that the deviation of the RIs $n_{o,e}^{\text{eff}}$ curves from the corresponding curves in the unmodified material $n_{o,e}$ becomes larger for longer wavelengths. This is an indication that with only two rings of tracks, the WG structure can not confine the modes well at long wavelengths.

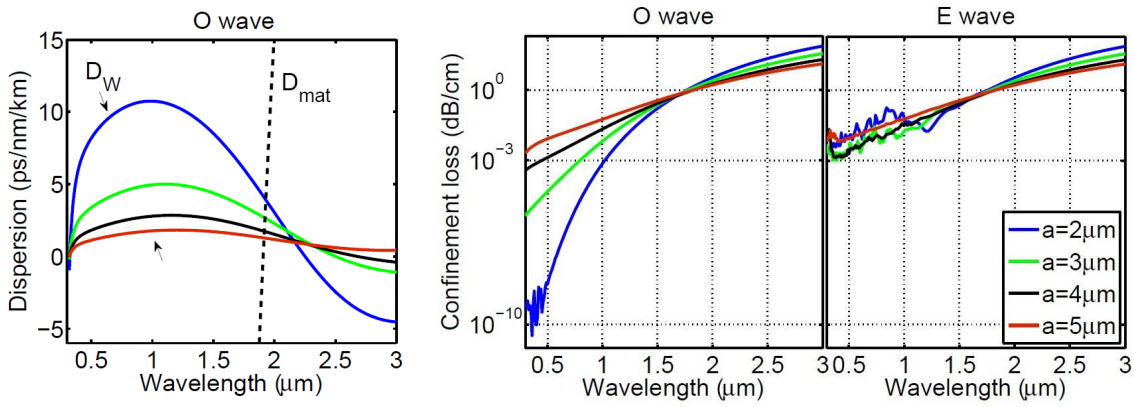

(a) (b)

Figure 4.4: (a) WG dispersion D_W for O wave, and (b) confinement losses for O and E waves as a function of wavelength for a depressed-cladding WG with two rings of tracks with various pitches. The material dispersion D_{mat} is also shown. Other WG parameters are: $d = 1.6\ \mu$m, $\delta n = -0.05$.

In Fig. 4.4 we show the variation of the key WG quantities: WG dispersion D_W and confinement loss $\mathcal{L}$, as a function of both wavelength and track spacing for a WG with two rings of tracks. The pitch a was varied from 2 to 7 μm, whereas other WG parameters were kept the same as in Fig. 4.3. A noticeable trend in the dispersion curves is that the dispersion changes introduced by the WG are more pronounced for smaller a. These changes, however, are not big enough to affect the total dispersion of the structure significantly. Note that at the shorter wavelengths, the depressed cladding can effectively confine the modes in the core guiding region. Guidance becomes worse at longer wavelengths, hence the modes behave like 'leaky modes'. Because of such a leakage at longer wavelengths, none of the resonance features which would be expected due to the periodicity of the structure can be observed.

Moreover, band-gap resonances could be observed for this structure at wavelengths three or four times larger than the pitch, which fall outside the wavelength range used in our study. Our simulations also show that the change of the pitch in itself does not extend the spectral range where the loss figures for the modes are acceptably low. We assume hereafter 1 dB/cm to be an acceptable loss level for practical applications. The influence of the RI contrast of tracks on the WG dispersive and loss properties is illustrated in Fig.4.5. There δn was varied from -0.02 to -0.05. It is clear that larger RI contrasts expand the wavelength region where the values of geometric loss are acceptably low, even with only two rings of tracks. The wavelength region where the WG contribution to the total dispersion is not negligible becomes also wider though the dispersion changes due to the WG remain small.

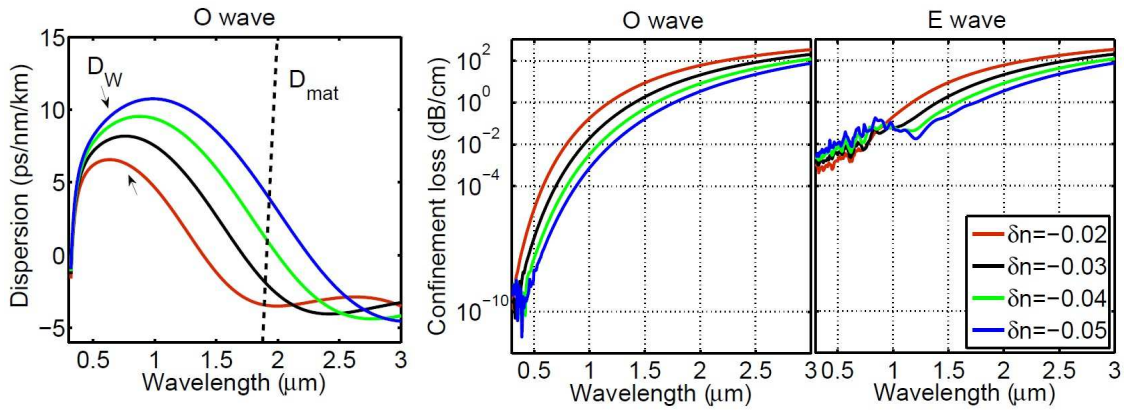

(a) (b)

Figure 4.5: (a) WG dispersion D_W for O wave, and (b) confinement losses for O and E waves as a function of wavelength for a depressed-cladding WG with two rings of tracks of various RI contrasts. The material dispersion D_{mat} is also shown. Other WG parameters are: d = 1.6 μm, a = 2 μm.

A general fact that emerged from our study is that control over the waveguiding properties is better for compact cladding structures with small-sized and densely packed tracks with the largest possible RI contrasts. Fig.4.6 highlights the more interesting scenario that can be achieved with a varying number of cladding layers. The RI contrast was set to $\delta n =$

-0.01 in these simulations. As can be seen from Fig.4.6, while the dispersion changes due to the WG become increasingly more pronounced with increasing N_r, the overall effect of adding rings 3-7 on the dispersion properties of the structure is little. On the other hand, importantly, adding further rings of tracks can reach much better control over the losses even at the relatively moderate RI contrasts that are currently technologically feasible. As Fig.4.6 shows, adding rings (3-7) results in an extension of the spectral range where the confinement losses in both O and E polarisations are below 1 dB/cm to the wavelengths near 2 μm, and in a reduction of the losses in both polarisations by more than three orders of magnitude near the telecommunication wavelength $\lambda = 1.55$ μm. This is an important result for any practical applications of such WG structures. We would like to note, however, that the figures reported here include only confinement losses showing the limitations that are due to the confinement by a MS WG. In practice the total losses of the modes propagating in the structure will always be higher because of various factors, including: material absorption induced by fs irradiation, scattering losses due to irregularities (non-smoothness) of the cladding tracks, and imperfect positioning of the tracks which would increase the leakage of modes out of the guiding region.

As it was shown in Ref. [143] in the case of MOFs, a natural strategy to achieve low losses with fewer tracks or, equally, to extend the spectral range of low-loss operation of the WG structure, is to allow the track diameter to differ from one ring to another with the exterior rings that have large tracks. This design concept is illustrated in Fig. 4.7, which shows the variation of the confinement losses in the O and E polarisations with wavelength for a seven-ring structure with different track diameters. The track diameter of the innermost ring was arbitrarily set to $d_1 = 1$ μm, and the diameter of subsequent rings was increased linearly up to the maximum value $d_7 = 2.2$ μm for the outermost ring. Such a variation of

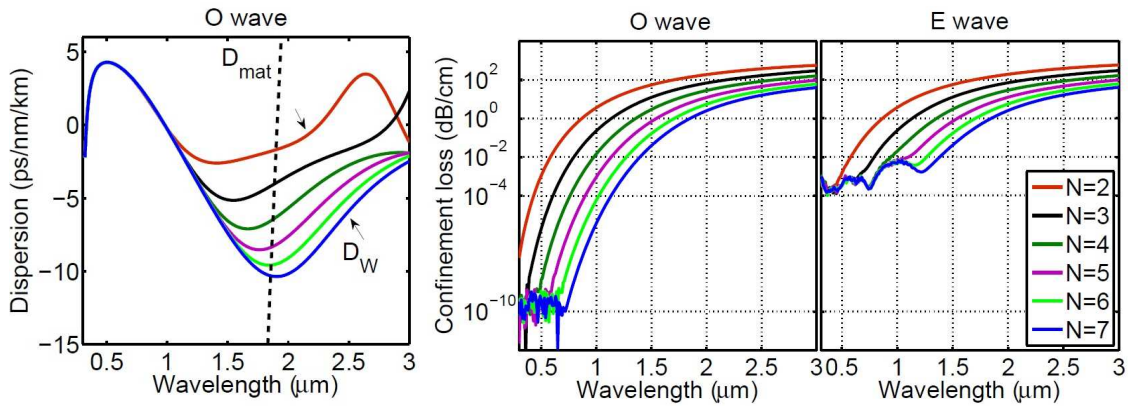

(a) (b)

Figure 4.6: (a) WG dispersion D_W for O wave, and (b) confinement losses for O and E waves as a function of wavelength for a depressed-cladding WG with varying number of track rings. The material dispersion D_{mat} is also shown. Other WG parameters are: $d = 1.6\,\mu$m, $a = 2\,\mu$m, $\delta n = -0.01$.

the track size can be easily realised in practice by changing the energy of the irradiating fs laser pulses from one ring to another. Note, however, that this would entail a slight change in the induced RI contrast since also the latter depends on the pulse energy (cf. Chapter 3). The pitch was $a = 2.5\,\mu$m, and the RI contrast was $\delta n = -0.01$ in these simulations. One can see from Fig. 4.7 that, compared to the usual WG structure made of tracks of identical diameter (Fig.4.6), this WG design allows us to expand the diapason of low-loss operation for both O and E polarisations into the mid-IR spectral region. As we will see in Chapter 5, optimisation of these WG geometries may enable further expansion of their low-loss operational spectral range.

An important issue that should be addressed here relates to the practical feasibility of the investigated WG structures. As mentioned in Chapter 3, there are experimental limitations on the magnitude of the RI contrasts that can be reached for smooth tracks in crystals. Thus, to provide WG structures that display low-loss operation over a wide spectral range, the most viable solution is to write a fairly large number of rings of tracks, possibly with different

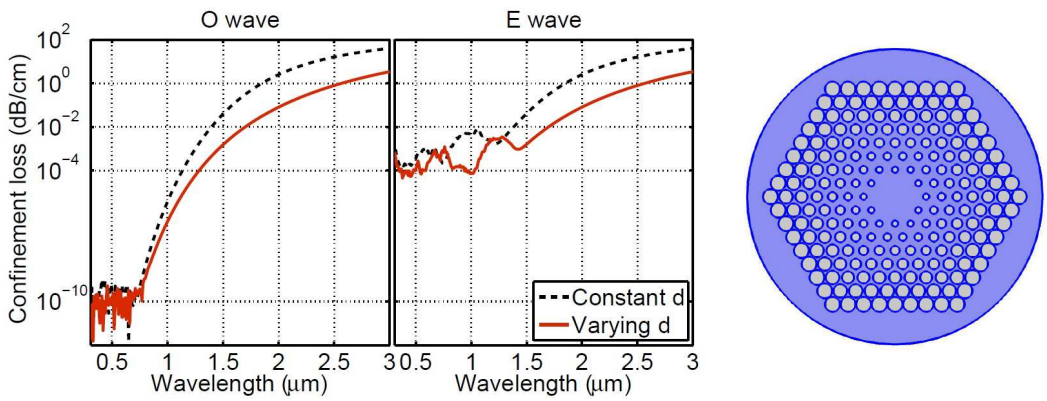

(a) (b)

Figure 4.7: (a) confinement losses for O and E waves as a function of wavelength for depressed-cladding WG with seven rings of tracks, $N_r = 7$, with different diameters $d = 1.2 - 2\ \mu$m. Other WG parameters are: $a = 2.5\ \mu$m, $\delta n = -0.01$. The losses for seven rings of identical diameter are also shown (extracted from Fig. 4.6). (b) cross section of modeled WG structure.

sizes. These requirements on the number of rings make HRR fs laser inscription the preferred micro-fabrication technique, as high-repetition-rate fs systems can enable up to four orders of magnitude quicker fabrication than the low-repetition-rate ones [20]. For example, for a propagation length of 10 centimeters in a WG with seven rings (around 200 tracks) the total length of the inscribed lines would amount to approximately 20 meters. Clearly, if one uses a kHz fs system (with a typical sample translation speed of 10 to 100 mm/s), the fabrication time required on a single structure may exceed 60 hours, whereas a high-repetition-rate system can do the job in less than an hour.

4.5 Conclusion

We have shown numerically the feasibility of controlling the guiding properties of depressed-index cladding WGs that can be formed in a LiNbO$_3$ crystal by fs laser writing, by exploiting the WG geometric and structural characteristics. Our study ranged over the parameter space:

track size, spacing, number of rings, and RI contrast, that is accessible experimentally. As shown, the relatively moderate RI contrasts that are feasible by use of current fs micro-fabrication technology mean that geometric WG parameters have little control over the chromatic dispersion properties of the WG. On the other hand, the number of track rings revealed to play a major role in the control of the geometric losses. Importantly for technological applications, it is shown that for the typical induced RI contrast -0.01, increasing the number of rings from two to seven results in an extension of the spectral range where the confinement losses in both O and E polarisations are acceptably low (below 1 dB/cm) to the wavelengths near 2 μm, and in a reduction of the losses in both polarisations by more than three orders of magnitude near the telecommunication wavelength $\lambda = 1.55$ μm. We have also shown that WG designs with track diameters that differ from one ring to another [143] can further expand the spectral region of low-loss operation into the mid-IR range. Similarly, these designs would allow us to achieve low losses with fewer tracks.

Chapter 5

Optimisation of micro-structured waveguides for broadband operation

In the previous chapter, we have demonstrated to which extent the wave-guiding properties of depressed-cladding WGs written in $LiNbO_3$ can be controlled by the WG geometry at the induced RI contrasts that are feasible by use of current fs micro-fabrication technology. In particular, the number of track rings revealed to play a major role in the control of the confinement losses. We have also shown that WG designs with track diameters that differ from one ring to another can extend the spectral region of low-loss operation of the WG to longer wavelengths. Obviously, with virtually an infinite number of structural parameters the design of such WG structures is not as trivial. In this chapter we describe how the wave-guiding properties of MS WGs in $LiNbO_3$ can be optimised for low-loss operation in the mid-infrared spectrum [146].

It emerged from our previous study that a systematic procedure is required to find optimum laws for the variation of WG parameters such as the track size among different rings

of tracks. Another motivation for the work presented in this chapter is that, as discussed in Chapter 3, the RI contrast and the track size are not independent parameters - if the track size varies the RI contrast changes too, thus a meaningful optimisation should also account for this dependence. Additionally, the direct fs laser inscription always generates losses both within and around the tracks [130], whose effect should be properly accounted for. All the fore-mentioned effects become more significant at the long wavelengths, where we observed an unusual variation of the confinement losses in the O and E polarisations. Here, we present a practical approach to the numerical optimisation of the guiding properties of depressed-cladding WGs inscribed in z-cut $LiNbO_3$ crystals. The approach accounts for both a suitable variation of the track size among different track layers, the relationship between track size and induced RI contrast, and the intrinsic losses due to fs laser inscription [146].

5.1 Set-up of MS WG geometry for optimisation

For this study, we modelled WGs with an hexagonal packing geometry and up to seven rings of cylindrical tracks, as shown in Fig. (5.1).

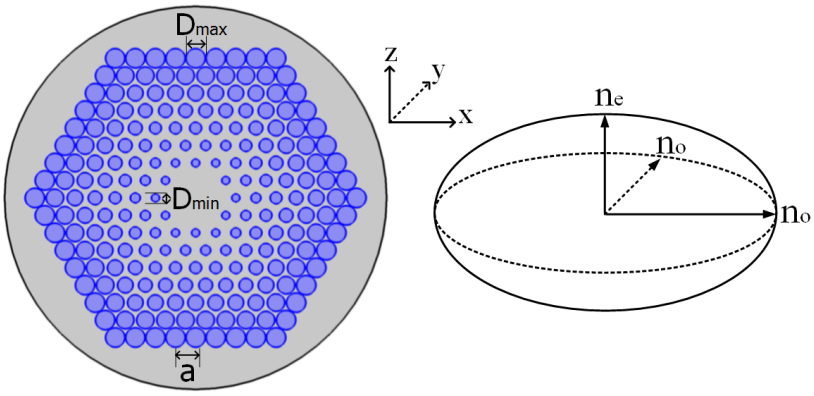

Figure 5.1: Cross-section of WG structure with seven rings of tracks with different diameters, and ellipsoid of RIs of z-cut $LiNbO_3$ crystal.

As it is shown in Fig. 3.3, the track diameter D (in [μm]) and the induced RI contrast δn

depend on the laser pulse energy E (in [nJ]), and a linear fit to the experimental data yields the following functions:

$$\delta n = -5.1 \times 10^{-4} \left(E - E_{\text{th}}\right), \quad D = 0.193 \left(E - E_{\text{th}}\right), \tag{5.1}$$

where $E_{\text{th}} = 36.45$ nJ is the energy threshold of the 100× MO used for inscription (numerical aperture NA = 1.25). These relations were found to be valid for a laser repetition rate of 11 MHz and the optimum (sample translation) inscription speed of 10 or 20 mm/s (determined by a trade-off between inscription depth and laser pulse energy), up to a maximum available laser pulse energy of approximately 75 nJ. These fitting functions serve as the basis for the optimisation of MS WGs being described. As discussed in Chapter 4, a natural strategy to extend the spectral range of low-loss operation of the WG structure, is to allow the track diameter to differ from one ring to another with the exterior rings that have large tracks. The rate of growth of the track size from the innermost to the outermost ring can be parameterised with a single parameter $p > 0$, so that the track diameter D_n in the n-th ring is:

$$D_n = D_{\text{min}} + \left(\frac{n-1}{N_r - 1}\right)^p (D_{\text{max}} - D_{\text{min}}), \quad n \in [1, N_r], \tag{5.2}$$

where D_{max} and D_{min} are the respective maximum and minimum diameters. Examples of how the growth rate parameter p changes the track diameter in a seven-ring WG structure and the cross-sections of structures for different values of p are given in Fig. 5.1.

5.2 Numerical results by PWM and comparison with FEM

As mentioned in Chapter 2, the rather large size of the PML absorber used in the FEM-based numerical model limits the number of modes that can be followed simultaneously over a wide wavelength range. In order to explore the behaviour of a larger number of modes,

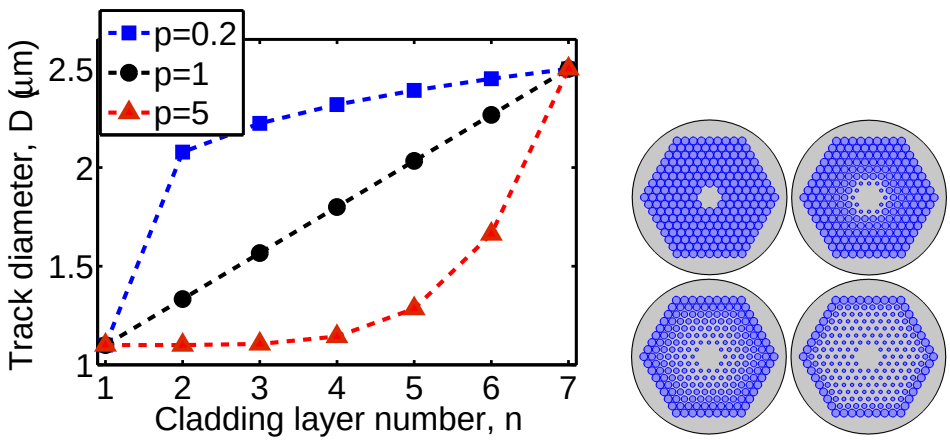

Figure 5.2: Left: track diameter versus cladding layer number for a seven-ring WG structure with different growth rate parameters p. Right: Cross-sections of seven-ring structures for (from top to bottom and left to right) $p = 0$ (uniform structure), 0.2, 1, 5. Other parameters are: pitch $a = 2.5$ μm, $D_{\max} = 2.4$ μm, $D_{\min} = 1$ μm.

we use here the PWM described in Chapter 2, and compare the results with those obtained by the FEM. For practical applications, MS WG structures built of low-RI-contrast tracks may feature low confinement losses by having a fairly large number of cladding layers. For the PWM calculations being discussed, we considered seven-ring structures with the pitch $a = 2$ μm, a track radius of $r = 0.8$ μm and a track RI contrast of $\delta n = -0.01$. The Fourier coefficients and matrices $U_{o,e}$, $P_{o,e}$, etc. in Eqs. 2.17 were calculated for values of the indices m,n up to ± 35, and 578 PWs. These PWs included mostly modes propagating along the x-axis. The eigenvalue problem was solved numerically using the "cg.f" program from the "EISPACK" package (NetLib). Figure 5.3 shows the computed modes of the structure. We can note an overlap between the O and E polarisations at the wavelength of 1.5 μm. This overlap will lead to additional losses in the E mode due to a perturbation induced in the WG.

In Fig. 5.4, the effective RI profiles for the fundamental mode are compared to those obtained using the FEM. The PWM and FEM results are in excellent agreement for the O polarisation, whereas a small deviation within the wavelength range 0.5 μm to 1.5 μm can be observed for the E polarisation. This is likely due to a leakage of the E mode with

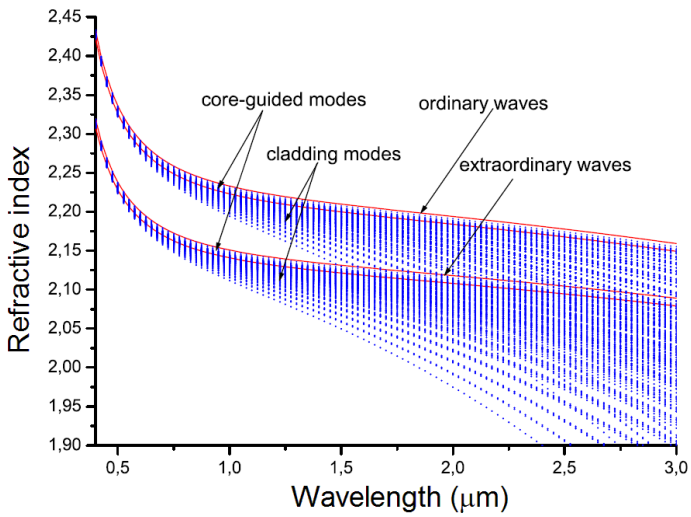

Figure 5.3: Real parts of effective RIs as a function of wavelength for the PWM computed modes of a WG structure with seven rings of tracks.

Table 5.1: Real parts of effective mode indices for O and E waves calculated using the PWM and the FEM. The RIs of the unmodified material $n_{o,e}$ are also displayed.

λ (μm)	n_o	n_e	$\mathcal{R}\left(n_o^{\text{eff}}\right)_{\text{PWM}}$	$\mathcal{R}\left(n_e^{\text{eff}}\right)_{\text{PWM}}$	$\mathcal{R}\left(n_o^{\text{eff}}\right)_{\text{FEM}}$	$\mathcal{R}\left(n_e^{\text{eff}}\right)_{\text{FEM}}$
0.5	2.33624	2.23809	2.3354	2.2372	2.33543	2.23728
1	2.23297	2.15087	2.23	2.1498	2.23001	2.14791
1.5	2.20986	2.13135	2.2039	2.129	2.20547	2.12545
2	2.19398	2.11805	2.1847	2.1087	2.18470	2.10877
2.5	2.17775	2.1045	2.165	2.098	2.16498	2.09173
3	2.15921	2.08905	2.1431	2.0758	2.14301	2.07285

lower RI into the higher-RI O polarisation, which is not accounted for by PWM calculations. The effective mode index values obtained from PWM and FEM calculations at different wavelengths are given in Table 5.1.

5.3 Optimisation of WG structural parameters

To minimise the confinement losses in the WG structure at the long wavelengths and, thus, extend the spectral range where the loss figures for the modes are acceptably low, we performed FEM simulations. A simple idea to address the numerical optimisation problem described in this chapter came from the observation that the confinement losses become monotonic

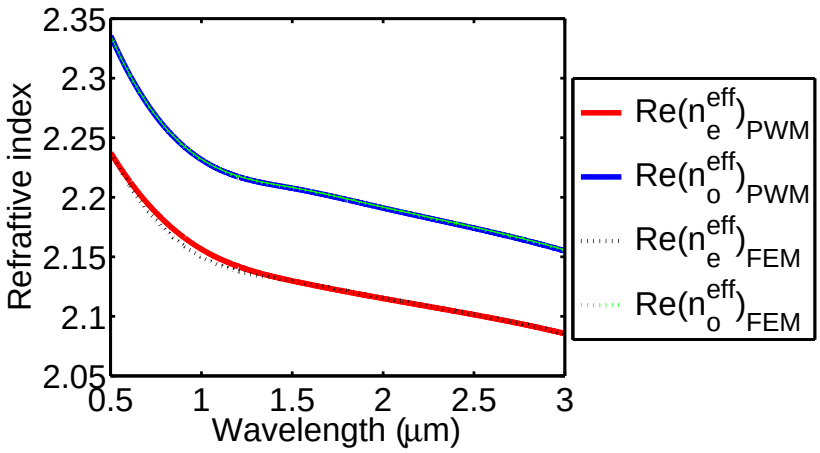

Figure 5.4: Real parts of effective RIs for O and E waves as a function of wavelength for the fundamental mode of a seven-ring WG structure, as obtained from PWM and FEM simulations.

functions of wavelength at sufficiently long wavelengths. Thus, one can vary different WG structural parameters at a fixed wavelength of interest, and only when the best loss figures are obtained, perform a full wavelength scan. This makes the optimisation procedure much less time consuming and practically feasible.

The RI contrast induced by fs inscription is the most important parameter for mid-IR operation of the WG. Figure 5.5 illustrates the dependence of the confinement loss on the track diameter at the wavelength $\lambda = 1.55\,\mu$m for a seven-ring, uniform ($p = 0$) structure with different values of δn. It is seen that for $\delta n = -0.01$ and $\delta n = -0.02$ there is a "plateau" of low losses over the diameter range from 2.2 μm to 2.5 μm, and from 1.4 μm to approximately 2.2 μm, respectively. Remarkably, such a plateau does not appear for lower RI contrasts, which are typically obtained by low-repetition rate fs laser inscription [25]. As mentioned in the previous chapters, the RI contrasts of smooth tracks that can be achieved in crystals with current fs micro-fabrication technology are around -0.01. Higher RI contrasts can still be obtained by fs inscription, with the fs laser creating severe damage tracks inside the bulk at the focal volume [147, 148]. Damage tracks, however, are not smooth and, thus, typically

not suitable for low-loss light guiding.

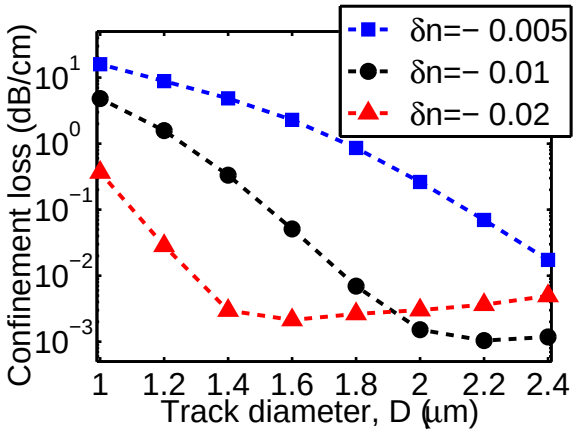

Figure 5.5: Confinement loss for E wave at $\lambda = 1.55$ μm versus track diameter for a seven-ring WG structure with $a = 2.5$ μm and different values of δn.

The influence of a varying track diameter among the different cladding layers on the loss properties of the WG at the wavelengths 1.55 μm and 3 μm is illustrated in Fig. 5.6. Our simulations showed that the most interesting range of growth rate parameter values is $0 < p \leq 1$. It can be seen from Fig. 5.6 that as p decreases from 1, the confinement loss also decreases down to much lower values than that of a uniform structure (corresponding to $p = 0$ when $D_n = D_{\max}$ $\forall n$). At $\lambda = 1.55$ μm, the loss profile is flat over the p range $p \to 0$ (yielding $D_1 = D_{\min}$ and $D_n \approx D_{\max}$, $n > 1$) to $p = 0.5$ for the maximum track diameter $D_{\max} = 2.4$ μm. For a uniform structure $D_{\max} = 2.2$ μm yields lower confinement loss than $D_{\max} = 2.4$ μm. On the other hand, the loss for a structure with $p = 1$ is higher than that for the uniform structure at $D_{\max} = 2.2$ μm. Differently, at $\lambda = 3$ μm the decrease of the confinement loss with decreasing p values is approximately linear for both $D_{\max} = 2.2$ μm and $D_{\max} = 2.4$ μm. The smallest loss value of $\mathcal{L} = 0.5$ dB/cm is obtained for p very close to 0 and $D_{\max} = 2.4$ μm. The possibility of achieving such low loss figures at $\lambda = 3$ μm makes the WG suitable for mid-IR applications. Note that the transparency region of the WG can be further extended to longer wavelengths by increasing $D_{\max}$ and properly fitting

the p parameter to the RI contrasts being used.

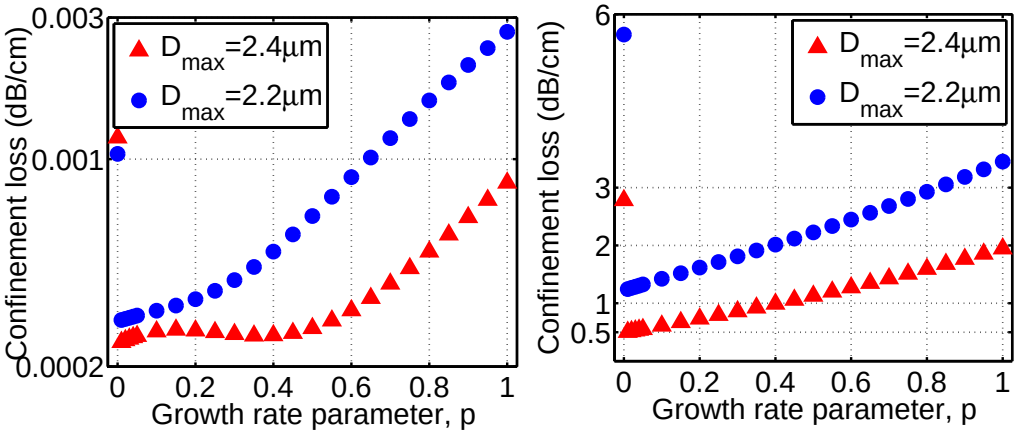

Figure 5.6: Confinement loss for E wave versus growth rate parameter p at $\lambda = 1.55$ μm (left) and $\lambda = 3$ μm (right), for a seven-ring WG structure with $\delta n = -0.01$. Here, $D_{\min} = 1$ μm.

Figure 5.7 shows the variation of the confinement loss across the wavelength range 0.3 μm to 3 μm for WG structures with various growth rate parameters. One can see that while for a uniform structure the losses in both O and E polarisations are below 1 dB/cm for wavelengths up to approximately 1.8 μm, the spectral range where the losses are acceptably low is extended up to $\lambda = 3$ μm for a structure with $p = 0.01$. The optimisation of the growth rate parameter results in a reduction of the losses in both polarisations by two orders of magnitude at $\lambda = 3$ μm. One may also notice that while the confinement losses of a WG with $p = 0.5$ are lower than those of a WG with $p = 1$ for wavelengths below 2.6 μm, a reversal of trend happens at the wavelengths above 2.6 μm. Further, Fig. 5.6 highlights the distinctly different behaviours of the confinement losses in the O and E polarisations at the low wavelengths. The confinement loss for the E wave stops decreasing with decreasing wavelength below some wavelength which is specific to the WG structure, and features resonance effects. The critical wavelengths below which such behaviour is observed are 1.8 μm, 1.6 μm, 1.4 μm and 1.2 μm for WGs with the respective growth rates $p = 0.01$, $p = 0.5$, $p = 1$ and $p = 0$. This resonance behaviour which is peculiar to E polarised propagating

waves in anisotropic WGs, stems from the coupling of the E-polarised fundamental mode to the radial modes of O polarisation and consequent leakage of the E wave through these modes [61].

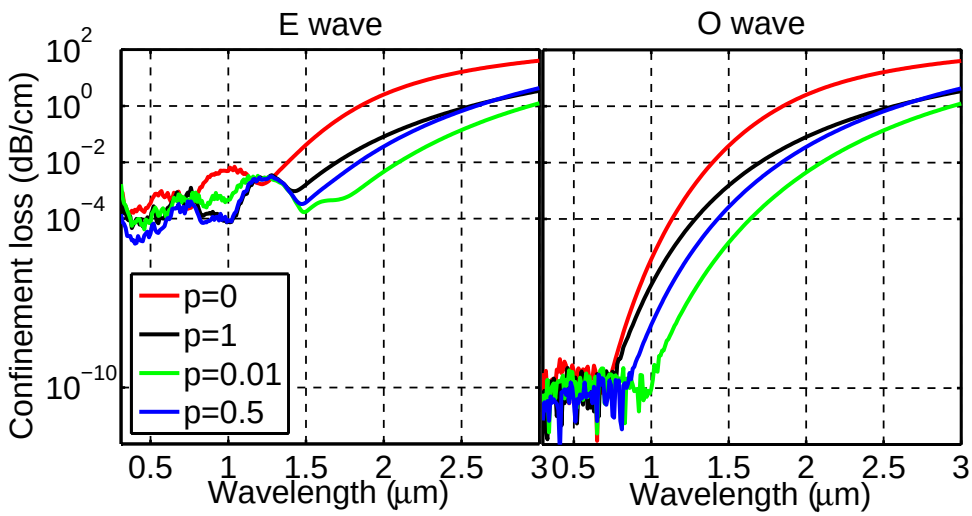

Figure 5.7: Confinement losses for O and E waves as a function of wavelength for a seven-ring WG structure with different growth rate parameters p. Other parameters are: $\delta n = -0.01$, $D_{\max}$ =2.2 μm, $D_{\min}$=1 μm.

The results presented so far were obtained by assuming that the RI change induced in the material by direct fs laser inscription is a real value. In fact, as previously mentioned, the fs irradiation always induces material absorption, which needs to be accounted for in the WG design. To this end, we computed the confinement loss in a WG with $p = 0$ and $p = 0.5$ at $\lambda = 1.55$ μm, and with $p = 0.01$ at $\lambda = 3$ μm for a range of fs laser-induced loss values. The results are shown in Fig. 5.8, which reveals that the higher is the confinement loss of the WG, the lower is the WG sensitivity to the imaginary part of the induced RI contrast. Indeed, induced losses of up to 1 dB/cm do not affect the confinement loss at $\lambda = 3$ μm, whereas the effect of induced loss is more important at $\lambda = 1.55$ μm, where the WG exhibits lower confinement loss. We note that the imaginary part of the modified RI could be measured by using, for example, the Born scattering interferometry method recently proposed in [130].

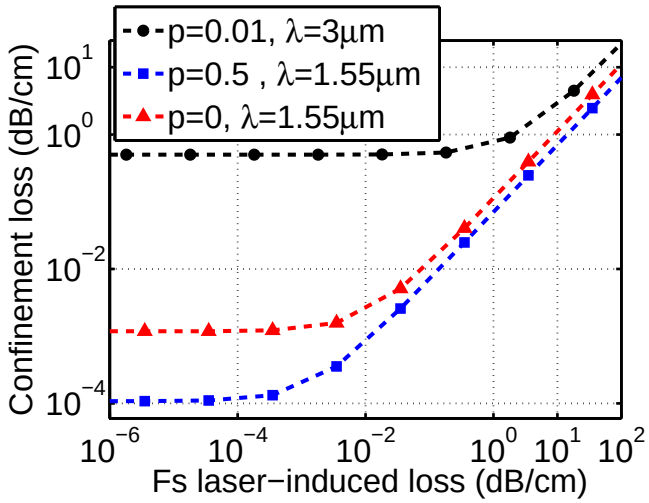

Figure 5.8: Confinement loss for E wave versus loss induced on tracks by fs inscription for a WG with $p = 0$ and $p = 0.5$ at $\lambda = 1.55$ μm, and with $p = 0.01$ at $\lambda = 3$ μm. Other WG parameters are: $\delta n = -0.01$, $a = 2.5$ μm, $D_{\text{max}} = 2.4$ μm, $D_{\text{min}} = 1$ μm.

Finally, we included in our design procedure also the relationship between induced RI contrast δn and track size D. Indeed, as we mentioned before, the dependence of δn and D on the laser pulse energy makes such parameters correlated if the sample translation speed is fixed (Eq. (5.1)). Note that it is possible to experimentally trim these parameters to the desired values by tuning both the laser pulse energy and the sample translation speed, which as both produce albeit connected but not identical changes to δn and D (cf. Chapter 3). Simulation results are presented in Fig. 5.9, which shows the variation of the confinement losses in the O and E polarisations as a function of wavelength for a seven-ring WG structure with a growth rate parameter of $p = 0.01$ and where the RI contrast was changed from one ring of tracks to another following the change in the track size. It is seen that the spectral region where the losses in both polarisations are below 1 dB/cm extends up to 3.5 μm for this optimised structure.

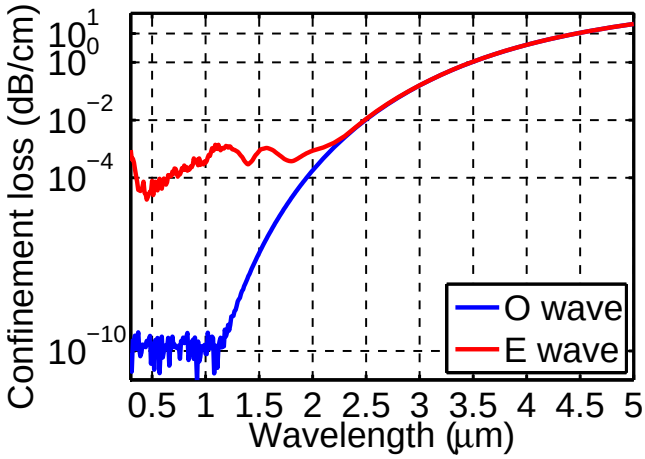

Figure 5.9: Confinement losses for O and E waves as a function of wavelength for a seven-ring WG structure with $p = 0.01$. Other parameters are: maximum RI contrast $\delta n = -0.01$, $D_{\max} = 2.4\ \mu$m, $D_{\min} = 1\ \mu$m.

5.4 Summary

A numerical approach to the optimisation of the guiding properties of depressed-index cladding WGs in a z-cut $LiNbO_3$ crystal by direct fs laser inscription has been presented. The approach accounted for both a suitable variation of the track size among different cladding layers, the relationship between the track sizes and induced RI contrasts, and the losses induced on the tracks by fs irradiation. We have shown that the spectral region where the confinement losses in both O and E polarisations are acceptably low (below 1 dB/cm) can extend up to a wavelength of 3.5 μm for optimised, hexagonal WG structures with seven rings of tracks. This makes such structures suitable for mid-IR applications. We note that the possibility of further extending the low-loss operation region of these WGs depends on the ability to experimentally achieve higher RI contrasts than those which are currently achieved by fs micro-fabrication technology.

Chapter 6

Advanced waveguide geometries

6.1 Introduction

Various geometries of MS WGs have been explored over the years for the purpose of improving the propagation properties of light in a wide number of optical applications [39, 40, 141, 149]. The kind of possible WG geometries has generally been dependent on the ability of any fabrication technology to form specific RI modulated areas in a WG material. As the most commonly considered, geometries with translational symmetries (triangular, square and hexagonal geometries) have successfully been applied on fulfilling the potentials of PhC technology. As one of the primary reasons to study in the previous chapters, the hexagonal geometry has been known to provide with the densest packing of tracks/rods, thereby allowing for the lowest leakage of the propagation modes [141]. However, the use/study of more complex or advanced geometries has generally been restricted due to the difficulties on fabricating specific shapes and sizes of tracks/rods. It is shown [45] that tracks in $LiNbO_3$ can be fabricated at varying sizes, and this allows for the design and fabrication

of more advanced WG structures.

Among the structures with the lack of translation symmetry, spirals [150, 151] are the most attractive from our point of view, as the geometrical curves which turn around a fixed center point and in which radius vector changes both its length (i.e. radius) and direction (i.e. polar angle) in accordance with a certain law [152]. Spiral equations can most easily be derived in the polar coordinate system, and one can construct structures with both adjustable high order rotational symmetries or no rotational/translational symmetry. Spirals are very

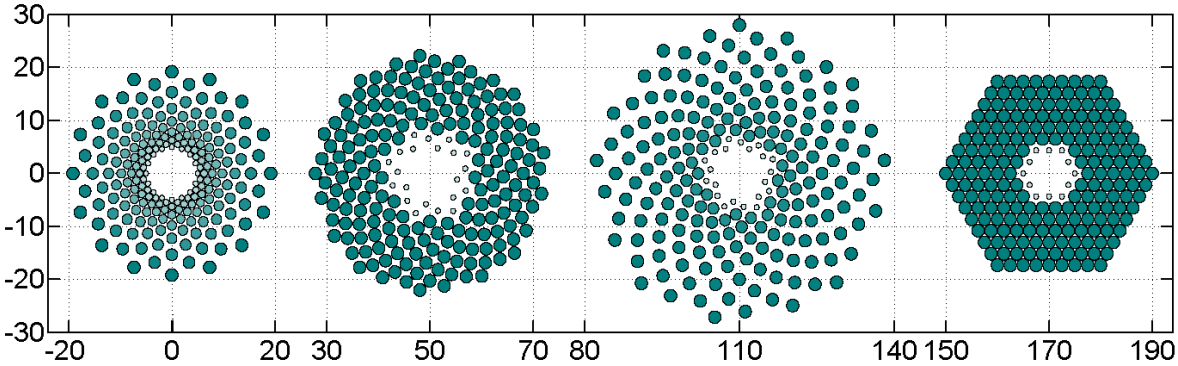

Figure 6.1: Cross sections of MS WGs with optimised parameters of Equiangular spiral geometry, Fermat spiral geometry, Archimedes spiral geometry and Hexagonal geometry.

abundant in Nature because it reflects the harmony and balance of dynamical systems that living or non-living structures follow during their formation and growth [151]. The design of many human-made products have been inspired by spiral geometries. In recent years, various optical devices with 1D, 2D or 3D spiral geometries have also been proposed, such as, antennas [153, 154], micro-disk resonators [155–157], WG Bragg gratings [158] and optical delay lines [159]. The design of MS fibers with 2D spiral geometries has also been proposed to achieve, such as, high birefringence [160,161], increased nonlinearity [161,162], tunable zero dispersion wavelength [163] and low bending and confinement losses.

As one can see on the Fig. 6.1, the spiral geometries can allow for both dense packing

and variable 'periods' at the same time, which was not possible with hexagonal geometry (as it had a translation symmetry, i.e. the period was constant). So, the spirals can offer a number of additional design parameters, which needs to be explored.

6.2 The design of MS WGs with spiral geometries

In this work, 3 different spiral geometry has been studied. The first one is the Equiangular spiral (ES) [150,162,164], in which the radius grows exponentially with identical increments in polar angle. The second one is the Fermat spiral (FS), in which the radius scales as a square root of identical angle increments, thereby producing almost equally separated spiral arms. In the third case it scales linearly with the angle, giving the Archimedes spiral (AS). The curve of an ES spiral can generally be expressed in polar coordinates (ρ,θ) by the equation $\rho = ae^{b\theta}$, where ρ is the distance from the center, θ is the angle, a is a real constant of the spiral, and b is a positive number called 'growth constant', $b = \cot\alpha$ [164]. The angle (α) between the line from the spiral center towards a point on the spiral curve and its tangent is same for all points on the ES curve, an indication of a self-similar property such that the shape of the curve does not change while it grows outwards [164]. Archimedian spiral is a general name including a group of spirals, and it is formulated in polar coordinates by the equation $\rho^n = a^p\theta$, where a is a real constant and n is the power coefficient. Both FS and AS are two different types of Archimedian spiral, differing from each other by the value of p ($p = 1/2$ for FS and $p = 1$ for AS).

To design a MS WG by using an ES geometry, we had to use multi-arm spirals, not a single one. We can define the positions of all tracks ($R_{n,m}$,$\phi_{n,m}$) in polar coordinate system ($R_{\mathrm{n,m}}$ and $\phi_{\mathrm{n,m}}$ are the radial distance and polar angle, respectively, of the n-th track in the

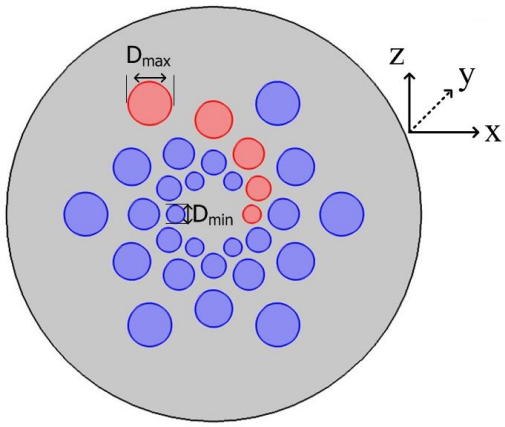

Figure 6.2: Cross section of ES modeled depressed-cladding WG with six arms ($M_{\text{arm}} = 6$) and five ring ($N_{\text{ring}} = 5$) of tracks

m-th arm , i.e. the index n - is the sequential number of the point/track in the arm of the ES spiral, $n = 1...N_{\text{ring}}$, m is the number of the arm, $m = 1...M_{\text{arm}}$, where this n-th track is located). A MS WG consisting of six arms ($M_{\text{arm}} = 6$) and five rings ($N_{\text{ring}} = 5$) within an ES geometry is shown in Fig. 6.2. The tracks in the first arm is colored by red. The total number of tracks in the structure with ES geometry (we agreed to keep it approx. constant) is: $N_{\text{total}} = N_{\text{ring}} \cdot M_{\text{arm}}$. The location of any track can be defined by using the track positions in the first arm ($m = 1$) [162]:

$$R_{n,1} = R_0.e^{\theta(n-1)cot\alpha} \tag{6.1}$$

$$\phi_{n,1} = \theta(n-1) \tag{6.2}$$

To build the whole multi-arm geometry we implement the rotation operator, $\widehat{T}$; T is the rotation angle for the whole arm ($T = 2\pi/M_{\text{arm}}$). Since two nearby tracks on a ring is separated by a polar angle of T, and a track on the following ring should be placed at an equal polar angle difference from both the track on the previous ring of the same arm and the track next to it, θ in Eq. (6.1) becomes θ=$T/2$ =π/M_{arm} [162, 165, 166]. So the positions of

tracks ($x_{n,m}$,$y_{n,m}$) in Cartesian coordinate system is:

$$\begin{pmatrix} x_{n,m} \\ y_{n,m} \end{pmatrix} = \begin{pmatrix} Cos(2\theta \cdot (m-1)) & -sin(2\theta \cdot (m-1)) \\ Sin(2\theta \cdot (m-1)) & Cos(2\theta \cdot (m-1)) \end{pmatrix} \begin{pmatrix} R_{n,1} \cdot Cos(\theta \cdot (n-1)) \\ R_{n,1} \cdot Sin(\theta \cdot (n-1)) \end{pmatrix} \tag{6.3}$$

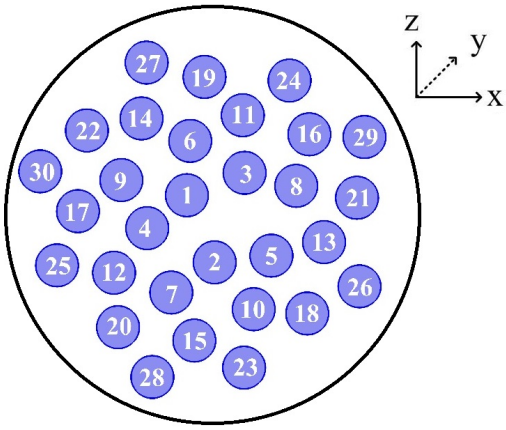

Figure 6.3: Positions of tracks within FS geometry

The design of a MS WG by using FS or AS geometry can be realised by positioning all tracks just on a single arm without any need for rotations. The positions of tracks in polar coordinates (R_n,ϕ_n) can be defined by the following equation:

$$R_n = R_0(n\theta)^p, \quad n \in [N_0, N_0 + N_{\text{total}} - 1] \tag{6.4}$$

$$\phi_n = n\theta \tag{6.5}$$

where R_0 is spiral radius and p is power coefficient. A core region can be designed by omitting a certain number of tracks from $n = 1$ to $n = N_0 - 1$, where N_0 is the starting track number to form cladding region. A total number of N_{total} tracks can be positioned in the cladding region starting from $n = N_0$ to $N_0 + N_{\text{total}} - 1$. The arrangement of tracks within both FS and AS geometries have been governed by accepting the value of θ as the golden angle ($\theta = \pi(3 - \sqrt{5}) = 137.507..^\circ$) [152], which is the smaller of two angles corresponding to the two arcs obtained by dividing a circle into two parts with a golden ratio [167] such that

the ratio of the bigger arc to the smaller arc is equal to the ratio of the full circle to the bigger arc. Being seen also in nature, for example, in the arrangements of leafs on some plants or of seeds on sunflowers, spirals with golden angle is shown to provide with the optimal filling of space with minimal overlaps [152], because successive rotations never end up at the same polar angle since the value of the golden angle is an irrational number.

In most of the spiral geometries observable in Nature, specimens like seeds, leafs, and so on, located on the spiral arms show a varying size profile. This is because spirals reflect the optimum geometry during the appearance and growth of those specimens [151]. It was shown that writing tracks at varying sizes is possible [45]. The design of a MS WG with varying sized tracks on spiral geometries brings an extra degree of freedom to adjust WG properties by increasing the possible range of spiral design parameters. On the other hand, incorporation of possible track sizes and RI contrasts is a challenging task for both the design and optimisation of those MS WGs, and should be carefully handled. A linear fit was already applied on experimentally achieved track diameters and induced RI contrasts (cf. Eq. (5.1)), which are both co-related by the applied pulse energy (if the sample translation speed is fixed). Following a similar design strategy as in [146], track sizes are allowed to increase from innermost ring to outermost ring. The sizes of tracks in each ring has been calculated by the following equation:

$$D_n = D_{\min} + \left(\frac{n-1}{N_{\text{ring}}-1}\right)^p (D_{\max} - D_{\min}), \quad n \in [1, N_{\text{ring}}], \tag{6.6}$$

where $D_{\max}$ and $D_{\min}$ are the respective maximum and minimum track diameters, p is a parameter to control the growth rate of track sizes, N_{ring} is the number of rings, n is the corresponding ring that a track is located.

For spiral geometries holding rotational symmetries such as ES geometry, that is easy

to identify specific rings in which a group of tracks are equally distanced from core center, and the Eq. (5.1) and Eq. (6.6) can be easily applied on tracks according to corresponding ring number in which a track resides. However, MS WGs with FS and AS geometries has been formed on a single arm in this work, therefore the radial distance of all tracks get a different value. Also, when θ is chosen as a golden angle, all tracks take place at a different polar angle. As a consequence, there will exist no specific ring formation. In this case, the strategy followed is based on classifying all tracks in some pseudo-rings according to their distance from the core center; first, N_{ring} is determined, then $N_{\text{total}}/N_{\text{ring}}$ tracks closest to core center are categorised as existing in the first ring, and following $N_{\text{total}}/N_{\text{ring}}$ closest tracks are categorised as existing in the second ring, and so on. Tracks which are located inside any of the corresponding ring are assumed to have a same track size and RI contrast.

6.3 Optimisation of WG structural parameters

The optimisation of MS WGs designed by ES, FS and AS geometries, and a comparison between each other with respect to their confinement properties are much more complex to handle than those of MS WGs with conventional geometries, since each spiral geometry has a multitude of specific design parameters and different shapes, let alone the parameters for the variation of track sizes. Moreover, optimisation by tuning spiral parameters around intuitively chosen values may not produce proper structures worth any evaluation due to, such as, track overlaps or excessive core or cladding sizes. To exclude such structures, some properties of MS WGs, such as core and cladding sizes, have only been accepted in certain limits, and parameter sets realising only several criteria have been used during optimisation. To design MS WGs which have similar structural traits to previously studied hexagonal

geometry, and to make it easier to compare between those structures, the design of MS WGs with spiral geometries has been based on using the same number of tracks in the cladding region and similar core sizes as with seven rings hexagonal geometry. MS WGs with seven ring hexagonal geometry consisted of 210 tracks, and tracks at hexagonal corners of the first ring were positioned at a 5 μm distance from the core center. Also, the distances between nearby tracks follow an irregular order in spiral geometries. Therefore, as a design strategy, the minimum track separation distance − between the outer regions − of tracks have been set to a fixed value of 0.1 μm.

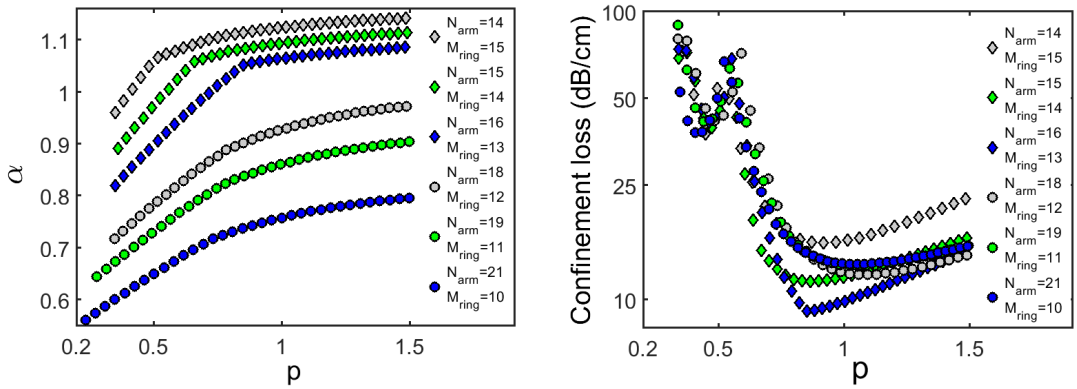

(a) (b)

Figure 6.4: (a) α and p pairs, and (b) confinement losses of MS WGs with ES geometry at 3 μm wavelength.

The design and optimisation of each spiral geometry involve a different evaluation process by using specific design parameters; N_{arm}, N_{ring}, R_0, α and p for ES geometry, and R_0, N_0, N_{total} and p for FS and AS geometries. For ES geometry, firstly, N_{arm} and N_{ring} parameters providing a total track number (N_{total}) of 210 is determined. Then, for each N_{arm}-N_{ring} pair, tracks at the first ring is adjusted to be at a 5 μm distance by setting $R_0 = 5$ μm. The minimum of all of the track separations has been adjusted to be at 0.1 μm with no overlap of tracks by finding specific α-p pairs shown in Fig. 6.4(a). Confinement losses at 3 μm

wavelength on those MS WGs with given $\alpha - p$ pairs have been calculated, as shown in Fig. 6.6(a). The lowest value of confinement loss has been obtained for a MS WG with the following parameters of ES geometry: $N_{\text{arm}} = 16$, $N_{\text{ring}} = 13$, $\theta = \pi/16$, $R_0 = 5$, $\alpha = 1.0524$, $p = 0.8536$.

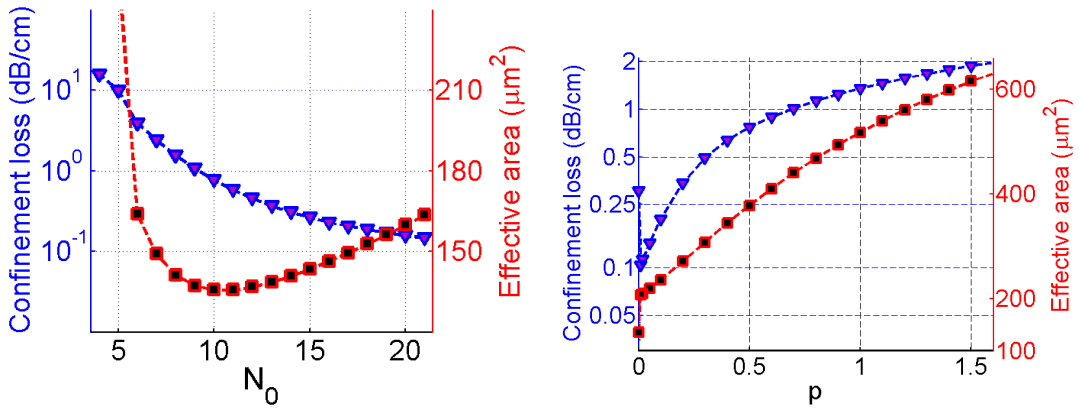

Figure 6.5: The change of confinement loss (blue) and effective area (red)(a) by N_0 ($N_{\text{total}} = 210$, $p = 0$), and (b) by p ($N_0 = 11$, $N_{\text{total}} = 210$) for a MS WG with FS geometry at 3 μm of wavelength.

For both of the FS and AS geometries (cf. Eq. (6.4)), N_{total} is chosen as 210, θ is a constant number (Golden angle), so R_0, N_0 and p remain to be determined. In the case of just FS geometry, separation distances between nearby tracks on all over the cladding region are very similar (cf. Fig. 6.3) due to the almost constant growth rate of FS geometry. So, the change of p in Eq. (6.6) does not make much impact on the variation of the core size. It has been observed that, when N_0 is bigger than 5, R_0 remains same. Only way to fix the position of the closest track to the core center at 5 μm remains the adjustment of starting track number (N_0). Fig. 6.5(a) shows the change of confinement loss by N_0 when all FS design parameters are kept same ($N_{\text{total}} = 210$, $p = 0$). It can be seen that the lowest confinement loss is obtained for $N_0 = 11$. Interestingly, the radial distance of $N_0 = 11$-th track to core center becomes

5.008 μm, which is closest to 5 μm. After setting $N_0 = 11$ and corresponding $R_0 = 0.9747$, optimisation of MS WGs with FS geometry has been realised by keeping the positions of all tracks same and by changing just the p parameter. As shown in Fig. 6.6(b), the lowest confinement loss at 3 μm wavelength has been obtained by a MS WG with the following parameters of FS geometry; $R_0 = 0.9747,\ p = 0.01,\ N_0 = 11,\ N_{\text{ring}} = 10,\ N_{\text{total}} = 210$.

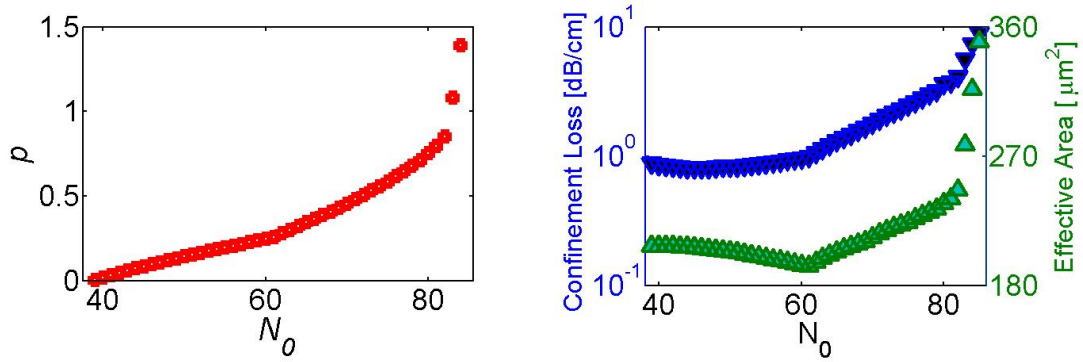

(a) (b)

Figure 6.6: (a) $N_0 - p$ pairs, and (b) confinement losses of MS WGs with $N_0 - p$ pairs of AS geometry at 3 μm wavelength ($N_{\text{total}} = 210$).

In the case of AS geometry, the growth rate of separation distances between tracks from inner side to outer side shows similarity to ES geometry. The radial distance of the first track to core center – if the smallest of track separations is kept at a certain value – highly depends on p parameter, as well as N_0 and R_0, which means that it is possible to flexibly adjust the core and cladding structure. So, it is possible to find a multitude of N_0 realising our criteria. For different N_0 values, all N_0-p pairs providing both the smallest track separation at 0.1 μm and the first track located at a 5 μm distance have been searched. It is found that a MS WG with the above given criteria can be obtained when N_0 is between 39 to 85 with corresponding only one p and R_0 values for each. Those N_0-p pairs can be seen in Fig. 6.6(a). The confinement loss and effective area of light at 3 μm wavelength for MS WGs with those $N_0 - p$ pairs of AS geometry are shown in Fig. 6.6(b). The lowest confinement

loss at 3 μm wavelength has been obtained by a MS WG with the following parameters of AS geometry; $N_0 = 45$, $R_0 = 0.0463$, $p = 0.083$, $N_{\text{ring}} = 10$). On the other hand, the effective area has the lowest value when N_0 is 61.

6.4 Comparison of MS WG geometries in $LiNbO_3$

The ability to fabricate varying sizes of tracks in $LiNbO_3$ provide with greater freedom to design MS WGs with spiral geometries. It allows to design advanced geometries of 2D circular WGs with adjustable lengths of core and cladding regions with varying local densities of tracks. As one of the most suitable to utilise track size variations, spiral geometries offer the advantage of adjusting flexibly the propagation properties of MS WG structures, such as dispersion, confinement loss, birefringence, effective area and so on.

In this work, the design of MS WGs with three different spiral geometries; ES, FS and AS have been studied based on the experimentally obtained parameters by direct HRR fs laser inscription in $LiNbO_3$. So, optimised parameters of MS WGs with each spiral geometry should be considered as a result of presently achieved experimental parameters. Improving the properties of MS WGs with a much better control on the propagation properties of light may even become possible by achieving flexibly obtainable experimental parameters, such as varying sizes of tracks accompanied by constant RI contrasts.

$LiNbO_3$ has a very wide transmission window, which allows a wide range of applications operating at telecommunication, mid-IR, and ultraviolet wavelength regions. Some applications such as frequency conversion devices even require the propagations of more than one light at different wavelength regions together in the same WG so as to obtain maximum conversion efficiencies. In the light of general design concepts of MS WGs with spiral

geometries, as given above, it is always possible to choose the most appropriate geometry and to find the optimised parameters in accordance with the specific needs of $LiNbO_3$ applications. In this work, MS WGs in $LiNbO_3$ with different design geometries have been compared with a focus on confinement losses at 3 μm wavelength of light. Considering a high number of different geometric design parameters, a comparison has been realised between MS WGs which have similar core sizes and which use the same number of tracks in their cladding regions. Core sizes have been approximated to be similar by positioning the nearest tracks at the same distance to core centre in each geometry .

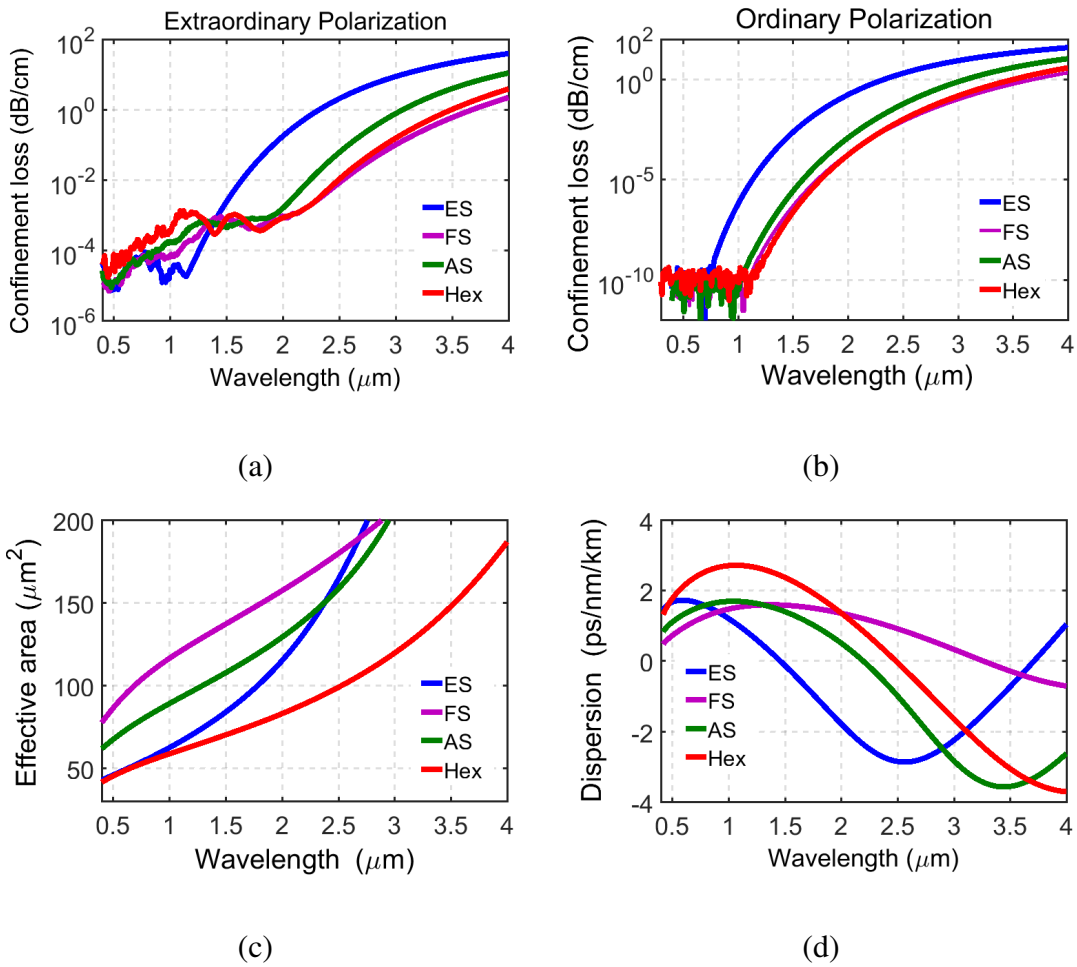

Figure 6.7: A comparison of MS WG geometries in terms of confinement loss for (a) E polarisation, (b) O polarisation, (c) effective area and (d) WG dispersion.

The propagation properties (confinement loss for O and E polarisations, effective area

and WG dispersion) of MS WGs with optimised parameters have been shown in Fig. 6.7. The best results in terms of confinement loss have been obtained by FS geometry. In our previous work, the optimisation of an hexagonal geometry with 7 rings of tracks had resulted in the extension of the wavelength of 1 dB/cm confinement loss from 2.94 μm to 3.48 μm [146]. In this work, the optimisation of a MS WG with FS geometry has provided a better result with an extension of the wavelength of 1 dB/cm confinement loss from 3.295 μm to 3.665 μm. For MS WGs with optimised parameters of ES and AS geometries, the maximum wavelengths of 1 dB/cm confinement losses have been calculated to be 2.315 and 3.054 μm, respectively. On the other hand, it can be seen in Fig. 6.7(c) that hexagonal geometry provides a better result in terms of the effective area. At the wavelengths of 1 dB/cm confinement loss, the effective areas of propagating light in MS WGs with optimised parameters of ES, FS, AS and hexagonal geometries have been found to be 143.4, 252.15, 213.3 and 146.8 μm^2, respectively.

It is also worth considering to evaluate those results with respect to the structural differences of MS WGs with those geometries. First, the density of tracks over the cladding region of a MS WG with hexagonal geometry do not change from inner side to outer side. However, the density of tracks on different parts of MS WGs with spiral geometries may show big differences. Secondly, considering the experimentally obtained parameters that RI contrasts of tracks with smaller sizes are less than those of tracks with bigger sizes, average RI contrasts in inner sides of each cladding region with ES and AS geometries become less, even though tracks may become positioned more densely on those parts. Propagation properties of MS WGs with ES and AS geometries, such as confinement loss and effective area, could get better if tracks could have been written at varying sizes with constant RI contrasts. On the other hand, some other properties, such as dispersion and zero dispersion wavelength,

can be controlled better over a wide frequency range by the variation of both track sizes and RI contrasts. Fig. 6.7(d) shows the waveguide dispersions of MS WGs with optimised parameters. As it can be seen, all WG dispersion profiles are very different, and zero dispersion wavelength can be tuned over a very wide wavelength range.

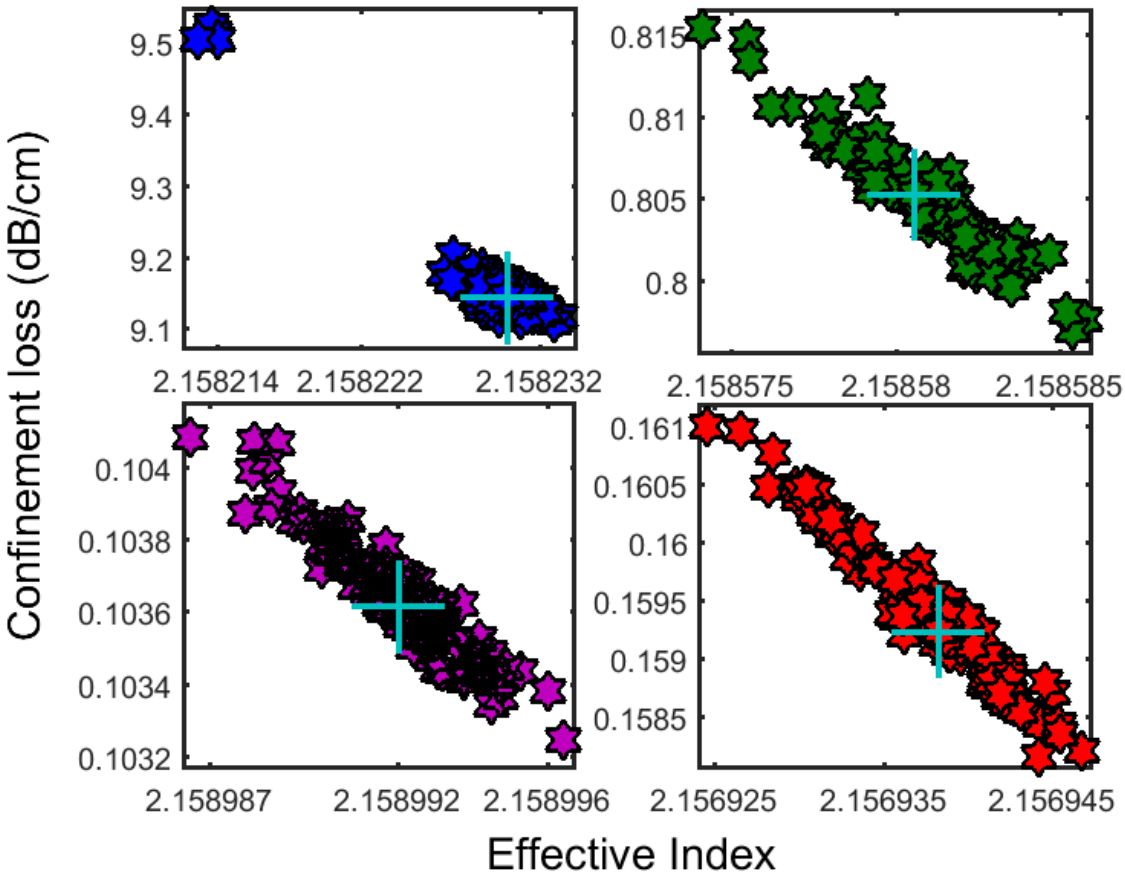

Figure 6.8: The change of confinement loss by positioning errors of tracks in MS WGs with ES (blue), FS (pink), FS (green) spiral geometries and hexagonal (red) geometry for O polarisation vs. effective RI (n_O^{eff}) at 3 μm wavelength.

MS WGs with hexagonal and spiral geometries should also be compared with respect to the stability of propagation properties in case positions of tracks may have been fabricated by errors during inscription process. For an evaluation purpose of the effect of positioning errors, the positions of tracks in MS WGs with optimised parameters of all studied geometries have been induced a random noise along transverse directions of Cartesian coordinate system.

Any overlap of tracks have been assumed to be not occurring by keeping the maximum level of absolute position fluctuation of each track at half of the minimum track separation. Fig. 6.8 shows the confinement losses of MS WGs at 3 μm wavelength when randomly generated noises have been induced on the positions of all tracks. A comparison between how MS WGs with different geometries react on any positioning error is made by calculating the rate of mean absolute deviation of confinement loss to the confinement loss without any noise induced, as expressed by the following equation:

$$Deviation\ Rate = \frac{\sum_{i=1}^{j} |\mathcal{L}_i^{with-noise} - \mathcal{L}^{without-noise}|}{j \cdot \mathcal{L}^{without-noise}} \tag{6.7}$$

where $\mathcal{L}_i^{with-noise}$ is confinement loss (dB/cm) when positioning noise has been introduced, $\mathcal{L}_i^{without-noise}$ is confinement loss (dB/cm) when tracks are on their original positions, j is iteration number. To summarise the calculation process, a randomly generated noise has been induced on the positions of all tracks, and this has been repeated 100 times ($J = 100$) with different randomly generated values in each MS WG with hexagonal, ES, FS and AS geometries. Then, Eq. 6.7 has been calculated by using the 100 different confinement losses and the confinement loss of a MS WG without any noise induced. It has been found that the deviation rates of confinement losses under positioning errors are $\%0.31$ for Hexagonal, AS and ES geometries, and $\%0.13$ for FS geometry. This result shows that, under any perturbations during inscription process, the change of confinement loss for FS geometry is 2.5 times less than those of other geometries, and that FS geometry is much less vulnerable to positioning errors. All in all, the wavelengths at 1 dB/cm confinement loss and corresponding effective areas, zero waveguide dispersion wavelengths (ZDW) and stability rates of optimised WGs has been given in Table 6.1.

Lastly, it is considered to be worth evaluating the differences between the birefringence

	Wavelength (μm) at 1 dB/cm	Effective Area (μm^2)	ZDW (μm)	Stability
Equiangular	2.315	143.4	1.4642	0.31
Fermat	3.665	252.15	3.2729	0.13
Archimede	3.054	213.3	2.20	0.31
Hexagonal	3.48	146.8	2.489	0.31

Table 6.1: A comparison of optimised WG properties

properties of MS WGs with spiral geometries. Excluding intrinsic material birefringence of $LiNbO_3$, any birefringence due to WG structure arises mostly due to asymmetry of core or cladding region of MS WGs, or any perturbations that break symmetrical MS WG structure. The birefringence of MS WGs with optimised parameters of hexagonal, ES, FS and AS geometries has numerically been calculated between 0.4 μm and 4 μm wavelengths of light and shown in Fig. 6.9(a). As it can be seen, the MS WG with hexagonal geometry appears to have the biggest birefringence, which is at least two times more than maximum of any spiral geometry. Indeed, hexagonal geometry have a six-fold rotational symmetry, which cause a structural difference both in core and cladding region along polarisation directions of x and y crystal axes. Optimised ES geometry, as shown in Fig. 6.1(a), has a sixteen-fold rotational symmetry. Even though the core and cladding region of optimised ES geometry has a symmetric nature along both polarisation directions, it has, interestingly, bigger birefringence than AS and FS geometries. This seems to be a direct result of the effect of material anisotropy in combination with WG geometry .

FS and AS geometries have no rotational symmetry, and tracks are distributed with golden angle. The lowest birefringence has been obtained for the MS WG with FS geometry, which has no rotational symmetry and has an approximately equal-distanced distribution of tracks. This result may appear to contradict with previous studies [168, 169] of MS fibres with FS geometry which produce even bigger birefringence than MS fibres with hexagonal

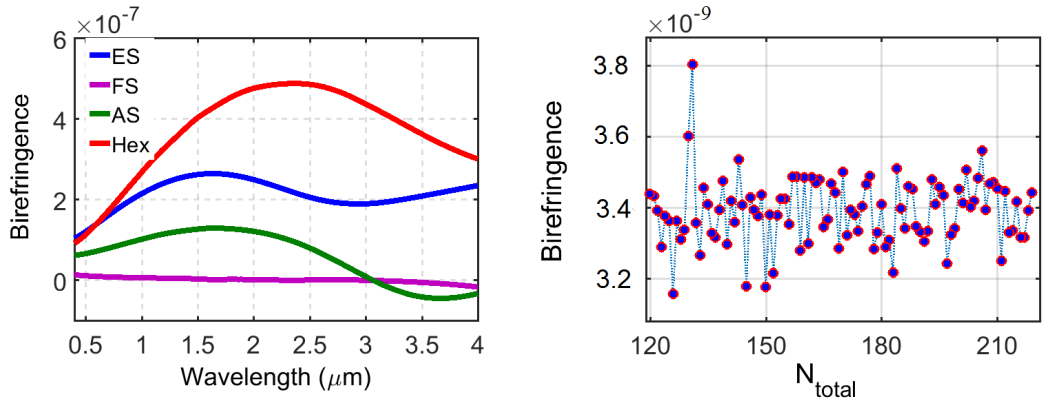

(a) (b)

Figure 6.9: (a) The change of birefringence by wavelength for optimised MS WGs with hexagonal, ES, FS and AS geometries, (b) the change of birefringence of an optimised MS WG with FS geometry by N_{total} at 1.55 μm wavelength.

geometry. Large birefringence has been explained to be due to small core area ($N_0 = 2$) and asymmetry in the air hole arrangement near the core area in [168]. However, it should be clear that there exist major differences between those and our WG structures: such as, our core area is relatively bigger ($N_0 = 11$), therefore core area appears to be much more symmetrical; RI contrast between tracks and unmodified regions is much smaller compared to RI difference between air and silica; $LiNbO_3$ is an anisotropic material while silica is an isotropic material. Additionally, it has been shown in [168] that increasing number of tracks around cladding region does not have much impact on birefringence. Indeed, cladding regions of MS WGs with FS and AS geometries (by using Golden angle) consist of tracks, each of which has been positioned at a different distance to core center and holds no rotational symmetry to other tracks. For those geometries, increasing number of tracks placed around the cladding have an averaging effect on the difference between effective RIs along x and y polarisation directions while it is a cumulative effect for geometries with rotational symmetries as the number of layers around cladding increases. The effect of placing an extra track around the cladding region of a MS WG with optimised parameters

of FS geometry has been shown in Fig. 6.9(b) at 1.55 μm wavelength. The birefringence is calculated by: $(n_O^{\text{eff}} - n_O) - (n_E^{\text{eff}} - n_E)$. An additional birefringence occurs with each track positioned, however it averages out while the total number of tracks is increased from 120 to 220 around the core center.

6.5 Summary

The design of spiral geometries for MS WGs in $LiNbO_3$ have numerically been studied by using FEM. Specifically, design procedures for MS WGs with ES, FS and AS geometries have been explored by taking into account the experimentally achieved track parameters. Additionally, an optimisation procedure is applied based on obtaining the lowest confinement losses at 3 μm wavelength by using a similar number of tracks in the cladding region and similar sizes of core regions. MS WGs with optimised parameters of spiral geometries and of hexagonal geometry have been compared between each other in terms of confinement loss, effective area, dispersion and birefringence. In the light of obtained results, it has been shown that the design of a MS WG with FS geometry can extend the maximum operation wavelength of 1 dB/cm confinement loss to around 3.66 μm. It has also been shown that each spiral geometry has different specific properties, which can be proper to use for different photonic applications. Positioning errors of tracks during fabrication process have numerically been evaluated, and shown that a MS WG with FS geometry provides more stable propagation properties compared to MS WGs with other geometries.

Chapter 7

Conclusions

In this chapter, a brief summary of topics covered in the previous chapters will be given, and a quick look towards future about how this work could be furthered in light of what has been done will be presented.

In chapter 2, approaches to the modelling of MS WGs in anisotropic crystals hve been presented. First, a theoretical analysis of light propagation in anisotropic crystals has been given in terms of full-vectorial Maxwell equations. Any analytical solution to the equations for the propagation of light could not have been obtained due to the couplings of polarised light components in inhomogeneous MS WGs with anisotropic crystals. Therefore, numerical methods which can cope with full-vectorial Maxwell equations in complex materials have been investigated. The FEM has generally been used for the modal analysis of those MS WGs during this work, and thus, the FEM and PWM have been described in detail. The accuracy of calculations has been validated by making a comparison work on the results of previously reported MOFs.

In chapter 3, the direct fs laser inscription method in $LiNbO_3$ has been introduced.

Experimentally obtained results regarding to WG properties in $LiNbO_3$ has been given. Those results has constituted the bases for the study on this thesis.

In chapter 4, the design of depressed-cladding MS WGs in $LiNbO_3$ has numerically been investigated. First, a methodology to design MS WGs in $LiNbO_3$ has been introduced by using an hexagonal geometry. The presented approach exploited the parameter space such as track size, spacing, number of rings, and RI contrasts, that is accessible experimentally. It appeared from this work that the relatively moderate RI contrasts which can be achievable by current fs micro-fabrication technology and geometric WG parameters have relatively little control over the dispersion properties of the MS WGs. On the other hand, the number of rings have played a major role in the control of the confinement losses. Increasing the number of rings from two to seven for the typical induced RI contrast -0.01 has resulted in an extension of the spectral range where the confinement losses are below 1 dB/cm to the wavelengths near 2 μm, and in a reduction of the losses by more than three orders of magnitude at the telecommunication wavelength $\lambda = 1.55$ μm.

In chapter 5, a practical approach for the optimisation of guiding properties of depressed-cladding MS WGs in z-cut $LiNbO_3$ has been presented. First, the optimisation geometry of a MS WG in z-cut $LiNbO_3$ has been introduced. An optimisation procedure has been applied to find the lowest confinement losses at 3 μm wavelength by taking in to account the experimentally achieved track properties. It has been shown that the spectral region where the confinement losses are below 1 dB/cm can extend up to a wavelength of 3.5 μm for optimised, hexagonal WG structures with seven rings of tracks, thereby making such structures suitable for mid-IR applications.

In chapter 6, advanced WG geometries have been explored to design MS WGs in z-cut $LiNbO_3$. First, the design procedures for MS WGs with Equiangular, Fermat and Archimedes

spiral geometries have been given in terms of corresponding mathematical representations and of experimentally obtained track sizes. Then, an optimisation procedure has been applied to find the lowest confinement loss at 3 μm of wavelength based on using similar sizes of core regions and similar number of tracks in the cladding regions. Finally, propagation properties of optimised MS WGs with those spiral geometries and the MS WG with hexagonal geometry have been compared between each other. It has been shown that MS WGs with Fermat spiral geometry can extend the operation wavelength of maximum 1 dB/cm confinement loss to around 3.66 μm.

7.1 Future Work

Direct fs laser incription method is a newly emerging, but an enabling technology to achieve many appealing applications and to build highly complex high performance IOC devices in a small footprint. It is clear that the range of packing geometries and parameters that can be investigated are far from being fully explored at present. A future work should be in the direction of establishing new inscription processes and regimes for the direct fs laser inscription of crystals with controllable properties of material modifications beyond the limits by current technology. New inscription processes and regimes could be optimised in a controllable and generalisable manner by a prior modelling of hierarchical physical effects. Major limitations are the unavailability of the precise understan- ding of the underlying physical effects leading to material modifications, the unavailability of physical parameters and material constants, and the computational inefficiency of commercial softwares to handle a huge space of parameters coming into play at different stages of material modifications. So, it is a further future work to develop efficient analytic and numerical tools which can able to

solve the optimisation problem for generalisable MS WGs.

$LiNbO_3$ is one of the most ideal materials to realise a vast majority of both linear and nonlinear optical applications in a single platform. Curved and straight WGs constitute the basic blocks of IOCs. To give just an example, it is possible to design various devices relying on the coupling properties between closely spaced multiple WGs. It would be further research work to study and optimise the coupling properties of MS WGs. To make a step further towards building IOC devices, a future work should also be considered in the direction of modelling the propagation properties of light and optimising the bending losses in curved WGs. It is not possible to mention all of the application areas of $LiNbO_3$ as a future work, since each of which operates on specific device requirements. The propagation properties of light over the WG region of any specific linear or nonlinear device application need to be adjusted to optimise the output properties of optical devices in $LiNbO_3$.

References

[1] M.L. Calvo and V. Lakshminarayanan, *Optical Waveguides: From Theory to Applied Technologies*, CRC Press, Baton Rouge, US, January 2007.

[2] K. Okamoto, *Fundamentals of Optical Waveguides*, Elsevier Science, 2010.

[3] T. Suhara and M. Fujimura, *Waveguide Nonlinear-Optic Devices*, Springer, 2003.

[4] G. Lifante, *Integrated Photonics: Fundamentals*, Wiley, 2003.

[5] K. K. Wong, *Properties of Lithium Niobate*, Institution of Engineering and Technology, 2002.

[6] M. Lawrence, "Lithium niobate integrated optics", *Reports on Progress in Physics*, vol. 56, no. 3, pp. 363, 1993.

[7] L. Arizmendi, "Photonic applications of lithium niobate crystals", *Physica Status Solidi (a)*, vol. 201, no. 2, pp. 253–283, 2004.

[8] G. J. Griffiths and R. J. Esdaile, "Analysis of titanium diffused planar optical waveguides in lithium niobate", *IEEE Journal of Quantum Electronics*, vol. 20, no. 2, pp. 149–159, 1984.

[9] K. Sugii, M. Fukuma, and H. Iwasaki, "A study on titanium diffusion into $LiNbO_3$ waveguides by electron probe analysis and X-ray diffraction methods", *Journal of Materials Science*, vol. 13, no. 3, pp. 523–533, 1978.

[10] M. N. Armenise, C. Canali, M. De Sario, A. Carnera, P. Mazzoldi, and G. Celotti, "Ti compound formation during ti diffusion in $LiNbO_3$", *IEEE Transactions on Components, Hybrids, and Manufacturing Technology*, vol. 5, no. 2, pp. 212–216, 1982.

[11] J. L. Jackel, C. E. Rice, and J. J. Veselka, "Proton exchange for high index waveguides in $LiNbO_3$", *Applied Physics Letters*, 1982.

[12] Y. N. Korkishko and V. A. Fedorov, *Ion Exchange in Single Crystals for Integrated Optics and Optoelectronics*, Canmbridge International Science, 1999.

[13] X. F. Chen, Q. Li, S. W. Xie, Y. X. Xia, Y. L. Chen, S. Sottini, E. Giorgetti, A. Carta, R. Ramponi, R. Osellame, and M. Marangoni, "Fabrication and characterization of proton-exchanged lithium niobate", in *Frontiers of Laser Physics and Quantum*

Optics: Proceedings of the International Conference on Laser Physics and Quantum Optics, Zhizhan Xu, Shengwu Xie, Shi-Yao Zhu, and Marlan Orvil Scully, Eds. 2000, pp. 443–448, Springer Berlin Heidelberg.

[14] P. D. Townsend, "Ion implantation and integrated optics", *Journal of Physics E: Scientific Instruments*, vol. 10, no. 3, pp. 197–203, 1977.

[15] O. Pena-Rodriguez, J. Olivares, M. Carrascosa, A. Garcia-Cabanes, A. Rivera, and F. Agullo-Lopez, "Optical waveguides fabricated by ion implantation/irradiation: A review", in *Ion Implantation, Prof. Mark Goorsky*. 2012, InTech.

[16] C. Buchal, S. P. Withrow, C. W. White, and D. B. Poker, "Ion implantation of optical materials", *Annual Review of Materials Science*, vol. 24, no. 1, pp. 125–158, 1994.

[17] F. Chen and K. Wang, X. Wang, "Development of ion-implanted optical waveguides in optical materials: A review", *Optical Materials*, vol. 29, no. 11, pp. 1523 – 1542, 2007.

[18] R. Osellame, S. Taccheo, M. Marangoni, R. Ramponi, P. Laporta, D. Polli, S. D. Silvestri, and G. Cerullo, "Femtosecond writing of active optical waveguides with astigmatically shaped beams", *Journal of the Optical Society of America B: Optical Physics*, vol. 20, no. 7, pp. 1559–1567, 2003.

[19] K. M. Davis, K. Miura, N. Sugimoto, and K. Hirao, "Writing waveguides in glass with a femtosecond laser", *Optics Letters*, vol. 21, no. 21, pp. 1729–1731, 1996.

[20] T. Allsop, M. Dubov, V. Mezentsev, and I. Bennion, "Inscription and characterization of waveguides written into borosilicate glass by a high-repetition-rate femtosecond laser at 800 nm", *Applied Optics*, vol. 49, no. 10, pp. 1938–1950, April 2010.

[21] V. R. Bhardwaj, E. Simova, P. B. Corkum, D. M. Rayner, C. Hnatovsky, R. S. Taylor, B. Schreder, M. Kluge, and J. Zimmer, "Femtosecond laser-induced refractive index modification in multicomponent glasses", *Journal of Applied Physics*, vol. 97, no. 8, pp. 083102–1–083102–9, 2005.

[22] A. Stefani, M. Stecher, G. E. Town, and O. Bang, "Direct Writing of Fiber Bragg Grating in Microstructured Polymer Optical Fiber", *Photonic Technology Letters*, vol. 24, no. 13, pp. 1148–1150, July 2012.

[23] A. Rodenas, G. A. Torchia, G. Lifante, E. Cantelar, J. Lamela, F. Jaque, L. Roso, and D. Jaque, "Refractive index change mechanisms in femtosecond laser written ceramic Nd:YAG waveguides: micro-spectroscopy experiments and beam propagation calculations", *Applied Physics B-Lasers and Optics*, vol. 95, no. 1, pp. 85–96, April 2009.

[24] M. V. Dubov, L. Krushchev, I. Bennion, A. G. Okhrimchuk, and A. V. Shestakov, "Waveguide inscription in YAG:Cr^{4+} crystals by femtosecond laser irradiation", in *Conference on Lasers and Electro-Optics/International Quantum Electronics Conference and Photonic Applications Systems Technologies*, San Francisco, California United States, 2004, p. CWA49.

[25] A. G. Okhrimchuk, V. K. Mezentsev, H. Schmitz, M. Dubov, and I. Bennion, "Cascaded nonlinear absorption of femtosecond laser pulses in dielectrics", *Laser Physics*, vol. 19, no. 7, pp. 1415–1422, 2009.

[26] S. Nolte, M. Will, J. Burghoff, and A. Tünnermann, "Femtosecond waveguide writing: A new avenue to three-dimensional integrated optics", *Applied Physics A: Materials Science and Processing*, vol. 77, no. 1, pp. 109–111, 2003.

[27] W. Horn, S. Kroesen, J. Herrmann, J. Imbrock, and C. Denz, "Electro-optical tunable waveguide bragg gratings in lithium niobate induced by femtosecond laser writing", *Optics Express*, vol. 20, no. 24, pp. 26922–26928, November 2012.

[28] J. Thomas, M. Heinrich, P. Zeil, V. Hilbert, K. Rademaker, R. Riedel, S. Ringleb, C. Dubs, J. P. Ruske, S. Nolte, and A. Tünnermann, "Laser direct writing: Enabling monolithic and hybrid integrated solutions on the lithium niobate platform", *Physica Status Solidi (A)*, vol. 208, no. 2, pp. 276–283, 2011.

[29] J. Burghoff, S. Nolte, and A. Tünnermann, "Origins of waveguiding in femtosecond laser-structured $LiNbO_3$", *Applied Physics A*, vol. 89, no. 1, pp. 127–132, 2007.

[30] L. Gui, B. Xu, and T. C. Chong, "Microstructure in lithium niobate by use of focused femtosecond laser pulses", *IEEE Photonics Technology Letters*, vol. 16, no. 5, pp. 1337–1339, May 2004.

[31] L. Gui, B. X. Xu, D. J. Wu, Y. W. Goh, and T. C. Chong, "Refractive index change in lithium niobate induced by focused femtosecond laser", in *Integrated Optics: Devices, Materials, and Technologies VIII*, Y. Sidorin and A. Tervonen, Eds., vol. 5355 of *Proceedings of SPIE*, pp. 22–32. 2004.

[32] R. R. Thomson, S. Campbell, I. J. Blewett, A. K. Kar, and D. T. Reid, "Optical waveguide fabrication in z-cut lithium niobate ($LiNbO_3$) using femtosecond pulses in the low repetition rate regime", *Applied Physics Letters*, vol. 88, no. 11, 2006.

[33] Y. L. Lee, N. E. Yu, C. Jung, B. A. Yu, I. B. Sohn, S. C. Choi, Y. C. Noh, D. K. Ko, W. S. Yang, H. M. Lee, W. K. Kim, and H. Y. Lee, "Second-harmonic generation in periodically poled lithium niobate waveguides fabricated by femtosecond laser pulses", *Applied Physics Letters*, vol. 89, no. 17, October 2006.

[34] A. H. Nejadmalayeri and P. R. Herman, "Ultrafast laser waveguide writing: lithium niobate and the role of circular polarization and picosecond pulse width", *Optics Letters*, vol. 31, no. 20, pp. 2987–2989, October 2006.

[35] J. Burghoff, C. Grebing, S. Nolte, and A. Tünnermann, "Efficient frequency doubling in femtosecond laser-written waveguides in lithium niobate", *Applied Physics Letters*, vol. 89, no. 8, 2006.

[36] J. Burghoff, H. Hartung, S. Nolte, and A. Tünnermann, "Optical and structural properties of waveguides in $LiNbO_3$ fabricated by ultrashort laser pulses", San Jose, California, USA, 21 - 24 January 2007, "Commercial and Biomedical Applications of Ultrafast Lasers" Conference, vol. 6460, pp. 64600W–64600W–10.

[37] A. G. Okhrimchuk, A. V. Shestakov, I. Khrushchev, and J. Mitchell, "Depressed cladding, buried waveguide laser formed in a YAG:Nd^{3+} crystal by femtosecond laser writing", *Optics Letters*, vol. 30, no. 17, pp. 2248–2250, September 2005.

[38] E. Yablonovitch, "Inhibited spontaneous emission in solid-state physics and electronics", *Physical Review Letters*, vol. 58, no. 20, pp. 2059–2062, May 1987.

[39] J. D. Joannopoulos, S. G. Johnson, J. N. Winn, and R. D. Meade, *Photonic Crystals: Molding the Flow of Light*, Princeton University Press, 2011.

[40] P. S. J. Russell, "Photonic-crystal fibers", *Journal of Lightwave technology*, vol. 24, no. 12, pp. 4729–4749, December 2006.

[41] R. Buczynski, "Photonic crystal fibers", *Acta Physica Polonica Series A*, vol. 106, no. 2, pp. 141–168, August 2004.

[42] J. Thomas, M. Heinrich, J. Burghoff, S. Nolte, A. Ancona, and A. Tünnermann, "Femtosecond laser-written quasi-phase-matched waveguides in lithium niobate", *Applied Physics Letters*, vol. 91, no. 15, October 2007.

[43] A. Okhrimchuk, V. Mezentsev, A. Shestakov, and I. Bennion, "Low loss depressed cladding waveguide inscribed in YAG:Nd single crystal by femtosecond laser pulses", *Optics Express*, vol. 20, no. 4, pp. 3832–3843, 2012.

[44] R. He, Q. An, Y. Jia, G. R. Castillo-Vega, J. R. V. Aldana, and F. Chen, "Femtosecond laser micromachining of lithium niobate depressed cladding waveguides", *Optical Materials Express*, vol. 3, no. 9, pp. 1378–1384, September 2013.

[45] M. Dubov, S. Boscolo, and D. Webb, "Microstructured waveguides in z-cut $LiNbO_3$ by high repetition rate direct femtosecond laser inscription", *Optical Materials Express*, vol. 4, no. 8, pp. 1708–1716, August 2014.

[46] P. Yeh, *Optical Waves in Layered Media*, Wiley, 2005.

[47] A. Yariv and P. Yeh, *Optical waves in crystals: propagation and control of laser radiation*, Wiley, 1984.

[48] H. Karakuzu, M. Dubov, S. Boscolo, L. Mel'nikov, and Y. Mazhirina, "Control of the properties of micro-structured waveguides in lithium niobate crystals", in *Advanced Solid-State Lasers Congress*. 2013, p. JTh2A.22, Optical Society of America.

[49] G.P. Agrawal, *Nonlinear fiber optics*, Academic Press, San Diego, CA, 1989.

[50] J. M. Jin, *The Finite Element Method in Electromagnetics*, Wiley, 1993.

[51] S. G. Johnson and J. D. Joannopoulos, "Block-iterative frequency-domain methods for Maxwell's equations in a planewave basis", *Optics Express*, vol. 8, no. 3, pp. 173–190, January 2001.

[52] J. Shibayama, J. Yamauchi, and H. Nakano, "Application of the finite-difference beam-propagation method to optical waveguide analysis", in *17th International Conference on Applied Electromagnetics and Communications, ICECom 2003*, October 2003, pp. 262–265.

[53] G. Lifante, F. Cusso, and E. Cantelar, "Numerical methods for optical waveguide devices", in *Mathematical Methods in Electromagnetic Theory, 2006 International Conference on*, 2006, pp. 77–82.

[54] B. M. A. Rahman and A. Agrawal, *Finite Element Modeling Methods for Photonics*, Artech House, 2013.

[55] Z. Zhu and T. G. Brown, "Full-vectorial finite-difference analysis of microstructured optical fibers", *Optics Express*, vol. 10, no. 17, pp. 853–864, August 2002.

[56] K. A. Rutkowska and L. W. Wei, "Full-vectorial description of the light guidance in anisotropic photonic liquid crystal fibers", *Acta Physica Polonica A*, vol. 122, no. 5, pp. 880–890, 2012.

[57] N. Schulz, K. Bierwirth, F. Arndt, and U. Koster, "Finite-difference method without spurious solutions for the hybrid-mode analysis of diffused channel waveguides", *IEEE Transactions on Microwave Theory and Techniques*, vol. 38, no. 6, pp. 722–729, June 1990.

[58] J. Arriaga, J. C. Knight, and P. S. J. Russell, "Modelling photonic crystal fibres", *Physica E: Low-dimensional Systems and Nanostructures*, vol. 17, pp. 440 – 442, 2003.

[59] K. M. Leung and Y. F. Liu, "Photon band structures: The plane-wave method", *Physical Review B*, vol. 41, no. 14, pp. 10188–10190, May 1990.

[60] H. S. Sozuer, J. W. Haus, and R. Inguva, "Photonic bands: Convergence problems with the plane-wave method", *Physical Review B*, vol. 45, no. 24, pp. 13962–13972, June 1992.

[61] M. Lu and M. M. Fejer, "Anisotropic dielectric waveguides", *Journal of Optical Society of America A*, vol. 10, no. 2, pp. 246–261, February 1993.

[62] I. A. Khromova and L. A. Mel'nikov, "Anisotropic photonic crystals: Generalized plane wave method and dispersion symmetry properties", *Optics Communications*, vol. 281, no. 21, pp. 5458–5466, November 2008.

[63] Y. A. Mazhirina and L. A. Mel'nikov, "On the structure of waveguiding regions for high-order core modes of solid-core photonic-crystal fibers", *Optics and Spectroscopy*, vol. 107, no. 3, pp. 454–459, 2009.

[64] Y. A. Mazhirina and L. A. Mel'nikov, "Numerical modelling of waveguiding properties of solid core photonic crystal fibers", *AIP Conference Proceedings*, vol. 1291, pp. 136–138, 2010.

[65] N. Engheta, W. D. Murphy, V. Rokhlin, and M. S. Vassiliou, "The fast multipole method (FMM) for electromagnetic scattering problems", *IEEE Transactions on Antennas and Propagation*, vol. 40, no. 6, pp. 634–641, June 1992.

[66] T. P. White, B. T. Kuhlmey, R. C. McPhedran, D. Maystre, G. Renversez, C. M. Sterke, and L. C. Botten, "Multipole method for microstructured optical fibers. I. formulation", *Journal of Optical Society of America B*, vol. 19, no. 10, pp. 2322–2330, October 2002.

[67] B. T. Kuhlmey, T. P. White, G. Renversez, D. Maystre, L. C. Botten, C. M. Sterke, and R. C. McPhedran, "Multipole method for microstructured optical fibers. II. implementation and results", *Optical Society of America B*, vol. 19, no. 10, pp. 2331–2340, October 2002.

[68] D. G. Popescu and P. Sterian, "Photonic crystal fiber mode characterization with multipole method", *University Politehnica of Bucharest Scientific Bulletin, Series A*, vol. 75, no. 2, pp. 205–215, 2013.

[69] T. P. White, R. C. McPhedran, L. C. Botten, G. H. Smith, and C. M. Sterke, "Calculations of air-guided modes in photonic crystal fibers using the multipole method", *Optics Express*, vol. 9, no. 13, pp. 721–732, December 2001.

[70] O. C. Zienkiewicz, *The finite element method in engineering science*, McGraw-Hill, 1971.

[71] K. Saitoh and M. Koshiba, "Numerical modeling of photonic crystal fibers", *Journal of Lightwave Technology*, vol. 23, no. 11, pp. 3580–3590, November 2005.

[72] L. A. Mel'nikov, Y. S. Skibina, P. Glas, D. Fischer, N. B. Skibina, V. I. Beloglazov, and R. Wedell, "Glass and metal-glass holey fibers with high quality hexagonal structure", in *Conference on Lasers & Electro-Optics Europe (CLEO/Europe)*, June 2003, pp. 609–.

[73] O. C. Zienkiewicz, *The Finite Element Method*, McGraw-Hill, London, England, 3rd edition, 1977.

[74] P. Silvester and R. L. Ferrari, *Finite Elements for Electrical Engineers*, Cambridge Press, 2nd edition, 1990.

[75] J. N. Reddy, *An Introduction to the Finite Element Method*, McGraw-Hill, New York, 1st edition, 1984.

[76] D. Welt and J. Webb, "Finite-element analysis of dielectric waveguides with curved boundaries", *IEEE Transactions on Microwave Theory and Techniques*, vol. 33, no. 7, pp. 576–585, July 1985.

[77] B. M. A. Rahman and J. B. Davies, "Penalty function improvement of waveguide solution by finite elements", *IEEE Transactions on Microwave Theory and Techniques*, vol. 32, no. 8, pp. 922–928, August 1984.

[78] H. Whitney, *Geometric Integration Theory*, Princeton University Press, 1957.

[79] A. Bossavit, "Simplicial finite elements for scattering problems in electromagnetism", *Computer Methods in Applied Mechanics and Engineering*, vol. 76, no. 3, pp. 299 – 316, 1989.

[80] R. F. Harrington, *Field Computation by Moment Methods*, R. E. Krieger Publishing Company, Florida, 1968.

[81] J. F. Lee, D. K. Sun, and Z. J. Cendes, "Full-wave analysis of dielectric waveguides using tangential vector finite elements", *IEEE Transactions on Microwave Theory and Techniques*, vol. 39, no. 8, pp. 1262–1271, August 1991.

[82] B. Engquist and A. Majda, "Absorbing boundary conditions for the numerical simulation of waves", *Mathematics of Computation*, vol. 31, no. 139, pp. 629–651, 1977.

[83] A. Taflove and S. C. Hagness, *Computational Electrodynamics: The Finite-difference Time-domain Method*, Artech House, 2 edition, 2000.

[84] J. P. Berenger, "A perfectly matched layer for the absorption of electromagnetic waves", *Journal of Computational Physics*, vol. 114, no. 2, pp. 185 – 200, 1994.

[85] Z. S. Sacks, D. M. Kingsland, R. Lee, and J. F. Lee, "A perfectly matched anisotropic absorber for use as an absorbing boundary condition", *IEEE Transactions on Antennas and Propagation*, vol. 43, no. 12, pp. 1460–1463, December 1995.

[86] W. C. Chew and W. H. Weedon, "A 3D Perfectly Matched Medium from modified Maxwell's equations with stretched coordinates", *Microwave and Optical Technology Letters*, vol. 7, no. 13, pp. 599–604, 1994.

[87] C. M. Rappaport, "Perfectly matched absorbing boundary conditions based on anisotropic lossy mapping of space", *IEEE Microwave Guided Wave Letters*, vol. 5, no. 3, pp. 90–92, March 1995.

[88] F. L. Teixeira and W. C. Chew, "General closed-form PML constitutive tensors to match arbitrary bianisotropic and dispersive linear media", *IEEE Microwave and Guided Wave Letters*, vol. 8, no. 6, pp. 223–225, June 1998.

[89] Y. Y. Botros and J. L. Volakis, "Detailed convergence study for perfectly matched layer PML applications", Naval Postgraduate School, Monterey, CA, 1998, 14th Applied Computational Electromagnetics Conference.

[90] Y. Tsuji and M. Koshiba, "Guided-Mode and Leaky-Mode Analysis by Imaginary Distance Beam Propagation Method Based on Finite Element Scheme", *Journal of Lightwave Technology*, vol. 18, no. 4, pp. 618, 2000.

[91] S. G. Johnson, P. Bienstman, M. A. Skorobogatiy, M. Ibanescu, E. Lidorikis, and J. D. Joannopoulos, "Adiabatic theorem and continuous coupled-mode theory for efficient taper transitions in photonic crystals", *Physical Review E*, vol. 66, pp. 066608, December 2002.

[92] A. F. Oskooi, L. Zhang, Y. Avniel, and S. G. Johnson, "The failure of perfectly matched layers, and towards their redemption by adiabatic absorbers", *Optics Express*, vol. 16, no. 15, pp. 11376–11392, July 2008.

[93] A. Oskooi and S. G. Johnson, "Distinguishing correct from incorrect PML proposals and a corrected unsplit PML for anisotropic, dispersive media", *Journal of Computational Physics*, vol. 230, no. 7, pp. 2369–2377, 2011.

[94] K. Saitoh and M. Koshiba, "Full-vectorial imaginary-distance beam propagation method based on a finite element scheme: application to photonic crystal fibers", *IEEE Journal of Quantum Electronics*, vol. 38, no. 7, pp. 927–933, July 2002.

[95] P. Viale, S. Fevrier, F. Gerome, and H. Vilard, "Confinement loss computations in photonic crystal fibres using a novel perfectly matched layer design", *Proceedings of the COMSOL Multiphysics User's Conference 2005 Paris*, vol. 10, no. 17, pp. 853–864, August 2005.

[96] K. Saitoh and M. Koshiba, "Highly nonlinear dispersion-flattened photonic crystal fibers for supercontinuum generation in a telecommunication window", *Optics Express*, vol. 12, no. 10, pp. 2027–2032, May 2004.

[97] R. Osellame, G. Cerullo, and R. Ramponi, *Femtosecond Laser Micromachining: Photonic and Microfluidic Devices in Transparent Materials*, Springer, 2012.

[98] M. Dubov, *Direct femtosecond laser inscription in transparent dielectrics*, PhD thesis, Aston University, 2011.

[99] K. Miura, J. Qiu, H. Inouye, T. Mitsuyu, and K. Hirao, "Photowritten optical waveguides in various glasses with ultrashort pulse laser", *Applied Physics Letters*, vol. 71, no. 23, pp. 3329–3331, 1997.

[100] O. M. Efimov, L. B. Glebov, K.A. Richardson, E. V. Stryland, T. Cardinal, S. H. Park, M. Couzi, and J. L. Bruneel, "Waveguide writing in chalcogenide glasses by a train of femtosecond laser pulses", *Optical Materials*, vol. 17, no. 3, pp. 379 – 386, 2001.

[101] B. Zhu, Y. Dai, H. Ma, S. Zhang, and J. Qiu, "Direct writing Eu^{3+}-doped $Ba_2TiSi_2O_8$ crystalline pattern by femtosecond laser irradiation", *Journal of Alloys and Compounds*, vol. 460, no. 1–2, pp. 590–593, July 2008.

[102] C. N. Borca, V. Apostolopoulos, F. Gardillou, H. G. Limberger, M. Pollnau, and R. P. Salathe, "Buried channel waveguides in Yb-doped $KY(WO_4)_2$ crystals fabricated by femtosecond laser irradiation", *Applied Surface Science*, vol. 253, no. 19, pp. 8300–8303, July 2007.

[103] I. Bennion, M. Dubov, I. Khrushchev, and J. Mitchell, "Laser inscription of optical structures in crystals", June 2005, WO Patent App. PCT/GB2004/004,334.

[104] F. Chen and J. R. V. Aldana, "Optical waveguides in crystalline dielectric materials produced by femtosecond-laser micromachining", *Laser & Photonics Reviews*, vol. 8, no. 2, pp. 251–275, 2014.

[105] N. D. Psaila, R. R. Thomson, H. T. Bookey, A. K. Kar, N. Chiodo, R. Osellame, G. Cerullo, A. Jha, and S. Shen, "Er:Yb-doped oxyfluoride silicate glass waveguide amplifier fabricated using femtosecond laser inscription", *Applied Physics Letters*, vol. 90, no. 13, 2007.

[106] G. D. Valle, S. Taccheo, R. Osellame, A. Festa, G. Cerullo, and P. Laporta, "1.5 μm single longitudinal mode waveguide laser fabricated by femtosecond laser writing", *Optics Express*, vol. 15, no. 6, pp. 3190–3194, 2007.

[107] A. M. Streltsov and N. F. Borrelli, "Fabrication and analysis of a directional coupler written in glass by nanojoule femtosecond laser pulses", *Optics Letters*, vol. 26, no. 1, pp. 42–43, January 2001.

[108] J. Liu, Z. Zhang, S. Chang, C. Flueraru, and C. P. Grover, "Directly writing of 1-to-N optical waveguide power splitters in fused silica glass using a femtosecond laser", *Optics Communications*, vol. 253, no. 4-6, pp. 315–319, 2005.

[109] A. Martinez, M. Dubov, I. Khrushchev, and I. Bennion, "Direct writing of fibre bragg gratings by femtosecond laser", *Electronics Letters*, vol. 40, no. 19, pp. 1170–1172, September 2004.

[110] W. Cai, A. R. Libertun, and R. Piestun, "Polarization selective computer-generated holograms realized in glass by femtosecond laser induced nanogratings", *Optics Express*, vol. 14, no. 9, pp. 3785–3791, 2006.

[111] S. S. Mao, F. Quere, S. Guizard, X. Mao, R. E. Russo, G. Petite, and P. Martin, "Dynamics of femtosecond laser interactions with dielectrics", *Appl. Phys. A*, vol. 79, pp. 1695–1709, 2004.

[112] V. Mezentsev, J. Petrovic, M. Dubov, I. Bennion, J. Dreher, H. Schmitz, and R. Grauer, "Femtosecond laser microfabrication of subwavelength structures in photonics", *Proceedings of SPIE*, vol. 6459, pp. 64590B–64590B–11, 2007.

[113] R. R. Gattass and E. Mazur, "Femtosecond laser micromachining in transparent materials", *Nature Photonics*, vol. 2, no. 4, pp. 219–225, 2008.

[114] G. D. Valle, R. Osellame, and P. Laporta, "Micromachining of photonic devices by femtosecond laser pulses", *Journal of Optics A: Pure and Applied Optics*, vol. 11, no. 1, 2009.

[115] V. Mezentsev, M. Dubov, J. Petrovic, I. Bennion, J. Dreher, and R. Grauer, "Role of plasma in femtosecond laser pulse propagation", *AIP Conference Proceedings*, vol. 876, no. 1, pp. 169–180, 2006.

[116] A. M. Streltsov, "Femtosecond-laser writing of tracks with depressed refractive index in crystals", 2003, vol. 4941, pp. 51–57.

[117] N. Dong, F. Chen, and J. R. V. Aldana, "Efficient second harmonic generation by birefringent phase matching in femtosecond-laser-inscribed KTP cladding waveguides", *Physica Status Solidi (RRL) - Rapid Research Letters*, vol. 6, no. 7, pp. 306–308, 2012.

[118] J. Hu and C. R. Menyuk, "Understanding leaky modes: slab waveguides revisited", *Advances in Optics and Photonics*, vol. 1, no. 1, pp. 58–106, January 2009.

[119] A. H. Nejadmalayeri and P. R. Herman, "Rapid thermal annealing in high repetition rate ultrafast laser waveguide writing in lithium niobate", *Optics Express*, vol. 15, no. 17, pp. 10842–10854, August 2007.

[120] S. M. Eaton, M. L. Ng, J. Bonse, A. Mermillod-Blondin, H. Zhang, A. Rosenfeld, and P. R. Herman, "Low-loss waveguides fabricated in BK7 glass by high repetition rate femtosecond fiber laser", *Applied Optics*, vol. 47, no. 12, pp. 2098–2102, April 2008.

[121] S. M. Eaton, H. Zhang, M. L. Ng, J. Li, W. J. Chen, S. Ho, and P. R. Herman, "Transition from thermal diffusion to heat accumulation in high repetition rate femtosecond laser writing", *Optics Express*, vol. 16, no. 13, pp. 9443–9458, June 2008.

[122] S. Gross, M. Ams, D. G. Lancaster, T. M. Monro, A. Fuerbach, and M. J. Withford, "Femtosecond direct-write überstructure waveguide bragg gratings in ZBLAN", *Optics Letters*, vol. 37, no. 19, pp. 3999–4001, October 2012.

[123] S. Gross, M. Alberich, A. Arriola, M. J. Withford, and A. Fuerbach, "Fabrication of fully integrated antiresonant reflecting optical waveguides using the femtosecond laser direct-write technique", *Optics Letters*, vol. 38, no. 11, pp. 1872–1874, June 2013.

[124] R. R. Thomson, S. Campbell, G. Brown, I. J. Blewett, A. K. Kar, and D. T. Reid, "Femtosecond waveguide fabrication in bulk lithium niobate ($LiNbO_3$)", in *Conference on Lasers and Electro-Optics/Quantum Electronics and Laser Science and Photonic Applications Systems Technologies*. 2005, p. CThV5, Optical Society of America.

[125] J. Burghoff, H. Hartung, S. Nolte, and A. Tünnermann, "Structural properties of femtosecond laser-induced modifications in $LiNbO_3$", *Applied Physics A*, vol. 86, no. 2, pp. 165–170, 2007.

[126] J. Burghoff, C. Grebing, S. Nolte, and A. Tünnermann, "Waveguides in lithium niobate fabricated by focused ultrashort laser pulses", *Applied Surface Science*, vol. 253, no. 19, pp. 7899–7902, 2007.

[127] Z. Huang, C. Tu, S. Zhang, Y. Li, F. Lu, Y. Fan, and E. Li, "Femtosecond second-harmonic generation in periodically poled lithium niobate waveguides written by femtosecond laser pulses", *Optics Letters*, vol. 35, no. 6, pp. 877–879, 2010.

[128] R. Osellame, N. Chiodo, M. Lobino, M. Marangoni, G. Cerullo, R. Ramponi, H. T. Bookey, R. R. Thomson, N. Psaila, and A. K. Kar, "Efficient second harmonic generation in femtosecond laser written optical waveguides on periodically poled lithium niobate", 2008, vol. 6881.

[129] A. Fernandez, T. Fuji, A. Poppe, A. Furbach, F. Krausz, and A. Apolonski, "Chirped pulse oscillators: a route to high-power femtosecond pulses without external amplification", *Optics Letters*, vol. 29, no. 12, pp. 1366–1368, June 2004.

[130] A. V. Turchin, M. Dubov, and J. A. R. Williams, "3D reconstruction of the complex dielectric function of glass during femtosecond laser micro-fabrication", *Optical and Quantum Electronics*, vol. 42, no. 14-15, pp. 873–886, 2011.

[131] B. P. Cumming, A. Jesacher, M. J. Booth, T. Wilson, and M. Gu, "Adaptive aberration compensation for three-dimensional micro-fabrication of photonic crystals in lithium niobate", *Optics Express*, vol. 19, no. 10, pp. 9419–9425, May 2011.

[132] A. Roberts, E. Ampem-Lassen, A. Barty, K. Nugent, G. Baxter, N. Dragomir, and S. Huntington, "Refractive index profiling of optical fibers with axial symmetry by use of quantitative phase microscopy", *Optics Letters*, vol. 27, no. 23, pp. 2061–2063, December 2002.

[133] K. A. Nugent, "Wave field determination using three-dimensional intensity information", *Physical Review Letters*, vol. 68, pp. 2261–2264, April 1992.

[134] A. Barty, K. A. Nugent, D. Paganin, and A. Roberts, "Quantitative optical phase microscopy", *Optics Letters*, vol. 23, no. 11, pp. 817–819, June 1998.

[135] E. Ampem-Lassen, S. Huntington, N. Dragomir, K. Nugent, and A. Roberts, "Refractive index profiling of axially symmetric optical fibers: a new technique", *Optics Express*, vol. 13, no. 9, pp. 3277–3282, May 2005.

[136] R. S. Weis and T. K. Gaylord, "Lithium niobate: Summary of physical properties and crystal structure", *Applied Physics A*, vol. 37, pp. 191–203, March 1985.

[137] J. A. Armstrong, N. Bloembergen, J. Ducuing, and P. S. Pershan, "Interactions between light waves in a nonlinear dielectric", *Physical Review*, vol. 127, no. 6, pp. 1918–1939, Sep 1962.

[138] H. Karakuzu, M. Dubov, and S. Boscolo, "Control of the properties of micro-structured waveguides in lithium niobate crystal", *Optics Express*, vol. 21, no. 14, pp. 17122–17130, 2013.

[139] I. Khrushchev, A. G. Okhrimchuck, A. V. Shestakov, M. Dubov, and I. Bennion, "Laser inscribed structures", Patent WO 2005111677, 2005.

[140] Q. An, Y. Ren, Y. Jia, J. R. V. Aldana, and Feng Chen, "Mid-infrared waveguides in zinc sulfide crystal", *Optical Material Express*, vol. 3, no. 4, pp. 466–471, April 2013.

[141] F. Zolla, G. Renversez, and A. Nicolet, *Foundations of Photonic Crystal Fibres*, Imperial College Press, 2012.

[142] T. P. White, R. C. McPhedran, C. M. De Sterke, L. C. Botten, and M. J. Steel, "Confinement losses in microstructured optical fibers", *Optics Letters*, vol. 26, no. 21, pp. 1660–1662, November 2001.

[143] G. Renversez, B. Kuhlmey, and R. McPhedran, "Dispersion management with microstructured optical fibers: ultraflattened chromatic dispersion with low losses", *Optics Letters*, vol. 28, no. 12, pp. 989–991, June 2003.

[144] L. Dong, W. Wong, and M. E. Fermann, "Single mode propagation in fibers and rods with large leakage channels", Patent US 2013/0089113 A1, 2013.

[145] D. E. Zelmon, D. L. Small, and D. Jundt, "Infrared corrected Sellmeier coefficients for congruently grown lithium niobate and 5 mol. % magnesium oxide-doped lithium niobate", *Optical Society of America B*, vol. 14, no. 12, pp. 3319–3322, December 1997.

[146] H. Karakuzu, M. Dubov, S. Boscolo, L. A. Mel'nikov, and Y. A. Mazhirina, "Optimisation of microstructured waveguides in z-cut $LiNbO_3$ crystals", *Optical Materials Express*, vol. 4, no. 3, pp. 541–552, 2014.

[147] V. Apostolopoulos, L. Laversenne, T. Colomb, C. Depeursinge, R. P. Salathe, M. Pollnau, R. Osellame, G. Cerullo, and P. Laporta, "Femtosecond-irradiation-induced refractive-index changes and channel waveguiding in bulk Ti^{3+}:Sapphire", *Applied Physics Letters*, vol. 85, no. 7, pp. 1122–1124, August 2004.

[148] A. Rodenas and A. K. Kar, "High-contrast step-index waveguides in borate nonlinear laser crystals by 3D laser writing", *Optics Express*, vol. 19, no. 18, pp. 17820–17833, August 2011.

[149] A. Bjarklev, J. Broeng, and A. S. Bjarklev, *Photonic Crystal Fibres*, Springer US, 2012.

[150] E. H. Lockwood, *A Book of Curves*, Cambridge University Press, 1961.

[151] T. A. Cook, *The Curves of Life: Being an Account of Spiral Formations and Their Application to Growth in Nature, to Science, and to Art : with Special Reference to the Manuscripts of Leonardo Da Vinci*, Dover Publications, 1979.

[152] I. Hargittai and C. A. Pickover, *Spiral Symmetry*, World Scientific, 1992.

[153] J. Dyson, "The equiangular spiral antenna", *IRE Transactions on Antennas and Propagation*, vol. 7, no. 2, pp. 181–187, April 1959.

[154] H. Wen, J. Yang, W. Zhang, and J. Zhang, "Optical resonant Archimedean spiral antennas", *Journal of Nanophotonics*, vol. 5, no. 1, pp. 053523–053523–7, 2011.

[155] M. Kneissl, G. D. Chern, M. Teepe, D. W. Treat, Z. H. Yang, R. K. Chang, and N. M. Johnson, "Spiral-shaped microdisk lasers", 2005, vol. 5738, pp. 225–228.

[156] E. E. Narimanov and V. A. Podolskiy, "Spiral whispering-gallery resonators", 2005, vol. 5708, pp. 222–229.

[157] C. Ciminelli, F. Dell'Olio, and M. N. Armenise, "High-Q spiral resonator for optical gyroscope applications: Numerical and experimental investigation", *IEEE Photonics Journal*, vol. 4, no. 5, pp. 1844–1854, October 2012.

[158] C. Lin, E. W. Jacobs, and J. S. Rodgers, "Spiral planar-waveguide Bragg gratings", 2009, vol. 7218, pp. 72180E–72180E–8.

[159] X. Zhang, P. Li, F. Fang, and Q. Wang, "Ultra-precision turning of complex spiral optical delay line", 2011, vol. 8202, pp. 82020N–82020N–8.

[160] I. N. M. Wijeratne, N. Kejalakshmy, A. Agrawal, B. M. A. Rahman, and K. T. V. Grattan, "Numerical analysis of second harmonic generation in soft glass equiangular spiral photonic crystal fibers", *IEEE Photonics Journal*, vol. 4, no. 2, pp. 357–368, April 2012.

[161] C. Gui and J. Wang, "Elliptical and spiral photonic crystal fibers with wideband high birefringence, large nonlinearity, and low dispersion", *Photonics Journal*, vol. 4, no. 6, pp. 2152–2158, December 2012.

[162] A. Agrawal, N. Kejalakshmy, B. M. A. Rahman, and K. T. V. Grattan, "Soft glass equiangular spiral photonic crystal fiber for supercontinuum generation", *IEEE Photonics Technology Letters*, vol. 21, no. 22, pp. 1722–1724, November 2009.

[163] A. Agrawal, M. Tiwari, Y. O. Azabi, V. Janyani, B. M. A. Rahman, and K. T. V. Grattan, "Ultrabroad supercontinuum generation in tellurite equiangular spiral photonic crystal fiber", *Journal of Modern Optics*, vol. 60, no. 12, pp. 956–962, 2013.

[164] M. I. Munteanu, "From golden spirals to constant slope surfaces", *Journal of Mathematical Physics*, vol. 51, no. 7, 2010.

[165] A. Agrawal, N. Kejalakshmy, M. Uthman, B. M. A. Rahman, A. Kumar, and K. T. V. Grattan, "Ultra low bending loss equiangular spiral photonic crystal fibers in the terahertz regime", *AIP Advances*, vol. 2, no. 2, 2012.

[166] A. Agrawal, Y. O. Azabi, and B. M. A. Rahman, "Stacking the Equiangular Spiral", *IEEE Photonics Technology Letters*, vol. 25, no. 3, pp. 291–294, February 2013.

[167] T. O. Omotehinwa and S. O. Ramon, "Fibonacci numbers and golden ratio in mathematics and science", *International Journal of Computer and Information Technology*, vol. 02, no. 04, pp. 630–638, July 2013.

[168] A. Agrawal, N. Kejalakshmy, J. Chen, B. M. A. Rahman, and K. T. V. Grattan, "Golden spiral photonic crystal fiber: polarization and dispersion properties", *Optics Letters*, vol. 33, no. 22, pp. 2716–2718, Nov 2008.

[169] A. Agrawal, N. Kejalakshmy, B. M. A. Rahman, and K. T. V. Grattan, "Polarization and dispersion properties of elliptical hole golden spiral photonic crystal fiber", *Applied Physics B*, vol. 99, no. 4, pp. 717–726, 2010.

*

Appendix A
Numerical computation

A.1 A Comsol - Matlab script to calculate the propagation modes of a MS WG

%An example of the Comsol- Matlab Script to calculate the propagation modes of MS %WGs in a material is given below. More details can be found on the web page of the program- www.comsol.com

```
clear all
% creating a model
model = ModelUtil.create('Model');
%A name can be set by
model.name('MS WG');
%Parameters are the wavelength of light (Lambda) [μm], track radius (radius) [μm], separation
%of tracks (pitch)[μm], RIs of material along polarization directions (no,ne), RI contrast (δn),
%PML length (L) [μm]. All of those parameters can be varied by creating a loop.
model.param.set('Lambda', '1');
model.param.set('no','(1+2.245*Lambda^2/(Lambda^2-0.012^2)+
1.3*Lambda^2/(Lambda^2-0.053^2)+6.897*Lambda^2/(Lambda^2-331.33^2))^0.5');
model.param.set('ne','(1+2.247*Lambda^2/(Lambda^2-0.0147^2)+
1.461*Lambda^2/(Lambda^2-0.056^2)+9.65*Lambda^2/(Lambda^2-371.2^2))^0.5');
model.param.set('delta_n', '0.01');
```

```
model.param.set('pitch', '2.5');
model.param.set('radius', '1');
model.param.set('claddingradius', '3*pitch');
model.param.set('L', '10');
model.param.set('pmlradius', 'claddingradius+L');
%Creating a 2D geometry node
model.modelNode.create('mod1');
%Create the geometry
model.geom.create('geom1', 2);
model.geom('geom1').lengthUnit([native2unicode(hex2dec('00b5'), 'Cp1252') 'm']);
%Track1
model.geom('geom1').feature.create('c3', 'Circle');
model.geom('geom1').feature('c3').set('pos', '0' 'sqrt(3)*pitch');
model.geom('geom1').feature('c3').set('r','radius');
%Track2
model.geom('geom1').feature.create('c4', 'Circle');
model.geom('geom1').feature('c4').set('pos', '0' '-sqrt(3)*pitch');
model.geom('geom1').feature('c4').set('r','radius');
%Track3
model.geom('geom1').feature.create('c5', 'Circle');
model.geom('geom1').feature('c5').set('pos', '-2*pitch' '0');
model.geom('geom1').feature('c5').set('r','radius');
%Track4
model.geom('geom1').feature.create('c6', 'Circle');
model.geom('geom1').feature('c6').set('pos', '2*pitch' '0');
model.geom('geom1').feature('c6').set('r','radius');
%Track5
model.geom('geom1').feature.create('c7', 'Circle');
model.geom('geom1').feature('c7').set('pos', '-3/2*pitch' 'sqrt(3)/2*pitch');
model.geom('geom1').feature('c7').set('r','radius');
%Track6
```

```
model.geom('geom1').feature.create('c8', 'Circle');
model.geom('geom1').feature('c8').set('pos', '3/2*pitch' 'sqrt(3)/2*pitch');
model.geom('geom1').feature('c8').set('r','radius');
%Track7
model.geom('geom1').feature.create('c9', 'Circle');
model.geom('geom1').feature('c9').set('pos', '-3/2*pitch' '-sqrt(3)/2*pitch');
model.geom('geom1').feature('c9').set('r','radius');
%Track8
model.geom('geom1').feature.create('c10', 'Circle');
model.geom('geom1').feature('c10').set('pos', '3/2*pitch' '-sqrt(3)/2*pitch');
model.geom('geom1').feature('c10').set('r','radius');
%Track9
model.geom('geom1').feature.create('c11', 'Circle');
model.geom('geom1').feature('c11').set('pos', '-1*pitch' 'sqrt(3)*pitch');
model.geom('geom1').feature('c11').set('r','radius');
%Track10
model.geom('geom1').feature.create('c12', 'Circle');
model.geom('geom1').feature('c12').set('pos', '1*pitch' 'sqrt(3)*pitch');
model.geom('geom1').feature('c12').set('r','radius');
%Track11
model.geom('geom1').feature.create('c13', 'Circle')
model.geom('geom1').feature('c13').set('pos', '-1*pitch' '-sqrt(3)*pitch');
model.geom('geom1').feature('c13').set('r','radius');
%Track12
model.geom('geom1').feature.create('c14', 'Circle');
model.geom('geom1').feature('c14').set('pos', '1*pitch' '-sqrt(3)*pitch');
model.geom('geom1').feature('c14').set('r','radius');
%Enclosing circle 1
model.geom('geom1').feature.create('c2', 'Circle');
model.geom('geom1').feature('c2').set('pos', '0' '0');
model.geom('geom1').feature('c2').set('r','claddingradius');
```

```
%Enclosing circle 2
model.geom('geom1').feature.create('c1', 'Circle');
model.geom('geom1').feature('c1').set('pos', '0' '0');
model.geom('geom1').feature('c1').set('r','pmlradius');
model.geom('geom1').feature.create('uni1', 'Union');
model.geom('geom1').feature('uni1').set('intbnd', false);
model.geom('geom1').feature('uni1').set('edge', 'all');
model.geom('geom1').feature('uni1').selection('input').set('c1');
model.geom('geom1').run;
%Selection of materials for different domains
model.material.create('mat1');
model.material('mat1').propertyGroup.create('RefractiveIndex', 'Refractive index');
model.material('mat1').selection.set([1 2]);
model.material.create('mat2');
model.material('mat2').propertyGroup.create('RefractiveIndex', 'Refractive index');
model.material('mat2').selection.set([3:14]);
%Selection of study
model.physics.create('emw', 'ElectromagneticWaves', 'geom1');
%Mesh
model.mesh.create('mesh1', 'geom1');
model.mesh('mesh1').feature.create('ftri1', 'FreeTri');
%Selection of PML
model.coordSystem.create('pml1', 'geom1', 'PML');
model.coordSystem('pml1').selection.set([1]);
%Defining material RIs
model.material('mat1').name('unmodified_lithium_niobate');
model.material('mat1').propertyGroup('RefractiveIndex').set('n', '');
model.material('mat1').propertyGroup('RefractiveIndex').set('ki', '');
model.material('mat1').propertyGroup('RefractiveIndex').set('n', 'no' '0' '0' '0' 'ne' '0'
'0' '0' 'no');
model.material('mat1').propertyGroup('RefractiveIndex').set('ki', '0' '0' '0' '0' '0' '0' '0'
```

```
'0' '0');
model.material('mat1').propertyGroup('RefractiveIndex').set('lambda0', 'c_const/freq');
model.material('mat2').name('modified_lithium_niobate');
model.material('mat2').propertyGroup('RefractiveIndex').set('n', '');
model.material('mat2').propertyGroup('RefractiveIndex').set('ki', '');
model.material('mat2').propertyGroup('RefractiveIndex').set('n', 'no-delta_n' '0' '0' '0' 'ne-
delta_n' '0' '0' '0' 'no-delta_n');
model.material('mat2').propertyGroup('RefractiveIndex').set('ki', '0' '0' '0' '0' '0' '0' '0'
'0' '0');
model.material('mat2').propertyGroup('RefractiveIndex').set('lambda0', 'c_const/freq');
%Defining the feature of study
model.physics('emw').feature('wee1').set('DisplacementFieldModel', 'RefractiveIndex');
%Defining the features of mesh. The same type of mesh is applied, here, on all domains.
%User-defined values can also be applied for different domains.
model.mesh('mesh1').feature('size').set('hauto', 3);
model.mesh('mesh1').run;
%Setting the coordinate system for PML. PML settings here are program defined. User
%defined PML settings may also be applied.
model.coordSystem('pml1').set('ScalingType', 'Cylindrical');
%Creating a study mode and defining its properties.
model.study.create('std1');
model.study('std1').feature.create('mode', 'ModeAnalysis');
model.sol.create('sol1');
model.sol('sol1').study('std1');
model.sol('sol1').attach('std1');
model.sol('sol1').feature.create('st1', 'StudyStep');
model.sol('sol1').feature.create('v1', 'Variables');
model.sol('sol1').feature.create('e1', 'Eigenvalue');
model.study('std1').feature('mode').set('neigs', '30');
model.study('std1').feature('mode').set('shift', 'no');
model.study('std1').feature('mode').set('modeFreq', 'c_const/(Lambda[um])');
```

```
model.sol('sol1').attach('std1');
model.sol('sol1').feature('st1').name('Compile Equations: Mode Analysis');
model.sol('sol1').feature('st1').set('studystep', 'mode');
model.sol('sol1').feature('v1').set('control', 'mode');
model.sol('sol1').feature('e1').set('control', 'mode');
model.sol('sol1').feature('e1').set('transform', 'effective_mode_index');
model.sol('sol1').feature('e1').set('shift', 'no');
model.sol('sol1').feature('e1').feature('aDef').set('complexfun', true);
%Defining the plotting properties.
model.result.create('pg1', 'PlotGroup2D');
model.result('pg1').feature.create('surf1', 'Surface');
%The script given above can be run inside a loop to study the change of any of the parameters
defined in the parameter defining section.
track_radius=0.5:0.1:1;
for j=1:1:size(track_radius)
rd=track_radius(j);
model.param.set('radius', rd);
model.sol('sol1').runAll;
RIs_of_eigenmodes(:,j) = mphinterp(model,'emw.neff','coord', [0 0 0;0 0 0], 'complexout','on');
end
%%%%%The script given above is just an introductory example.%%%
```

A.2 A matlab code to construct RI profile from cumulative phase data

```
% A matlab program to construct RI profile from cumulative phase data

lambda=0.480; %filter wavelength
lambda_rad=lambda/2/pi; % filter wavelength (in radians)
ph=load('phaseprofile.txt'); % Read the phase data
vx=ph(:,1)-min(ph(:,1));
```

```
L=max(vx);
ud=abs(ph(2,1)-ph(1,1));
udu=ud/L;
vy=lambda/2/pi.*(ph(:,2)-min(ph(:,2)));
ll=length(vy);
subplot(2,2,1)
plot(vx,vy);
xlabel('Distance ( μm )');
ylabel( 'OPD (radian)');
title('One sided phase profile taken from microscope');
fvy=flipdim(vy,1);
fvy(ll+1:1:2*ll-1,1)=vy(2:1:ll);
fvx=-flipdim(vx,1)/L;
fvx(ll+1:1:2*ll-1,1)=vx(2:1:ll)/L;
c=spline(fvx,fvy);
stp1=udu/40;
fvxx= -1:stp1:1;
fvyint = ppval(c, fvxx);
subplot(2,2,2)
plot(fvxx,fvyint,'o',fvx,fvy,'r')
xlabel('Distance ( Normalized )');
ylabel( 'OPD (radian)');
title('Mirrored Optical Path Difference (OPD) image (Red) & Fitting Function (Blue)');
nf=70; % Number of coefficients in Fourier series expansion.
stp2=abs(fvxx(1)-fvxx(2));
A0=sum(fvyint*stp2)/2; % A0 in Fourier series expansion
fp=A0;
for n=1:1:nf
A(n)=sum(stp2*fvyint.*cos(n*pi*fvxx));% A parameters in Fourier series expansion
B(n)=sum(stp2*fvyint.*sin(n*pi*fvxx));% B parameters in Fourier series expansion
fp=fp+A(n).*cos(n*pi*fvxx)+B(n).*sin(n*pi*fvxx);
```

```
end
subplot(2,2,3)
plot(fvxx,fp,'o',fvx,fvy,'r') % Phase profile
xlabel('Distance ( Normalized )')
ylabel( 'OPD (radian)')
title('Fourier Polynomial fitting (Red) and original phase data (Blue) ')
n_point=91;
for jj=0:1:n_point
ro=jj*L/n_point;
for kk=1:1:nf
zz=ro/L;
fun = @(t)sin(pi*kk*sqrt(t.^2+zz^2))./sqrt(t.^2+zz^2);
q = integral(fun,0,sqrt(1-zz^2));
gg(kk)=2*kk/pi*q;
end
refr_ind(jj+1)=pi/2/L*sum(A.*gg);
end
subplot(2,2,4)
plot(L/n_point*(0:1:n_point),refr_ind) % Refractive Index profile
xlabel('Distance ( μm )')
ylabel( 'Refractive Index ')
title('Reconstructed RI Profile ')
```

Appendix B

Publications

Articles in peer-reviewed journals

1. H. Karakuzu, M. Dubov, and S. Boscolo, Control of the properties of micro-structured waveguides in lithium niobate crystal, *Optics Express*, vol. 21, no. 14, pp. 17122-17130, 2013.

2. S. Boscolo, C. Finot, H. Karakuzu, and P. Petropoulos, Pulse shaping in mode-locked fiber lasers by in-cavity spectral filter, *Optics Letters*, vol. 39, no. 3, pp. 438-441, 2014.

3. H. Karakuzu, M. Dubov, S. Boscolo, L. A. Melnikov, and Y. A. Mazhirina, Optimisation of microstructured waveguides in z-cut $LiNbO_3$ crystals, *Optical Materials Express*, vol. 4, no. 3, pp. 541-552, 2014.

Articles in peer-reviewed conference proceedings

1. H. Karakuzu, M. Dubov, and S. Boscolo, Control of the properties of micro-structured waveguides in $LiNbO_3$ fabricated by direct femtosecond laser inscription, *Conference Digest of the Conference on Lasers and Electro-Optics Europe - International Quantum Electronics Conference 2013 (CLEO/Europe-IQEC 2013)* (IEEE), paper CE-8.3, Munich, Germany, May 2013

2. H. Karakuzu, M. Dubov, and S. Boscolo, Control of the properties of z-cut lithium niobate crystal micro-structured waveguide by its geometry, *Proceedings of the 2nd Summer School and International Workshop: Photonics Meets Biology,* Crete, Greece, September 2013.

3. H. Karakuzu, M. Dubov, S. Boscolo, L. A. Melnikov, and Y. A. Manzhirina, Control of the properties of micro-structured waveguides in lithium niobate crystals, *Technical Digest of the OSA topical meeting on Advanced Solid-State Lasers and Mid-Infrared Coherent Sources (MICS 2013)*, paper JTh2A.22, Paris, France, October 2013.

4. M. Dubov, H. Karakuzu, and S. Boscolo, Optimization of micro-structured waveguides in lithium niobate, *Proceedings of the XXII International Workshop on Waveguide Theory and Numerical Modelling (OWTNM 2014)*, paper P-30, p. 73, Nice, France, June 2014.

5. H. Karakuzu, M. Dubov, and S. Boscolo, Optimisation of micro-structured waveguides in lithium niobate (z-cut), *Proceedings of the Comsol Conference*, paper 199881, Cambridge, United Kingdom, September 2014.

6. H. Karakuzu, M. Dubov, S. Boscolo, Y. O. Azabi, and A. Agrawal, Equiangular spiral

micro-structured waveguides in lithium niobate, *Proceedings of the XXIII International Workshop on Optical Wave & waveguide Theory and Numerical Modelling (OWTNM 2015)*, P-98, London, United Kingdom, April 2015.